Applications of the density-matrix renormalization group to mesoscopic phenomena

Dominique Gobert

RHEINISCH-WESTFÄLISCHE TECHNISCHE HOCHSCHULE AACHEN

Aachen 2004

Applications of the density-matrix renormalization group to mesoscopic phenomena

Dominique Gobert

Von der Fakultät für
Mathematik, Informatik und Naturwissenschaften
der Rheinisch-Westfälischen Technischen Hochschule Aachen
zur Erlangung des akademischen Grades
eines Doktors der Naturwissenschaften
genehmigte Dissertation

vorgelegt von

Dipl.-Phys. Dominique Gobert
aus München

Berichter:
Universitätsprofessor Prof. Dr. Ulrich Schollwöck
Universitätsprofessor Prof. Dr. Herbert Schoeller

Tag der mündlichen Prüfung: 13. Dezember 2004

Diese Dissertation ist auf den Internetseiten der
Hochschulbibliothek online verfügbar.

Contents

Deutsche Zusammenfassung **ix**

1 Introduction **1**

2 DMRG method **5**
2.1 Overview 5
2.2 The algorithm 6
2.3 Error analysis 10
2.4 Technical issues 11

3 Josephson effect between superconducting nanograins with discrete energy levels **13**
3.1 Introduction 13
3.2 Josephson effect for weakly coupled superconductors: Theory . 16
3.2.1 Josephson effect as a phase dependent delocalization energy 16
3.2.2 Pair tunneling Hamiltonian 18
3.2.3 Tight-binding model 20
3.2.4 Discussion of the tight-binding model 21
3.2.5 The effect of charging energy 22
3.2.6 Generalization to strong coupling 24
3.3 DMRG approach 25
3.3.1 The DMRG method in energy space 26
3.3.2 One-grain DMRG for tight-binding model 29
3.3.3 Two-grain DMRG 29
3.4 Results 30
3.4.1 From small to large grains: The effect of discrete energy levels within the tight-binding model 30
3.4.2 Limitations of the tight-binding approach 35

4 Well-defined quasiparticles in interacting metallic grains 43
4.1 Introduction . . . 43
4.2 Excitation spectrum, No-Gaudino states . . . 45
4.3 DMRG implementation of the No-Gaudino Approximation . . 49
4.4 Dominance of a single No-Gaudino state . . . 50
4.5 Applications . . . 53
4.5.1 Tunneling density of states . . . 53
4.5.2 Magnetic response of rings . . . 53

5 Real-time dynamics in spin-1/2 chains with adaptive time-dependent DMRG 59
5.1 Introduction . . . 59
5.2 Model and initial state . . . 61
5.3 Outline of the adaptive t-DMRG . . . 63
5.4 Accuracy of the adaptive time-dependent DMRG . . . 66
5.4.1 Possible errors . . . 66
5.4.2 Error analysis for the XX-model . . . 67
5.4.3 Optimal choice of DMRG parameters . . . 75
5.5 Long-time properties of the time-evolution . . . 76
5.6 Conclusions . . . 89

6 Many-body scattering states via DMRG 91
6.1 Introduction . . . 91
6.2 Scattering states and the Lippmann-Schwinger equation . . . 92
6.3 Scattering "theory" in a finite system . . . 95
6.3.1 General considerations . . . 95
6.3.2 Example: Single particle with a δ potential . . . 98
6.4 Generalization to many-body states and DMRG solution . . . 102
6.5 Applications . . . 103
6.5.1 Real-space representation . . . 103
6.5.2 Momentum representation . . . 107

7 Conclusions 109

A DMRG algorithm in energy space 113

B Exact solution for noninteracting chain in real space 117
B.1 Single particle scattering state . . . 117
B.2 Many-body scattering state . . . 118

Bibliography 121

List of publications **126**

Acknowledgments **128**

List of Figures

2.1 Infinite-system DMRG algorithm 8
2.2 Finite-system DMRG algorithm 9

3.1 Error between Richardson's solution and two-grain DMRG . . 28
3.2 Josephson energy E_J in the tight-binding approximation . . . 31
3.3 Various approximations for the matrix element $\langle N|b_i|N+1\rangle$. 33
3.4 E_J^0 from the BCS, the finite-d BCS and the DMRG method . 34
3.5 Regimes of validity for the DMRG and the tight-binding approach 36
3.6 Josephson energy in the tight-binding and in the DMRG approach at small inter-grain coupling 38
3.7 Josephson energy in the tight-binding and in the DMRG approach at large inter-grain coupling 39
3.8 Josephson energy as a function of the inter-grain coupling . . . 41

4.1 Illustration of the Hilbert space structure for the pairing Hamiltonian 47
4.2 Comparison of full result and No-Gaudino approximation for the sum rule of a spectral function 51
4.3 Position of the maximum of the lost weight in the No-Gaudino approximation in the λ-γ-plane 52
4.4 The tunneling density of states in the No-Gaudino approximation 54
4.5 The magnetic response of rings in the No-Gaudino approximation 55

5.1 Quantum phase diagram of the Heisenberg model. 61
5.2 Magnetization deviation as a function of time for different Trotter time steps dt. 69
5.3 Magnetization deviation as a function of Trotter time step dt at times $t = 5$ and $t = 30$. 70

5.4 Forth-back error $FB(t)$ for $t = 30$ and $t = 50$ as function of dt. 71
5.5 Magnetization deviation $\Delta M(t)$ as a function of time for different numbers m of DMRG states. 72
5.6 The forth-back error as function of t. 73
5.7 The forth-back error as function of m. 74
5.8 Entanglement entropy between the left and the right half of the chain as function of time. 75
5.9 Lost weight in the density matrix truncation, summed over time intervals $\Delta t = 0.1$. 77
5.10 Time evolution of the absolute value of the local magnetization $|\langle S_n^z(t)\rangle|$ for the XX model as a density plot. 79
5.11 Density plots of the magnetization $|\langle S_n^z(t)\rangle|$ for $J_z = 0$, 0.3, 0.6, 0.9, 1.0, 1.1, and $\delta = 0$. 80
5.12 The change in the magnetization $\Delta M(t)$ for J_z =0; 0.3; 0.6; 0.9; 1.0; 1.1; 1.5 81
5.13 Best fit for the exponent a in $\Delta M(t) \propto t^a$. 82
5.14 $J_z = 1$: The change of the magnetization in a double logarithmic plot with an algebraic fit. 83
5.15 $J_z = 1$: Collapse of magnetization for a superdiffusive scaling form $(n/t^{0.6})$. 84
5.16 Current, averaged over the 5 middle sites, for various values of J_z between 0 and 1.1. 85
5.17 Density plots of the magnetization $\langle S_n^z(t)\rangle$ for dimerization δ =0; 0.2; 0.4; 0.6; 0.8; 1.0, and $J_z = 0$. 86
5.18 Change in magnetization $\Delta M(t)$ for dimerization $\delta = 0$, 0.2, 0.4, 0.6, 0.8, 1.0. 87
5.19 Best fit for the exponent a in $\Delta M(t) \propto t^a$. 88

6.1 Scattering of a single particle in two dimensions 93
6.2 Scattering of a single particle in one dimension 99
6.3 Current from the scattering state for nonzero η 100
6.4 Illustration of the nonequilibrium situation considered in section 6.5 103
6.5 Illustration of the real-space scattering formalism 104
6.6 Comparison of DMRG and exact solution for the scattering current 106

A.1 Sketch of the two-grain DMRG projection 114

Deutsche Zusammenfassung

In der vorliegenden Doktorarbeit untersuche ich Eigenschaften von mesoskopischen Systemen, in denen starke Quantenkorrelationen auftreten. Zu diesem Zweck benutze ich die Dichtematrix-Renormierungsgruppe (DMRG), eine numerische Methode, die speziell für die theoretische Untersuchung starkkorellierter Quantensysteme entwickelt wurde. Gleichzeitig führen die in der vorliegenden Arbeit untersuchten Fragestellungen zu einigen methodischen Weiterentwicklungen der DMRG, die ich ebenfalls detailliert beschreibe. Im folgenden gebe ich eine Übersicht über die einzelnen in dieser Arbeit untersuchten physikalischen Fragestellungen:

Josephson-Effekt zwischen supraleitenden Nanokörnern

Vor einigen Jahren ist es der Gruppe von Dan Ralph gelungen, tunnelspektroskopische Experimente an supraleitenden Körnern mit einem Durchmesser von nur wenigen Nanometern durchzuführen, in denen der Abstand der Energieniveaus d von der gleichen Größenordnung wie die supraleitende Bandlücke Δ_{BCS} ist [vDR01]. In diesem Regime verliert die BCS-Theorie der Supraleitung ihre Gültigkeit. Dennoch konnten supraleitende Paarkorrelationen indirekt über einen "Even-Odd-Effekt" nachgewiesen werden.

In der vorliegenden Arbeit untersuche ich den Josephson-Effekt – die Abhängigkeit der Energie zweier gekoppelter Supraleiter von der Differenz ihrer supraleitenden Phasenvariablen – als weitere Manifestation supraleitender Eigenschaften im Regime $d \sim \Delta_{\mathrm{BCS}}$. Zu diesem Zweck berechne ich den Grundzustand zweier gekoppelter supraleitender Körner und bestimme daraus die Josephson-Energie, welche die Stärke des Josephson-Effekts charakterisiert.

Im Limes großer Körner ($d \to 0$) reproduziert die Rechnung das Ergebnis der BCS-Theorie, für wachsendes d stelle ich sodann einen nichtmonotonen Verlauf der Josephson-Energie fest. Mit Hilfe eines tight-binding-Modells läßt sich dieser Verlauf qualitativ erklären.

Wohldefinierte Quasiteilchen in metallischen Körnern

Im zweiten Teil der Arbeit analysiere ich elektronische Spektralfunktionen metallischer Körner, in denen die Elektron-Elektron-Wechselwirkungen durch einen dem BCS-Modell ähnlichen "universellen Hamiltonoperator" beschrieben werden. Spektralfunktionen erlauben die Berechnung vieler physikalisch relevanter dynamischer Messgrößen.

Ich zeige, daß eine wichtige Klasse dieser Funktionen von einem einzigen angeregten Zustand dominiert wird. Eine unmittelbare Schlussfolgerung aus dieser Erkenntnis ist, daß die in den untersuchten Spektralfunktionen auf-

tretenden Quasiteilchen (unendlich) langlebig sind. Zudem zeige ich, daß der die Spektralfunktionen dominierende Zustand nur einen bestimmten Typ von Anregungen, die ich als "No-Gaudino"-Anregungen charakterisiere, enthält: Nur diese sind demzufolge für viele Eigenschaften der betrachteten Systeme relevant.

Die Dominanz der "No-Gaudino"-Zustände hat darüberhinaus auch einen hohen praktischen Wert: Denn sie ermöglicht es, Spektralfunktionen mit Hilfe der DMRG mit hoher Genauigkeit zu berechnen. Als Anwendungsbeispiel dieser Methode berechne ich die Tunnelzustandsdichte metallischer Körner und den Kreisstrom in von Magnetfeldern durchdrungenen mesoskopischen Ringen.

Realzeit-Dynamik von Spinketten

Ein weiteres Thema meiner Arbeit ist das Verhalten von Spinketten fern des Gleichgewichts. Ich untersuche den Einfluß verschiedener Wechselwirkungen und Dimerisierungen auf den Magnetisierungstransport in Spin-1/2-Ketten mit Nächster-Nachbar-Wechselwirkung, indem ich die Zeitentwicklung eines nichtstationären Anfangszustands $|\uparrow \ldots \uparrow\downarrow \ldots \downarrow\rangle$ betrachte. Zu diesem Zweck benutze ich die "adaptive time-DMRG", eine kürzlich entwickelte DMRG-Variante, die das Lösen der Vielteilchen-Schrödingergleichung mit hoher Genauigkeit erlaubt.

Hierbei stelle ich fest, daß die Magnetisierung einen wohldefinierten Limes für lange Zeiten besitzt, dessen qualitatives Verhalten nicht von der Dimerisierung, sondern allein von der Stärke J_z der S^zS^z-Wechselwirkung abhängt: Für $|J_z| < 1$ findet ballistischer Magnetisierungstransport statt, für $|J_z| > 1$ dagegen bleibt die Magnetisierung nahezu konstant, mit einem scharfen Übergang zwischen beiden Regimes bei $|J_z| = 1$. Ich erkläre dieses Verhalten als Konsequenz eines Quantenphasenübergangs bei $|J_z| = 1$.

Vielteilchen-Streuzustände

Im letzten Teil meiner Arbeit führe ich eine allgemeine Methode ein, die die Berechnung von Transporteigenschaften stark wechselwirkender Vielteilchensysteme fern des Gleichgewichts zum Ziel hat. Ich beschränke mich auf die Beschreibung des Verfahrens selbst, und präsentiere nur wenige einfache Berechnungen illustrierenden Charakters.

Die Methode basiert auf der Streutheorie: Es wird der Vielteilchen-Streuzustand $|\psi_V\rangle$ berechnet, der sich ergibt, wenn zwei Zuleitungen mit einer Spannungsdifferenz V über einen Streuer (z.B. einen Quantenpunkt) miteinander verbunden werden. $|\psi_V\rangle$ wird hierbei mit Hilfe der DMRG als Lösung der Lippmann-Schwinger-Gleichung gewonnen. Die Kenntnis von $|\psi_V\rangle$ für verschiedene angelegte Spannungen V erlaubt es wiederum, die Strom-Spannungs-Charakteristik $I(V) = \langle\psi_V|\hat{I}|\psi_V\rangle$ des Streuers zu bestimmen.

Chapter 1

Introduction

Strongly correlated quantum systems are of considerable interest both in experimental and theoretical physics due to their high degree of entanglement: The quantum states of their constituents cannot be considered separately, but must instead be described with reference to each other using a full many-body wave function. Such systems are of particular relevance in mesoscopic physics, because the quantum correlations are enhanced at low temperatures and in small samples, where the interactions between electrons increase due to their spatial confinement.

Owing to recent advances in microfabrication techniques, it has become possible to fabricate samples, e.g. quantum point contacts, quantum dots, metallic grains and even individual molecules, in which quantum correlations have a measurable influence on the electronic transport properties. Prominent examples include remnants of superconducting correlations in small grains [vDR01] and resonant scattering on magnetic impurities or otherwise degenerate degrees of freedom (see among others [PG04; COK98; GGSM$^+$98]), where quantum correlations were found to influence the transport characteristics drastically. In this thesis, I study these and other phenomena in detail; a comprehensive overview of the precise topics is given below.

Strongly correlated systems are difficult to describe theoretically: In general, Their ground state cannot be obtained by adding small corrections to a simple "free" state, therefore perturbation theory is not applicable. In this thesis, I use the density-matrix renormalization group (DMRG), a numerical method that has been developed specifically for analyzing such systems. Like in other renormalization group techniques, the main idea behind the DMRG algorithm is to find a description in terms of an effective model, in which the degrees of freedom of the original model have been greatly reduced. This effective model is then numerically manageable, but nevertheless captures

the essential physics of the original model.

The DMRG method in its original form is limited to the calculation of static ground-state properties, i.e. equilibrium properties at zero temperature, of one-dimensional systems. Within these limitations, the DMRG turned out to be an extremely successful and versatile method that produces results with unprecedented accuracy. However, many physically relevant properties do not fall into the above class of problems: Firstly, most interesting mesoscopic devices are not one-dimensional. Secondly, often properties far from equilibrium are important, in particular in transport measurements, where typically a fairly large bias voltage is applied. A number of adaptations of the DMRG have therefore been proposed that overcome some of its original limitations (see [Sch04] and references therein). I present several such extensions in this thesis. Some of them are newly invented, some others are adaptations of ideas that had been previously developed by other authors.

Although the unifying theme of this work is the DMRG method and its variants, their use is motivated by a number of open questions in mesoscopic physics. In the following, I present a summary of the physical problems addressed in this thesis.

Josephson effect between superconducting nanograins

It has recently become possible to perform tunneling spectroscopy experiments on small superconducting aluminium grains with a diameter of only a few nanometers [vDR01]. These grains are so small that the energy level spacing d is comparable to the bulk superconducting gap Δ_{BCS}. Hence, standard BCS theory of superconductivity is not applicable: In the BCS wave function, the dominant contribution to pairing correlations stems from levels within a range of the order Δ_{BCS} around the Fermi surface, but there are no such levels left when $d \geq \Delta_{\mathrm{BCS}}$.

Nevertheless, the experiments revealed an even-odd effect, i.e. an energy penalty for states containing an odd numbers of electrons, as a clear indication of remaining superconducting correlations even for level spacings as large as $d \sim \Delta_{\mathrm{BCS}}$. This leads naturally to the question how these correlations can be described without reference to the BCS solution, and whether there remain other, more direct signatures of superconductivity in that regime, in particular the Josephson effect.

Motivated by this question, I investigate in chapter 3 the Josephson effect, i.e. the dependence of the energy of two weakly coupled superconductors on the difference between their superconducting phase, in the regime $d \sim \Delta_{\mathrm{BCS}}$. Because the BCS solution is inapplicable, I use the DMRG to calculate the ground state of the two coupled superconductors and extract the characteristic energy scale, the Josephson energy E_J.

From the point of view of this method, the challenge consists in applying

the DMRG to systems in more than one dimension. The "trick", introduced in this context by Sierra et al. [DS99], is to organize the degrees of freedom (the one-particle eigenstates of the free Hamiltonian) along an energy axis, which is always one-dimensional. In energy space, the system can then be treated just like a one-dimensional chain. The price to pay, however, is that the interactions are highly nonlocal in this setting: Because all energy levels tend to interact with each other, the number of interaction terms is expected to scale quadratically with the number of energy levels N. Such interactions are highly inefficient to implement in the DMRG. Luckily, it is possible to deal with these complications in the reduced BCS model, because there, the $O(N^2)$ interaction terms can be grouped efficiently into only a few ($O(1)$) terms.

Well-defined quasiparticles in small metallic grains

In chapter 4, I analyze zero-temperature spectral functions of mesoscopic systems such as quantum dots and metallic grains, in the limit of large conductance. As shown in [ABG02], these systems can be described by a "universal Hamiltonian". Spectral functions, in turn, reveal many measurable and physically interesting dynamical properties of these systems.

I show that within the universal Hamiltonian model, an important class of spectral functions is dominated by one single energy eigenstate only. For an interacting system this is a very peculiar property, since the interactions usually shift a significant portion of the spectral weight to a background of excitations, responsible for the finite life-time of the quasiparticles.

Besides its own physical significance, this property has also high practical value, because it permits the calculation of zero-temperature spectral functions with high accuracy using the DMRG. I illustrate the use of this method by calculating the tunneling density of states of metallic grains and the magnetic response of mesoscopic rings.

Real-time dynamics in spin-1/2 chains

Transport through mesoscopic systems is often far from equilibrium. This regime is, however, difficult to describe theoretically. In the absence of a unified theory of nonequilibrium phenomena, it seems promising to have a particular model at hand that allows a direct study. Spin chain models are very instructive in this respect because they provide a comparatively simple framework that nevertheless exhibits rich behaviour, such as a nontrivial phase diagram with strongly correlated ground states in some of the phases.

In chapter 5, I study nonequilibrium properties of spin-1/2 chains by calculating the time evolution of a non-stationary initial state $|\uparrow \ldots \uparrow\downarrow \ldots \downarrow\rangle$. This system can also be interpreted as an oversimplified picture for spin transport between two coupled reservoirs of completely polarized spins of opposite direction. I investigate the influence of different interaction strength

and dimerization on the magnetization transport and in particular address the following questions: Does the state evolve into a simple long-time limit? If so, how is this limit reached? On what model parameters and properties does the long-time behaviour depend?

Directly calculating the time evolution, i.e. solving the full many-body Schrödinger equation of an interacting system is highly nontrivial. A recently developed DMRG variant, the adaptive time-dependent DMRG [Vid04; DKSV04; WF04], however, allows to perform this task with high accuracy. This method is able to adapt dynamically the projected DMRG state space to the time evolution of the state, such that the latter is in principle well-represented at all times.

As until now no detailed error analysis of this new method has been performed, it is also important to address the questions what kinds of errors can occur in principle, which ones of these dominate in practice, and how they can be minimized. Spin-1/2 chains provide an excellent benchmark for the adaptive time-dependent DMRG because of the existence of a nontrivial exact solution for a particular point in parameter space known as the XX model [ARRS99], against which the DMRG results can be compared.

Many-body scattering states

Chapter 6 is of rather general nature. Here, I present a newly developed method that, if implemented, should be able to describe the transport properties of strongly interacting many-body systems far from equilibrium, i.e. without the use of perturbation or linear response theory.

The approach presented here is based on scattering theory: The goal is to calculate the scattering state $|\psi_V\rangle$ that emerges when two leads with a chemical potential difference $\Delta\mu = eV$ are coupled via a scatterer (e.g. a quantum dot or a quantum point contact). The strategy for obtaining $|\psi_V\rangle$ is to solve the many-body Lippmann-Schwinger equation using the DMRG. Knowledge of $|\psi_V\rangle$ for arbitrary voltage V then allows one to obtain the I-V-characteristic $I(V) = \langle\psi_V|\hat{I}|\psi_V\rangle$ of the scatterer. In contrast to the well-known approach of Landauer and Büttiker [BILP85; Dat95], which is also based on scattering theory, the present approach uses a full many-body formalism in order to describe the strongly correlated regime.

Chapter 2

DMRG method

2.1 Overview

This chapter provides an overview of the standard density-matrix renormalization group (DMRG) algorithm. The subsequent chapters build on this description as a background; there, the DMRG is adapted and developed further in order to solve specific problems in mesoscopic physics. There exist a number of pedagogical introductions and reviews of the DMRG method [WN99; Sch04]. Therefore I limit myself to a rather brief description here, putting the emphasis on the basic algorithmic concepts and on the limitations of the method.

The DMRG was originally developed as a numerical method for calculating the low-energy properties of strongly correlated quantum systems, such as the Hubbard and the Heisenberg model (see [WN99] and references therein). The ground state of these models cannot be obtained by adding some small correction to an exactly solvable model, therefore perturbation theory is not applicable. Besides approaches based on the Bethe ansatz technique, it can be said that the only generally available and reliable solutions for these models are numerical ones, such as exact diagonalization, Monte Carlo, and DMRG calculations.

Like in other renormalization group techniques, [1] the main idea of the DMRG algorithm is to eliminate microscopic degrees of freedom successively. This leads to a description in terms of an effective model that is numerically manageable, but nevertheless captures the essential physics of the original model.

[1] Actually, it is a matter of debate whether the DMRG is a "true" RG approach, as it lacks some distinguishing features of other RG methods. See [Sch04] and references therein.

The standard DMRG method is limited in its range of applicability. In its original formulation, it was restricted to one-dimensional systems with local interactions. Moreover, only ground state properties were available, i.e. only static phenomena at zero temperature could be analysed.

In its domain, the DMRG was extremely successful, capable of producing results of unprecedented accuracy, in some cases almost as high as machine precision. Therefore, and due to the conceptual versatility of the DMRG, a number of extensions have been proposed that overcome the original limitations. The subsequent chapters of this thesis follow that path: There, I introduce and apply several such extensions that are particularly useful in mesoscopic physics.

2.2 The algorithm

I describe here the DMRG algorithm applied to a one-dimensional chain, e.g. a spin chain. The basic idea is to eliminate successively those microscopic degrees of freedom that are not relevant for representing the states of interest (in most cases the ground state of the system), called "target states".

Although the DMRG algorithm differs substantially from other numerical renormalization-group schemes such as Wilson's NRG [Wil75], the basic underlying idea can be described in similar terms: One initially considers a small system containing only a few lattice sites that can be diagonalized exactly. In this system the target state is calculated (which typically is the ground state). Then, the Hilbert space is truncated, i.e. only a limited part of the Hilbert space (of dimension m, typically $m \sim$ 50-500) is kept, namely the most relevant one for representing the target state (in terms of a criterion to be specified below). Then, the chain size is increased by adding new sites. This algorithm is repeated until the desired system size is reached. This is called the infinite-system DMRG. Because the Hilbert space is truncated in each step, the size of the reduced Hilbert space remains constant as new sites are added, whereas the full Hilbert space grows exponentially with system size.

Two kinds of errors are dominant within this algorithm: Firstly, in each DMRG step some information is inevitably lost even upon an optimal truncation of the Hilbert space. This error is called the truncation error. Secondly, a finite-size error is introduced: While optimizing the basis for the small initial systems, the algorithm "does not know" about the sites that are to be added at a later time. Thus, the target state at early DMRG steps is not identical to the target state of the system one is finally interested in. Because open boundary conditions are imposed at the outmost sites of the

chain, which obviously do not represent these "missing sites", the finite-size error can also be seen as a consequence of inappropriate boundary conditions while building up the chain. Despite their conceptual similarities, the DMRG and other real-space RG approaches differ fundamentally in the precise way they address these two errors.

I begin by discussing the finite-size error. Because this error is linked to inappropriate boundary conditions while new sites are added to the system, it makes a difference at which position these sites are added. For example, in Wilson's real-space NRG [Wil75], a new site is added to the *end* of the chain at each RG step; therefore the position of each site with respect to the chain boundaries changes at each step. This procedure works very well in Wilson's original application of the NRG to the Kondo problem, where due to the logarithmic discretization the hopping matrix elements fall off exponentially. Therefore, the additional sites to be added later can indeed be seen as small corrections. In most other models, however, this method is unreliable because boundary errors are more important [WN99].

In the DMRG, the finite-size error is reduced in two ways. Firstly, the new sites are added in the *middle* of the chain as shown in Fig. 2.1. This part of the DMRG algorithm is called the "infinite-system DMRG". Compared to the NRG algorithm, it has the advantage that the position of each site remains fixed at least with respect to its nearest boundary. To this end, the chain must be organized into two blocks (called L and R), so that the new sites can be added between them as shown in Fig. 2.1. The L and R block (consisting of sites $1..n-1$ and $n+2..l$, where $l=2n$ is the chain length) are each represented by m reduced basis states $|\alpha\rangle_{1..n-1}$, $|\beta\rangle_{n+2..l}$. (In the left-right symmetric example shown in Fig. 2.1, the basis vectors $|\alpha\rangle$, $|\beta\rangle$ can be taken to be identical). Within the DMRG, a state in the representation sketched in the upper part of Fig. 2.1 is then written as

$$|\psi\rangle = \sum_{\alpha\sigma\tau\beta} \psi_{\alpha\sigma\tau\beta} |\alpha\rangle_{1..n-1} |\sigma\rangle_n |\tau\rangle_{n+1} |\beta\rangle_{n+2..l}. \tag{2.1}$$

In each DMRG step, two new sites (say, n and $n+1$) are included into blocks L and R, respectively, as shown in the middle part of Fig. 2.1: A new m-dimensional reduced basis $|\alpha'\rangle_{1..n}$, $\alpha'=1..m$ for the Hilbert space of block L is formed. Its members are linear combinations of the old basis vectors $|\alpha\rangle_{1..n-1}|\sigma\rangle_n$. Likewise, a new R block is formed with a new truncated basis $|\beta'\rangle_{n+1..l}$. As explained below, these states are optimally chosen in order to represent the target states. In this new basis, a state is represented as

$$|\tilde{\psi}\rangle = \sum_{\alpha'\beta'} \psi_{\alpha'\beta'} |\alpha'\rangle_{1..n} |\beta'\rangle_{n+1..l}. \tag{2.2}$$

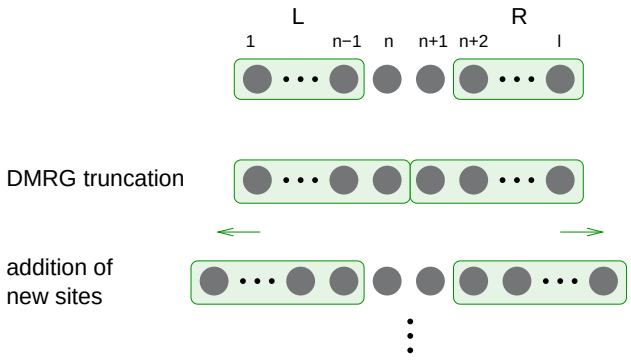

Figure 2.1: Infinite-system DMRG algorithm: A spin chain of length $l = 2n$ is constructed from two blocks L and R, each representing $(n-1)$ sites in a truncated basis, plus two additional sites in the middle (upper figure). A state is expressed in this basis as in Eq. (2.1). In every step of the infinite-system DMRG, one additional site is added to each of the two blocks, and a new truncated basis is formed (middle figure and Eq. (2.2)). In the next step of the infinite-system DMRG, two sites are added to the chain, and the algorithm is repeated.

Then, again two new sites are added to the middle of the chain as shown in the lower part of Fig. 2.1, thus creating a chain of length $l + 2$. This procedure is repeated until the final chain length l_f is reached.

Although this arrangement greatly reduces the errors due to the boundary conditions, nevertheless a finite-size error occurs, in particular during the very first DMRG steps, when the chain length l is likely to be smaller than the correlation length of the system: Then, each site also "sees" the boundary far from it. Hence, the optimal basis states for the small system (which are kept) and the ones for the larger final system (which are needed) may not be identical.

This finite-size error can be corrected in a second part of the DMRG, called the "finite-system algorithm" and illustrated in Fig. 2.2. Here, I only discuss the basic idea of this algorithm, and refer to [WN99; Sch04] for more details. When the final system size l_f has been reached, the, say, left block size is increased further by one site per iteration as in the infinite algorithm. The right block size, however, is *decreased* by the same amount, such that the total chain length l_f is kept constant. Hereby, the reduced basis vectors for the growing (left) block are newly constructed as in the infinite-system algorithm, whereas the basis for the shrinking (right) block is taken from a previous iteration. In this way, the "free sites" n and $n+1$ of Fig. 2.2 sweep

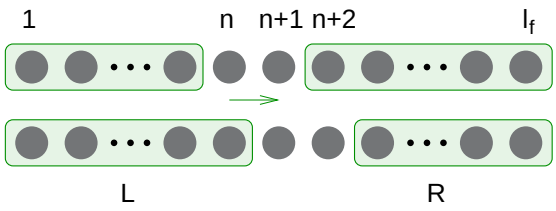

Figure 2.2: Finite-system DMRG algorithm (sweep to the right): As in the infinite-system algorithm, but here only the left block is growing, while the right block is shrinking. This way, the total block length is held fixed.

from left to right across the chain; therefore this procedure is also called a "sweep to the right". For a likewise "sweep to the left" the roles of block L and R are interchanged.

Now the finite-system DMRG algorithm consists of several such sweeps to the left and the right, whereby the sweep direction changes whenever the free sites hit one of the ends of the chain.[2] Because at each sweep, the basis of the growing block is optimized with the full knowledge of the proper boundary conditions, the initial finite-size errors can be corrected. Typically, the target states have converged after 3-10 sweeps. This finite-system part of the DMRG improves the accuracy and reliability of the method greatly.

I now describe the DMRG truncation prescription. For definiteness, I discuss a step of the infinite-system algorithm; the finite-system truncation differs only in minor details. The purpose of the DMRG truncation is to chose m basis vectors $|\alpha'\rangle_{1..n}$ and $|\beta'\rangle_{n+1..l}$ in each new block L and R as shown in the middle part of Fig. 2.1, that are optimally suited for representing a target state $|\psi_{\text{target}}\rangle$. This state is given in terms of the old basis as in Eq. (2.1), and will be given in the new basis as in Eq. (2.2) with suitable coefficients $\psi_{\alpha\sigma\tau\beta}$ and $\tilde{\psi}_{\alpha'\beta'}$, respectively. – The precise optimum condition is that the new basis of Eq. (2.2) must allow the construction of a truncated state $|\tilde{\psi}_{\text{target}}\rangle$ that minimizes the L_2 norm $||\tilde{\psi}_{\text{target}}\rangle - |\psi_{\text{target}}\rangle|$. Here, the minimum is defined with respect to varying both the new basis states and the wave function $\tilde{\psi}_{\alpha'\beta'}$ in Eq. (2.2), while the number of new basis states $|\alpha'\rangle$ and $|\beta'\rangle$ in each block is held fixed at the value m.

This optimum condition is very intuitive, but difficult to implement numerically. However, it can be shown [WN99] that it is equivalent to choosing the truncated basis vectors, say, of the left block $|\alpha'\rangle_{1..n}$, $\alpha' = 1..m$, to be the

[2] More precisely, when they hit almost the end of the chain – see section 2.4.

eigenstates corresponding to the m largest eigenvalues of the reduced density matrix. $\tilde{\rho}_L = \mathrm{Tr}_R |\psi_{\mathrm{target}}\rangle\langle\psi_{\mathrm{target}}|$ A likewise condition exists for $|\beta'\rangle_{n+1..l}$, with the role of L and R interchanged. – This is the truncation prescription that is actually implemented in the DMRG; hence the name. This prescription can be generalized to targeting several states at once: Then, a density matrix is used that represents a mixed state from the various target states with equal weights. (The result turns out to be fairly independent of their relative weights.)

I finally note that a different perspective on the DMRG algorithm was recently provided from quantum information theory. It has been known for some time that the truncated DMRG states always belong to a particular subset of all possible states, namely the so-called matrix product states [OR95; NO95; DMDNS98]. In fact, the DMRG can be recast as a variational method that uses matrix product states as ansatz wave functions, and finds the optimal state among them. This alternative formulation recently opened up a new perspective on extensions of the DMRG that overcome many of its original limitations: For example, the original DMRG was improved drastically with respect to the description of time-dependent systems [Vid04; DKSV04; WF04] and of periodic boundary conditions [VGRC04]; and efficient algorithms for two-dimensional models and finite temperature seem to be within reach [VC04; VGRC04]. Indeed, the adaptive time-DMRG presented in chapter 5 was originally developed in the context of matrix product states [Vid04].

2.3 Error analysis

The errors from the DMRG can be estimated in several ways. Roughly speaking, the eigenvalues of the reduced density matrix $\tilde{\rho}_L$ measure the importance of the corresponding eigenstates for representing the target state. Therefore, the "lost weight" w_L, defined as the sum of all the eigenvalues of the states not kept as basis states, is a good measure for the DMRG truncation error and in fact is often proportional to the errors of physical quantities calculated within the DMRG. However, w_L only measures the truncation error, whereas other sources of error such as the finite-size error are not captured. An example where the lost weight is not a useful measure can be found in section 5.4.

A careful convergence analysis in the number of kept states m usually provides a more reliable estimation of the full error. The DMRG is exact when $m \to \infty$. However, convergence up to tiny errors of, say, 10^{-7} is usually achieved even for moderate values of $m \sim 50 - 300$, at least for

ground state properties of one-dimensional systems with local interactions. [3] Although it cannot be ruled out that an ill-behaved system may be trapped in a metastable state for intermediate values of m, this phenomenon seems to be exceedingly rare in practice.

2.4 Technical issues

I discuss briefly some important, but rather technical issues. More details on them are given in [Sch04] and references therein.

Code performance is increased by orders of magnitude if good quantum numbers such as particle number, total spin etc. are exploited. To this purpose, the quantum numbers associated with each reduced basis state $|\alpha\rangle$ are explicitly kept track of. Most operators have block diagonal or block off-diagonal form in these quantum numbers, or can at least be decomposed into a sum of only a few such operators. The memory for storing these operators and the number of floating-point operations needed for calculating e.g. matrix-vector and matrix-matrix multiplications can be greatly reduced by explicitly storing and evaluating only the non-zero blocks. It is of particular importance that the reduced density matrix $\tilde{\rho}$ is block-diagonal. In order to diagonalize it – which is one of the most time-consuming steps in DMRG –, it is thus sufficient to diagonalize the smaller submatrices within each block, which is much faster than diagonalizing one large matrix.

I mention briefly how the target state(s) are constructed. The details depend on the precise nature of the target state. I restrict myself here to the most common case, namely the target state being the ground state of some Hamiltonian H. The ground state is calculated using the Lanczos algorithm described in [Saa03]. This algorithm reproduces the lowest (and highest) eigenvalue and the corresponding eigenvector of a matrix with high accuracy, but is much more efficient than a full diagonalization of H. It has the further significant advantage that the full Hamiltonian needs not to be stored in matrix form; instead, it is sufficient to know its action $H|\phi\rangle$ on a state $|\phi\rangle$. The latter can usually be computed by applying a few operators living on the L or R block to $|\phi\rangle$, i.e. operators only of dimension $m \times m$, instead of the dimension $m^2 \times m^2$ of the full Hamiltonian H.

A further technical detail is that the rank of $\tilde{\rho}$ cannot exceed the dimension of the block that is being traced over. For that reason, a sweep must end

[3] This is related to the fact that for these states, the reduced density matrices can be shown to have an eigenvalue spectrum that is exponentially decaying, see [Sch04] and references therein. Therefore, w_L is exponentially suppressed as the number of kept states m is increased.

when one of the blocks becomes so small that the dimension of its full associated Hilbert space is smaller than m: Otherwise, information about the state is lost upon performing the trace of $\tilde{\rho}$, because the number of meaningfully kept states m is effectively reduced to the dimension of the small block. For more details see e.g. [Sch04].

I implemented the DMRG algorithm in C++. This has the advantage that most routines can be hidden in an object-oriented class hierarchy. Once the algorithm was implemented, this allowed me to reuse most of the existing code across all problems discussed in the subsequent chapters. Furthermore, there exist a number of highly optimized libraries, such as LAPACK [Aa00], and to a lesser extent Numerical Recipes [WPE02], that are well suited for performing many of the computationally demanding tasks such as matrix diagonalization.

Chapter 3

Josephson effect between superconducting nanograins with discrete energy levels

3.1 Introduction

The Josephson effect can be regarded as one of the most striking illustrations of phase coherent behaviour in a macroscopic system and as one of the hallmarks of superconductivity: the flow of a zero-voltage current between two weakly coupled superconductors, with a sign and amplitude that depends on the difference of the phases of their respective order parameter. Although the Josephson effect is in general well understood, there is still a regime in which it has not yet been studied in detail: for superconductors that are so small that the discrete nature of their energy levels becomes important. In this regime, the theory of Bardeen, Cooper and Schrieffer (BCS), which the quantitative understanding of the Josephson effect has been based on, is not applicable.

This is because one of the underlying assumptions in standard BCS theory is the presence of a (quasi-) continuous energy band. As Anderson first pointed out [And59], BCS theory is not consistent anymore once the superconductor is so small that the mean level spacing d is of the order of the superconducting gap Δ_{BCS}: According to BCS theory, the dominant contribution to pairing correlations comes from levels within a range of order Δ_{BCS} around the Fermi surface, but there are no levels left within this range when $d > \Delta_{\mathrm{BCS}}$.

When it became possible to reach this regime experimentally by doing transport measurements on superconducting grains with a diameter of only

a few nanometers [BRT96; vDR01], interest was spurred in a description of the pair-correlated state that is also valid for $d > \Delta_{\mathrm{BCS}}$. It turned out that the BCS interaction in this regime had already been extensively studied in the context of nuclear physics, where an exact solution of the reduced BCS Hamiltonian with discrete energy levels had been found in 1964 by Richardson [RS64].

Using this solution, it was possible to explore in detail the breakdown of BCS (mean-field) theory as d increases. Several surprising insights were gained, one of which being that BCS theory already becomes unreliable when $d \geq \Delta_{\mathrm{BCS}}^2/\omega_{\mathrm{Debye}}$, in other words, long before the Anderson criterion $d \sim \Delta_{\mathrm{BCS}}$ is met [SILvD01]. The underlying reason is that in this regime, BCS theory underestimates the contribution of the so-called "far or distant levels", i.e. energy levels farther away than Δ_{BCS} from the Fermi surface. If the contribution of these levels is properly accounted for, remnants of superconductivity turn out to persist even for $d \geq \Delta_{\mathrm{BCS}}$ – well outside the regime of validity of BCS theory. Indeed, the recent experiments on small superconducting grains [BRT96; vDR01] indirectly confirmed these results: Even for level spacings as large as $d \sim \Delta_{\mathrm{BCS}}$, they observed an even-odd effect (i.e. an energy penalty for states containing an odd numbers of electrons) as a clear indication of remaining superconducting correlations.

Another issue that arises for small superconductors is that the superconducting phase ϕ is not well-defined: When the mean number of electron pairs $\langle N \rangle$ is so small that fluctuations around $\langle N \rangle$ in the grand canonical ensemble are not negligible anymore, N has to be treated as fixed. As a consequence, due to the uncertainty relation $[N, \phi] = i$, the notion of an order parameter with a well-defined phase loses its meaning.

Therefore, a very natural question arises: What is the fate of the Josephson effect between two small superconducting grains, in a regime where BCS theory breaks down, and where the notion of a superconducting phase variable is no longer valid?

In this chapter, this question is examined in detail by studying two pair-correlated grains, coupled by a tunneling term that allows pairs of electrons to tunnel between the grains. To this end, I use the density-matrix renormalization group (DMRG), which has already proven to be useful for calculating the properties of a single superconducting grain [SD00; DS99]. Here, I use it to calculate the ground state of two coupled grains and to extract the Josephson energy. For weak Josephson coupling, also a tight-binding approximation is performed, whose results are compared to those of the DMRG calculation for two coupled grains.

Two competing effects due to the discreteness of the energy levels are identified: Somewhat surprisingly, the Josephson energy is found to be en-

hanced for large level spacing due to the contribution of a single energy level, as long as a certain resonance condition is satisfied. At intermediate level spacing, a kinetic energy term dominates, which suppresses the Josephson energy. The competition of these effects leads to a surprising reentrant behaviour (decrease followed by increase) of the Josephson energy as a function of increasing level spacing. In the limit of vanishing level spacing, the BCS result is recovered.

At this point, I should mention an important restriction on the present analysis: In the regime of small superconductors that is studied here, the charging energy for an electron pair to tunnel between the two superconductors can become huge, easily of the order of a few hundred Kelvin in the experiments of [vDR01]. As will be explained in some detail in subsection 3.2.4, the dominant effect of the charging energy is to suppress tunneling events altogether and thereby to destroy the Josephson effect. However, the interest of the present chapter is to study the effects due to the discrete spacing of the energy levels rather than that of charging effects, which have been thoroughly examined already [AL99; MGG$^+$93; ITJ$^+$89]. Therefore, I set the charging energy to zero.

To experimentally realize the no-charging-energy model studied here, one needs systems for which the mean level spacing is larger than the charging energy. In principle, it is possible to reduce the charging energy somewhat, e.g. by using a pancake-shaped grain geometry, which increases the intergrain capacitance area, or by embedding the grains in a strong dielectric medium. — A more radical and not yet experimentally realized way of studying Josephson physics in the absence of charging effects would be to use uncharged particles instead of electrons, e.g. a degenerate Fermi gas of charge-neutral cold atoms. A "superconducting" phase of cold neutral atoms was observed recently [Lev03; CAR04]; and a natural next step is to apply a double-well trapping potential and to study the Josephson effect in this system, for which the charging energy would indeed be zero.

The remainder of this chapter is organized as follows: In section 3.2, I review the theory of the Josephson effect in a way that is also applicable for small superconductors, for which standard BCS theory is not applicable, and give a definition of the Josephson energy independently of a superconducting phase variable. Section 3.3 discusses how the DMRG method is adapted to the system of two coupled superconductors. Finally, in section 3.4 I present and discuss the results of the calculation.

3.2 Josephson effect for weakly coupled superconductors: Theory

In this section, I review some standard results of the theory of the Josephson effect. The discussion of the Josephson effect is restricted to weak coupling between superconductors, such that perturbation theory in the tunnel coupling (*not* in the superconducting coupling constant) can be applied. However, the Josephson effect is formulated in a way that allows for a straightforward generalization beyond perturbation theory; this is done in subsection 3.2.6.

The physical assumption underlying perturbation theory is that the tunnel coupling between the superconductors is so weak that it is energetically not favourable to create excited states with broken electron pairs in the individual grains. Therefore, the low-energy states of the coupled system will contain these "pair-breaking" excitations only as virtual states. In more quantitative terms, the weak-coupling condition is $E_J^0 \ll \Delta_{\rm sp}$, where $\Delta_{\rm sp}$ is the lowest energy of a pair-breaking excitation, and the Josephson tunneling matrix element E_J^0 is defined in Eq. (3.15) below.

Furthermore, the present discussion of the Josephson effect is formulated independently of the notion of an absolute superconducting phase variable, such that it remains valid in the regime of small superconductors. The material in this section is mostly not new and has been discussed in one way or the other previously [Fer88; dG99], but I feel it is worth presenting it in a way that makes the ensuing application to small grains evident.

3.2.1 Josephson effect as a phase dependent delocalization energy

In the grand canonical ensemble, the phase of a superconductor ϕ can be defined via the action of the pair annihilation operator[1] $b_i = c_{i\uparrow}c_{i\downarrow}$, and the state $|\phi\rangle$ is said to have a phase ϕ if

$$\langle\phi|b_i|\phi\rangle \sim e^{i\phi}, \tag{3.1}$$

ϕ being independent of the state i (this is the case for the ground state of a superconductor). A familiar example is the well-known BCS ansatz wave function $|\phi\rangle = \prod_i (u_i + v_i e^{i\phi} b_i^\dagger)|0\rangle$, where u_i and v_i are real. Eq. (3.1) implies

[1] In general, b_i annihilates a pair of electrons $c_{i\uparrow}c_{\bar{i}\downarrow}$ in time-reversed states $|i,\uparrow\rangle$ and $|\bar{i},\downarrow\rangle$; for the present context of nanograins in the absence of a magnetic field, one may take $i = \bar{i}$.

that a state with definite phase ϕ must be a superposition of many states $|N\rangle$, each of which has a fixed number of electron pairs N:

$$|\phi\rangle = \sum_{N\geq 0} C_N \mathrm{e}^{iN\phi}|N\rangle, \tag{3.2}$$

subject to the condition that $\langle N|b_i|N+1\rangle$ is real, and with real coefficients C_N.

In the canonical ensemble, however, where the number of electron pairs N is fixed, the expectation value (3.1) vanishes, and the notion of a superconducting phase ϕ is obviously not valid. Nevertheless, the concept of a phase *difference* φ between two coupled superconductors ("left" and "right", say) is still applicable, because the number of electron pairs on each individual superconductor needs not be definite as long as the total number on both superconductors is fixed. In analogy to Eq. (3.1), φ can, then, be defined as

$$\langle\varphi|b_r b_l^\dagger|\varphi\rangle \sim e^{i\varphi}. \tag{3.3}$$

Here, the operators b_l and b_r refer to energy levels l, r of the left and right superconductors, respectively. As in Eq. (3.1), one must assume that the phase in Eq. (3.3) is independent of the levels l and r for φ to be well-defined.

An example of a state with definite phase difference φ is, in analogy to Eq. (3.2),

$$|\varphi\rangle = \sum_{\nu=-N/2}^{N/2} C_\nu e^{i\nu\varphi}|\nu\rangle. \tag{3.4}$$

with real coefficients C_ν. Here, the states $|\nu\rangle$ denotes arbitrary states with $N/2-\nu$ pairs on the left and $N/2+\nu$ pairs on the right superconductor, subject to the condition that $\langle\nu|b_r b_l^\dagger|\nu+1\rangle$ is real.

For this work, the states of interest $|\nu\rangle$ have the form

$$|\nu\rangle = |N/2-\nu\rangle_L \otimes |N/2+\nu\rangle_R, \tag{3.5}$$

where $|n\rangle_{L,R}$ are the superconducting *ground states* of the isolated L- ("left") or R- ("right") superconductors, each containing a definite number of pairs, n. These states can always be chosen to satisfy the above reality condition.

As was discovered by Josephson, the presence of a phase difference φ as in Eq. (3.3) has observable consequences when two *bulk* superconductors are coupled: In particular, for weak coupling the coherent tunneling of pairs induces a zero-voltage current,

$$I = I_J \sin\varphi, \tag{3.6}$$

that explicitly depends on φ. As is well known [dG99; Tin96], the Josephson current can, via the relation

$$I = \frac{2e}{\hbar}\frac{\partial E}{\partial \varphi}, \tag{3.7}$$

also be interpreted as a dependence of the total energy E on the phase difference φ. Eq. (3.6) is then equivalent to the energy-phase relation

$$E(\varphi) = \text{const} - E_J \cos\varphi, \quad E_J = (\hbar/2e) I_J \tag{3.8}$$

which will be derived explicitly in 3.2.4 in the bulk limit $d \to 0$. A more general definition of E_J, which is consistent with Eq. (3.8), but also applicable in the small-grain limit, will be given in subsection 3.2.6. There, E_J is associated with the energy gain in the ground state (i.e. $\varphi = 0$) due to the coherent tunneling of electron pairs.

The Josephson energy E_J sets the energy scale relevant for the Josephson effect: It is a delocalization energy that characterizes the coupling of two materials, their tendency to have the same phase and the maximum supercurrent $I_J = (2e/\hbar)E_J$ that can flow between them.

3.2.2 Pair tunneling Hamiltonian

Only processes that depend on the relative phase φ are relevant for the Josephson effect. This is a consequence of Eq. (3.7). Because of Eq. (3.3), such processes require the coherent tunneling of electron pairs; therefore, they have to be treated at least in second order in the tunneling of single electrons. The main goal of this subsection will be to derive an effective pair-tunneling Hamiltonian, Eq. (3.13) below, that arises at this order.

Consider two superconductors L and R (left and right), each having equally spaced energy levels with level spacing d, and each with a reduced BCS interaction with (dimensionless) coupling constant λ:

$$H_L = \sum_{l\sigma} \epsilon_l c^\dagger_{l\sigma} c_{l\sigma} - \lambda d \sum_{ll'} c^\dagger_{l\downarrow} c^\dagger_{l\uparrow} c_{l'\uparrow} c_{l'\downarrow}, \tag{3.9}$$

where $\epsilon_l = l\,d$ is the bare energy of level l, $\sigma = \uparrow, \downarrow$ is the spin, and the sums are over all energy levels closer to the Fermi surface than the Debye energy ω_{Debye}. H_R is defined in analogy to Eq. (3.9); its energy levels shall be labelled by r.

Let L and R be coupled by single electron tunneling with constant tunneling matrix element t,

$$H_{1e} = -td \sum_{lr\sigma} c^\dagger_{l\sigma} c_{r\sigma} + h.c. \tag{3.10}$$

The coupling (3.10) lowers the total energy by generating states such as (3.4) that superimpose different numbers of electrons on each superconductor. Because tunneling occurs only for states near the Fermi energy (up to energy E_J^0, where E_J^0 is defined in Eq. (3.15)), one may cut off the sum in Eq. (3.10) at ω_{Debye} in all numerical calculations below as long as $E_J^0 \ll \omega_{\text{Debye}}$.

States with an odd number of electrons in each grain are energetically unfavourable, the energy cost being at least of the order of the lowest pair-breaking excitation energy Δ_{sp}. For $E_J^0 \ll \Delta_{\text{sp}}$, these states may be integrated out in a similar fashion to Anderson's poor man's scaling [Hew97]. To second order in H_{1e}, the tunneling processes can then be described by the effective tunneling Hamiltonian

$$H_2 = -\sum_{rl\sigma\nu} \frac{H_{1e}|rl\sigma\nu\rangle\langle rl\sigma\nu|H_{1e}}{E_{rl\nu}}, \tag{3.11}$$

acting on the space spanned by the states $|\nu\rangle$, defined in Eq. (3.5). The sum in Eq. (3.11) runs over all possible intermediate states $|rl\sigma\nu\rangle$ that can be reached by removing a single $(r\sigma)$-electron from state $|N/2-\nu\rangle_R$ and adding a single $(l\sigma)$-electron to state $|N/2+\nu\rangle_L$. $E_{rl\nu}$ is the corresponding excitation energy relative to the energy of the state $|\nu\rangle$.

It is shown in chapter 4 that of all matching states (i.e. with quantum numbers r, l, σ, ν), only the one with the lowest energy (called the "No-Gaudino state") gives a significant contribution to the sum in Eq. (3.11). The argument (which is substantiated in chapter 4) goes as follows: In the BCS limit, which is valid for $d \ll \Delta_{\text{BCS}}$, all excited states are described by the quasiparticle operators [Tin96]

$$\gamma^\dagger_{(e)\sigma i} = u_i c^\dagger_{i\sigma} \mp v_i P^\dagger c_{i(-\sigma)}, \quad \gamma^\dagger_{(h)\sigma i} = u_i P c^\dagger_{i\sigma} \mp v_i c_{i(-\sigma)}, \tag{3.12}$$

where $P^\dagger$ is an operator that creates an additional pair, and the upper sign corresponds to $\sigma =\uparrow$, the lower to $\sigma =\downarrow$. . In this limit, it is easy to see that only the lowest energy state $|rl\sigma\nu\rangle = \gamma^\dagger_{(e)\sigma l}\gamma^\dagger_{(h)(-\sigma)r}|\nu\rangle$ gives a contribution to Eq. (3.11), whereas all other intermediate states have a vanishing overlap with $H_{1e}|\nu\rangle$. This is also the case for $\lambda = 0$, where $\gamma^\dagger_{(e)\sigma l}\gamma^\dagger_{(h)(-\sigma)r} = c^\dagger_{\sigma l}c_{\sigma r}$. For intermediate values of λ, no simple argument can be made; it is expected, however, that still the state with the lowest energy will give the dominant contribution.

The energy $E_{rl\nu}$ is given by the collective excitation energies $E_r + E_l$, arising from the fact that levels r and l are singly occupied. In general, it can also include a ν dependent contribution from charging energy due to the electron tunneling; these are discussed comprehensively in [MGG$^+$93]. In

this chapter, however, I chose to consider only situations in which these can be neglected.

In Eq. (3.11), two kinds of tunneling terms are present: on the one hand, terms proportional to $b_l^\dagger b_r$ or to $b_r^\dagger b_l$ that describe coherent pair tunneling, on the other hand, single electron terms proportional to $c_{r\sigma}c_{r\sigma}^\dagger c_{l-\sigma}^\dagger c_{l-\sigma}$ that describe the tunneling of a single electron from l to r and back. When the former terms are applied to a state $|\varphi\rangle$, defined in Eq. (3.4), they produce a phase dependent energy shift. In contrast, the latter terms only lead to a phase-independent energy shift, which is irrelevant for the Josephson effect. For this reason, the single electron terms can be omitted from the Hamiltonian (3.11), as long as only phase dependent processes are of interest [Fer88]. Then, one finally arrives at the pair tunneling Hamiltonian

$$H_J = -2\sum_{rl}\frac{\gamma d^2}{E_r + E_l}(b_r^\dagger b_l + h.c.), \tag{3.13}$$

with $\gamma = t^2$. I shall use for the excitation energies their BCS values, $E_{r,l} = \sqrt{\Delta_{\mathrm{BCS}}^2 + \epsilon_{r,l}^2}$.

3.2.3 Tight-binding model

In the space spanned by all states of the form $|\nu\rangle$ defined in Eq. (3.5), i.e. states without any pair-breaking excitations, the Hamiltonian $H = H_L + H_R + H_J$ looks like a tight-binding Hamiltonian:

$$H = \begin{pmatrix} E(\nu) & -E_J^0/2 & 0 & \dots & \\ -E_J^0/2 & E(\nu) & -E_J^0/2 & 0 & \dots \\ 0 & -E_J^0/2 & & & \\ \vdots & 0 & & & \\ & \vdots & & & \end{pmatrix}, \tag{3.14}$$

where

$$E_J^0/2 = -\langle\nu|H_J|\nu+1\rangle, \tag{3.15}$$

$$E(\nu) = \langle\nu|(H_L + H_R)|\nu\rangle. \tag{3.16}$$

As long as $E_J^0 \ll \omega_{\mathrm{Debye}}$, the off-diagonal elements E_J^0 can be taken to be independent of ν. This is because different values of ν correspond to a different filling of the grain, i.e. to a different position of the Fermi surface with respect to the cutoff at ω_{Debye}. Because much the number ν of tunneled pairs is much smaller than the total number of energy levels N, the cutoff is

always far away, and it does not matter whether the Fermi surface is a few levels closer to or farther away from it.

The diagonal elements are given by

$$E(\nu) = \text{const} + 2d(\nu - \nu_0)^2, \tag{3.17}$$

which has the form of an effective charging energy term. This is because changing ν by one is equivalent to shifting the relative chemical potential between the grains by the amount $2d$ (except the energy level closest to the cutoff ω_{Debye}, which can be neglected for $\nu \ll N$).

3.2.4 Discussion of the tight-binding model

In this subsection, first the above tight-binding model (3.14) is discussed in the limit $d \to 0$, where it is checked that it reproduces the well-known result of Ambegaokar and Baratoff [AB63]. Then, I draw attention to what changes will occur in small superconductors, where the limit $d \to 0$ cannot be performed.

For $d \to 0$, the diagonal elements (3.17) of H_J [Eq. (3.14)] become independent of ν. Also, BCS theory is valid, so the off-diagonal elements (3.15) can be expressed in closed form:

$$E_J^0 = \sum_{lr} \frac{\Delta_{\text{BCS}}^2 t^2 d^2}{E_l E_r (E_l + E_r)} = \Delta_{\text{BCS}} t^2 \pi^2. \tag{3.18}$$

In the left equality of Eq. (3.18), the BCS expression for the matrix elements $\langle \nu | b_l b_r^\dagger | \nu + 1 \rangle = v_l u_l v_r u_r = \Delta_{\text{BCS}}^2 / (2E_l E_r)$ has been used. For the right equality, the sum has been replaced by an integral, $\sum_{ij} = \int_{-\infty}^{\infty} \frac{d\epsilon_1 \, d\epsilon_2}{d^2}$. No harm is done by extending the integral range beyond ω_{Debye} to infinity, because it is naturally cut off at the scale Δ_{BCS} anyway, assumed to be much smaller than ω_{Debye}.

Thus the Hamiltonian of Eq. (3.14) reduces to a tight-binding model with constant coefficients. This model has energy eigenstates of the form of Eq. (3.4) with constant coefficients $C_\nu = \text{const}$. As anticipated in Eq. (3.8), they correspond to an energy $E(\varphi) = \text{const} - E_J^0 \cos\varphi$, and therefore one can identify

$$E_J = E_J^0 = \Delta t^2 \pi^2 = \frac{\pi \hbar \Delta_{\text{BCS}}}{4e^2 R_N} \, . \tag{3.19}$$

The last equality expresses E_J in terms of the normal-state conductance $R_N^{-1} = (4\pi e^2/\hbar) t^2$, and agrees with the well-known Ambegaokar-Baratoff formula [AB63] at zero temperature.

Now I turn to the question what happens when the superconductors enter the regime $d \geq \Delta_{\mathrm{BCS}}^2/\omega_{\mathrm{Debye}}$, in which the BCS ansatz wave function becomes inappropriate [SILvD01]. The transition to this regime is straightforward now, because the tight-binding model itself, Eq. (3.14) - (3.17), remains valid. However, the diagonal and off-diagonal matrix elements $E(\nu)$ and E_J^0, defined in Eq. (3.17) and (3.15), will no longer be given by the BCS expression, but will have to be evaluated using the exact ground state wave function: The effect of the discrete level spacing on the diagonal elements $E(\nu)$, given by Eq. (3.17), will be to lift the degeneracy among them, thereby suppressing pair tunneling.

The off-diagonal elements E_J^0 will change with respect to their BCS value (3.18) due to two distinct effects when the superconductors become small:[2] Firstly, the change in superconducting correlations due to the finite level spacing will affect both the excitation energies E_r and E_l in Eq. (3.13) (which I, however, replace with their BCS value) and the matrix elements $\langle\nu|b_l b_r^\dagger|\nu+1\rangle$ that enter E_J^0. Secondly, the shift of the Fermi level between the states $|\nu\rangle$ and $|\nu+1\rangle$ of the order of d will also affect the matrix elements E_J^0, as is explained in section 3.4.1 below.

As it turns out (see section 3.4.1 below), E_J^0 *increases* for sufficiently large level spacing d, mainly due to the second effect. Once E_J^0 becomes comparable to Δ_{sp} (defined as the lowest pair breaking excitation energy), the superconductors can no longer be considered as weakly coupled, and the tight-binding model itself loses its validity.

3.2.5 The effect of charging energy

As mentioned in the introduction, the Coulomb charging energy plays an important role in small superconductors. Although I shall neglect it in the remainder of this chapter, here I present a brief qualitative discussion of its main effects. The charging energy $E_C = (2e)^2/C$, C being the intergrain capacitance, is the energy cost of tunneling an electron pair from one grain to the other. It introduces an additional term in the Hamiltonian, $E(\nu) = E_C(\nu - \nu_0)^2$. E_C can become huge in the small-grain limit and essentially destroys the Josephson effect, since it suppresses pair tunneling.

Even if a gate is used to make two states $|\nu\rangle$ and $|\nu+1\rangle$ degenerate by a suitable choice of the gate voltage (i.e. $\nu_0 = 1/2$ plus an integer), such that at least one pair can still tunnel between the grains at no energy cost, the

[2] As stated after Eq. (3.12), a third effect will actually take place when the charging energy is taken into account: the excitation energies $E_{rl\nu}$ in Eq. (3.13) will include a term from the charging energy in the intermediate state, as studied in [MGG+93]. I have, however, chosen not to study charging effects at all.

charging energy might nevertheless destroy the Josephson effect altogether: It may cause one electron pair to break into two unpaired electrons, one on each grain, if $E_C > \Delta_{\rm sp}$, i.e. the associated lowering of the charging energy exceeds the energy necessary to form a pair-breaking excitation.

An order-of-magnitude estimate shows that this actually happens in the regime in which the level spacing is important, if no measures are taken to reduce the charging energy: (i) As explained above, the charging energy must be smaller than the lowest energy of a pair breaking excitation, $E_C < \Delta_{\rm sp}$, such that no pair breaking excitations occur. (ii) At least, $\Delta_{\rm BCS} < \sqrt{\omega_{\rm Debye}\, d}$ must be satisfied if the grains are to be small enough so that deviations from BCS become important (the 'weak' criterion in [SILvD01], valid for cumulative properties). (iii) For the present purpose of constructing an order-of-magnitude estimate, I take $\Delta_{\rm sp} \sim \Delta_{\rm BCS}$, although these two energy scales may not be identical in the small-grain limit [SILvD01]. (They differ, for example, by a factor of up to two for the parameter range shown in Fig. 1 of [SILvD01].)

Putting (i), (ii) and (iii) together, the inequality

$$E_C < \sqrt{\omega_{\rm Debye}\, d}, \tag{3.20}$$

which is independent of λ, has to be satisfied.

Let me now explore what this implies for real Aluminium grains: If the inter-grain capacitance is modelled by an Aluminium oxide layer (with dielectric constant $\epsilon \approx 8$) of thickness $D \sim 15$ Å and area πr^2, then $E_C \approx 0.8\ \text{eV}(r/\text{nm})^{-2}$. A smaller thickness D in principle linearly decreases the charging energy, but at the same time, the inter-grain coupling t is exponentially increased [KL73], $t^2 \propto \exp[-D/(0.54\text{Å})]$. Since at a thickness of less than ~ 15 Å, the grains are so strongly coupled that they can no longer be considered as distinct, this distance seems to be a realistic order-of-magnitude lower bound for D. – Using the Debye energy $\omega_{\rm Debye} = 35$ meV for Aluminium, one obtains $\sqrt{\omega_{\rm Debye} \cdot d} = 0.054\ \text{eV}(r/\text{nm})^{-3/2}$, and Eq. (3.20) finally implies $r > 250$ nm if no pair breaking excitations are to occur.

At such a large size, condition (ii) above cannot be met for Aluminium; it is well in the BCS regime. According to criterion (ii), deviations from the BCS approach for a grain of that size would be observable only for a material with $\Delta_{\rm BCS} < 10^{-5}$ eV, an order of magnitude less than Aluminium.

The experiments of Nakamura et al. [NPT99] illustrate the above considerations. They use a superconducting island with $\Delta \approx 230$ μeV and $E_C \approx 117$ μeV: These islands are so small that they are quite close (up to a factor of 2) to the regime where the charging energy would begin to suppress pair tunneling and favour single-particle excitations. Nevertheless, their islands are still large enough to be well described by BCS theory.

However, as mentioned in the introduction, the interest of this chapter is to study the effects due to the discrete spacing of the energy levels, rather than charging effects. Therefore, I henceforth set the charging energy E_C to zero and refer for a more detailed analysis of effects related to E_C to [AL99; MGG$^+$93; ITJ$^+$89].

3.2.6 Generalization to strong coupling

In the weak coupling limit, the Josephson energy was defined via the part of the energy (3.8) that depends on φ. However, Eq. (3.8) is only valid for weak coupling (i.e. in second order in the single electron tunneling). One may equivalently define the Josephson energy as the maximal possible energy lowering due to coherent *pair* tunneling, i.e. when single electron terms are neglected as in the derivation of (3.13):

$$E_J \equiv E_{\text{coupled}} - E_{\text{uncoupled}}. \tag{3.21}$$

This definition agrees with the usual one (3.8) in the weak-coupling regime, because the maximal possible energy lowering occurs at phase difference $\varphi = 0$. Eq. (3.21) allows an extrapolation to strong coupling as well, and therefore I will use it henceforth.

Unfortunately, the pair tunneling Hamiltonian (3.13), being only derived in second order perturbation theory, loses its validity for strong coupling; in general, one would have to use the single-electron tunneling Hamiltonian (3.10) in that case. For simplicity, however, I choose for the strong coupling analysis a somewhat different coupling term that only includes pair tunneling,

$$H'_J = -\frac{\gamma d^2}{\Delta_{\text{BCS}}} \sum_{rl} (b^\dagger_{1r} b_{2l} + h.c.), \tag{3.22}$$

and that differs from the pair tunneling Hamiltonian (3.13) in that the intermediate energy $E_r + E_l$ has been replaced by the constant Δ_{BCS}, such that the prefactor of the pair tunneling term in Eq. (3.22) does not depend on the energy levels l, r.

The Hamiltonians (3.22) and (3.13) are not equivalent. It is nevertheless interesting to study the Hamiltonian (3.22) for several reasons: Firstly, it captures the essential physics of the Josephson effect in a simple way: two superconductors coupled by a tunneling barrier that allows for pair tunneling. Secondly, for $\gamma d/\Delta_{\text{BCS}} = \lambda$, the total Hamiltonian looks just like one single superconductor, thus (3.22) is able to describe the transition to the strong-coupling regime where two superconductors effectively become one. Thirdly, it is amenable to a rather straightforward treatment by the DMRG approach

(in contrast, H_J of Eq. (3.13) would require much more numerical effort), which has the significant advantage of yielding direct access to the regime of strong coupling between the two superconductors.

At weak coupling, a tight-binding analysis for (3.22) similar to the one that led to Eq. (3.18) can be performed. In the large grain limit, one finds the Josephson energy to be

$$E_J^0 = \frac{2\gamma\Delta_{\mathrm{BCS}}}{\lambda^2}, \tag{3.23}$$

independent of the level spacing d. In other words, the Hamiltonian (3.22) has a well-defined continuum limit when γ is held constant as $d \to 0$, as it should.

In section 3.4, I both examine the weak-coupling Hamiltonian of Eq. (3.13) (section 3.4.1), and the cartoon Hamiltonian for strong coupling, Eq. (3.22) (section 3.4.2).

3.3 DMRG approach

In the context of nuclear physics, Richardson found an exact solution [RS64] of the Hamiltonian (3.9) for a single superconductor, that allows in principle to calculate all of its eigenenergies and eigenstates. Because the tight-binding calculation for weakly coupled superconductors, as outlined in 3.2.3, only needs the matrix elements (3.15) between states of a single superconductor, Richardson's solution is, in principle, sufficient for that case.

However, while the eigenenergies of (3.9) can be calculated with only little numerical effort using Richardson's solution, the computation time needed for the eigenstates and for matrix elements like the ones in (3.15) scales like $n!$ with the number of energy levels n in the system, making it effectively impossible to go beyond, say, $n = 12$ levels or so (more precisely, only the number n of energy levels between $E_{\mathrm{Fermi}} - \omega_{\mathrm{Debye}}$ and $E_{\mathrm{Fermi}} + \omega_{\mathrm{Debye}}$ matters). For this reason, despite there being an exact solution available, it is indispensable also for the tight-binding model to have an alternative approach at hand that is approximate, but manageable. Moreover, for the strong coupling analysis in Sec. 3.2.6, that invokes the pair tunneling term (3.22), Richardson's solution is not applicable at all, so that the use of a different approach becomes unavoidable.

For these reasons, I have adopted an approach based on the DMRG method introduced in chapter 2, whose power and efficiency for dealing with pair-correlated nanograins has been demonstrated recently [SD00; DS99]. I use two kinds of DMRG calculations: A single-grain DMRG for calculating the matrix elements (Sec. 3.15) to be used in the tight-binding model

at weak coupling (cf. section 3.2.3), and a two-grain DMRG for the case of strong coupling (cf. section 3.2.6).

In this section, I first discuss some general aspects of the DMRG algorithm in energy space in 3.3.1, leaving some of the more technical issues for appendix A. In Sec. 3.3.2, I discuss the one-grain DMRG, and turn to the discussion of the two-grain DMRG in Sec. 3.3.3.

3.3.1 The DMRG method in energy space

The DMRG in its usual implementation is a real-space renormalization group method, and has been very successfully applied to one-dimensional many-particle quantum systems, such as spin chains [Pes99]. Usually, the Hilbert space for such systems is too large to be diagonalized exactly on a computer. As explained in chapter 2, the DMRG algorithm allows to keep only a reduced part of the Hilbert space that is small enough to be tractable even on a desktop computer, but still sufficient to describe one or several desired states, the so-called target states (in the present case, the ground state will be the target state). This is achieved by progressively increasing the chain size, adding sites one at a time, while only a limited number of states is kept at each step, those states being selected as the most relevant ones for describing the target state(s) in a density matrix analysis.

Although the DMRG is mostly limited to one dimensional systems, it can be applied to three dimensional ones by using the energy axis as the one dimensional "system", such that the bare energy levels play the role of sites on a one dimensional chain. This is not always useful, because the interactions between these "sites" can be much messier than between sites in real space, the latter being generally local. Luckily, as will be seen, the BCS interaction is, although nonlocal, simple enough for the DMRG algorithm to be applicable.

The energy-space DMRG builds up the system, starting from the energy levels closest to the Fermi surface, which are the physically most important ones. Then, the remaining levels are added symmetrically around the Fermi surface, in the order of increasing distance to the Fermi energy. It should be noted that this is quite contrary to the way usual RG calculations are performed, where high energy levels are integrated out, approaching the low energy states from above. This allows these two complementary approaches to be simultaneously applied: As long as not all energy levels have yet been added to the system, only the ones near the Fermi surface are explicitly included in the DMRG calculation. The other ones, which will be included only at later steps, are meanwhile taken into account using a renormalization of coupling constants (as introduced in eq. (43) of [SD00]).

For this purpose, the following scheme turns out to be numerically very efficient for renormalizing the coupling constants λ and γ: When the i levels closest to the Fermi energy are included, choose the coupling constants, say λ_i and γ_i, such that the BCS band gap Δ_i of the current system equals the final value Δ_n, where n is the desired final number of levels. In the DMRG for a single grain, $\Delta_i^{(1)} = id/(2\sinh(1/\lambda_i))$. In the two-grain DMRG, the band gap is given by $\Delta_i^{(2)} = id/\sinh(1/(\lambda_i + \gamma_i d/\Delta_n))$. The latter is the the solution of the BCS gap equation with two different interaction matrix elements $-\lambda_i d$ and $-\gamma_i d^2/\Delta_n^{(1)}$, as in (3.9) and (3.22). This renormalization scheme is not rigorously justified, because it is applied outside the regime of validity of BCS theory. Nevertheless, it turns out to be more efficient than a renormalization of the coupling constants based on a perturbative scheme for large inter-grain couplings, and still performs as well as a perturbative scheme at weak couplings, for which perturbation theory is expected to work.

Another drastic reduction of degrees of freedom occurs because in the model studied here, the energy levels that are occupied by a single electron completely decouple from all the interaction terms (3.9), (3.13) and (3.22). Because the creation of a singly occupied level is associated with the energy Δ_{sp} and therefore energetically unfavourable, there will be no singly occupied levels in the low-energy sector of a superconductor, if one assumes the total number of electrons to be even. Due to these considerations, one may omit these levels from the beginning, and consider only the case of empty or doubly occupied energy levels [vDR01].

Although the full Hilbert space is drastically reduced by the DMRG algorithm, it produces excellent results. In the case of the two-grain DMRG, the accuracy can be checked by comparing the condensation energy from DMRG to the Richardson solution, which is available for two specific values of the inter-grain coupling γ in (3.22), namely for [LH02] $\gamma d/\Delta = \lambda$ (which effectively describes one single, larger superconductor) and $\gamma = 0$ (two independent superconductors). The results for the two-grain DMRG are shown in Fig. 3.1 and show the following features: (i) High precision at strong inter-grain coupling, with a relative error in the condensation energies of only $\sim 10^{-7}$ when $m = 100$ states are kept. (ii) Lower, but still sufficient precision for decoupled grains ($\gamma = 0$): $\sim 10^{-3}$ for $m = 300$, for $n = 100$ energy levels. However, the algorithm fails at weak coupling when the number of energy levels n becomes large ($n > 80 - 150$, depending on the coupling constants), see 3.3.3. In this case, a perturbative calculation (see 3.3.2) becomes necessary.

With the one-grain DMRG, the accuracy of case (i) is obtained. As always in DMRG, the precision can be systematically improved by increasing m.

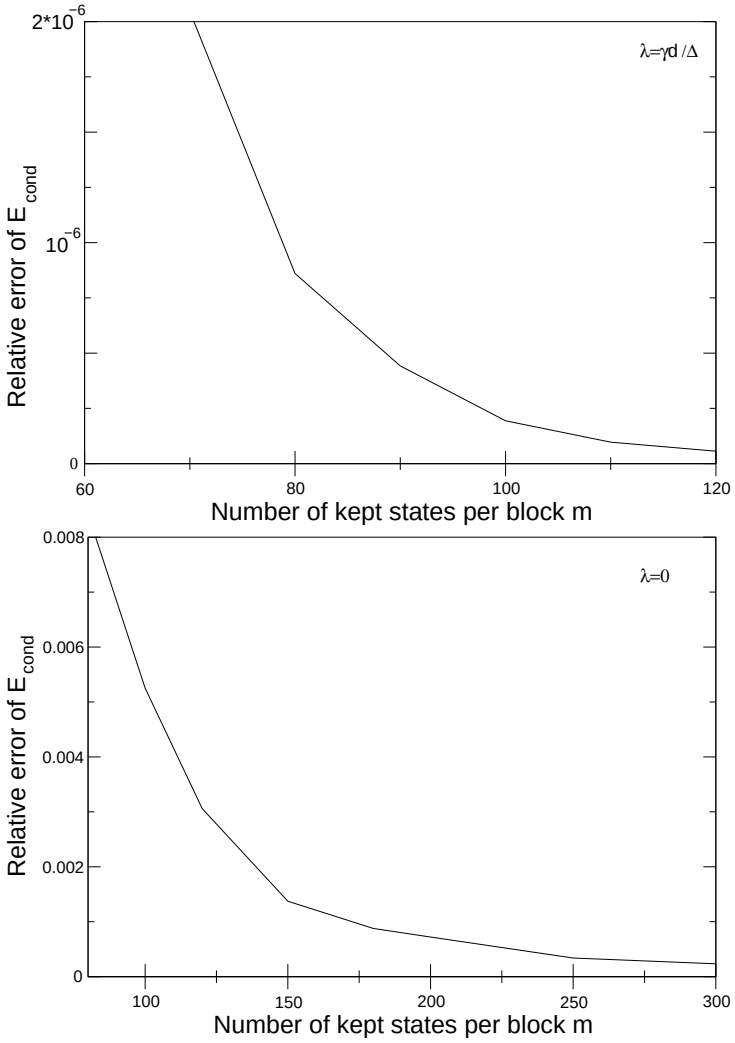

Figure 3.1: Relative error between the exact result from Richardson's solution and the two-grain DMRG at BCS coupling $\lambda = 0.4$, with $n = 100$ energy levels per grain. The inter-grain coupling in the upper plot is $\gamma d/\Delta = \lambda$. In the lower plot, $\gamma = 0$.

3.3.2 One-grain DMRG for tight-binding model

If the grains are weakly coupled, the tight-binding approach can be applied, based on the Hamiltonian (3.13). Here, the microscopic model only enters via the tunneling matrix elements E_J^0 (3.15) of the tight-binding Hamiltonian (3.14). Although these can in principle be calculated exactly using Richardson's solution, in practice the DMRG algorithm is much better suited for that task, as explained above.

Assuming $\nu \ll N$ and using Eq. (3.5), the only matrix elements needed for E_J^0 are $\langle N/2+1|b_i^\dagger|N/2\rangle$ for all values of i. I evaluate these matrix elements using the DMRG algorithm for one single grain, as introduced in Refs. [SD00; DS99]. This requires the simultaneous knowledge of two ground states with different pair occupation numbers, $|N/2\rangle$ and $|N/2+1\rangle$. These states are constructed in a single run, as explained in appendix A. Once these matrix elements have been calculated, it is straightforward to diagonalize the tight-binding Hamiltonian (3.14).

3.3.3 Two-grain DMRG

If the DMRG is directly applied to a system of two grains, the regime of strong coupling can be explored, too. For this purpose, I use the inter-grain coupling term (3.22), introduced in subsection 3.2.6. The exact Richardson solution cannot be applied for this system (except for the particular value of $\gamma = \lambda d/\Delta_{\mathrm{BCS}}$, which has been used in subsection 3.3.1 for checking the accuracy of the results).

Although the two-grain DMRG can cover the previously unaccessible parameter region of strong coupling, it turns out to fail for too weak inter-grain coupling if the system is large (more than, say, 80-150 or so energy levels, depending on the other parameters). The reason is that the DMRG relies on correlations between the grains for being able to effectively reduce the Hilbert space, and these correlations vanish in the limit $\gamma \to 0$. This can easily be seen in the limiting case $\gamma = 0$, in which the two grains L and R are completely uncorrelated and can, each, be described by m_1 independent basis vectors $|1\rangle_L, ..., |m_1\rangle_L$ and $|1\rangle_R, ..., |m_1\rangle_R$. This implies that the m basis vectors retained are essentially product states of the form $|i\rangle_L \otimes |j\rangle_R$, and only an accuracy corresponding to $m_1 = \sqrt{m}$ kept basis vectors per grain is attained. If the inter-grain coupling γ is increased, correlations between grains L and R quickly develop that allow to keep only a few dominant ones of the product states, but for $\gamma = 0$, and also for very small values of γ, each of these states is equally important, making the DMRG highly inefficient. That the DMRG still works even for $\gamma = 0$ if only a few ($< 80 - 150$,

depending on the couplings) energy levels are considered, is due to the fact that in this case, the necessary number of states to be kept per grain seems to be so low ($m_1 \approx 15$) that the ground state can still be reasonably well approximated.

To summarize, the two-grain DMRG works well for strongly correlated systems, but produces unsatisfying results for the case of weak inter-grain coupling. However, this is the regime in which perturbation theory can be used, as described before: thus, the two-grain DMRG and perturbation theory are two complementary approaches; their regimes of usefulness are illustrated in Fig. 3.5 below.

3.4 Results

3.4.1 From small to large grains: The effect of discrete energy levels within the tight-binding model

In this section, I present results from the tight-binding model, which is limited to small inter-grain coupling. I use the Hamiltonian Eq. (3.14), which is derived in that limit from a microscopic model, Eq. (3.10). Fig. 3.2 presents the results for the Josephson energy E_J, defined in Eq. (3.21) as the delocalization energy due to pair tunneling, in the tight-binding approximation. E_J is plotted in units of the BCS result E_J^{BCS}, given by Eq. (3.19). The dashed line in Fig. 3.2 displays the Josephson energy as a function of decreasing level spacing d, i.e. of increasing grain size, characterized by the number of discrete energy levels n between $\varepsilon_F \pm \omega_{\text{Debye}}$.

While the level spacing d is varied, the parameters λ and γ in (3.13) are held fixed (at the values $\lambda = 0.3$, $\gamma = 0.05$), such that the BCS value in Eq. (3.18) of E_J is independent of the grain size, and a well-defined limit $d \to 0$ exists.

Within the tight-binding model, one observes two competing effects, to be discussed in detail below, that influence the Josephson energy as the level spacing d increases (i.e. moving toward the left side of Fig. 3.2): (i) On the one hand, the finite-size kinetic energy term $E(\nu)$ of Eq. (3.17) increases, which tends to reduce the Josephson energy E_J; (ii) on the other hand, the off-diagonal matrix element E_J^0 in Eq. (3.14) increases (as shown in Fig. 3.2, dotted line), which tends to increase E_J. The combination of these two tendencies leads to the reentrant behaviour seen in Fig. 3.2, particularly in the inset, with a remarkable *increase* in E_J when d becomes sufficiently large.

The kinetic term (i) was discussed in section 3.2.3. I chose ν_0 in Eq. (3.17)

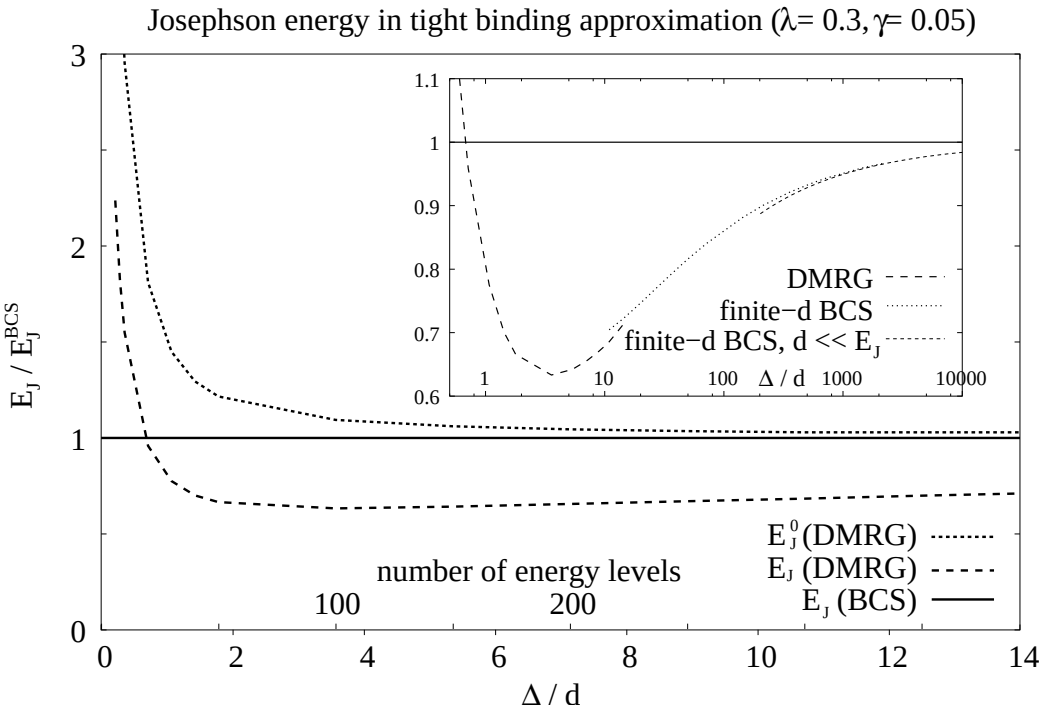

Figure 3.2: The Josephson energy E_J in the tight-binding approximation, based on Eq. (3.14), as a function of the grain size. E_J is defined via Eq. (3.21) as the additional energy gain due to coherent pair tunneling and is normalized to the BCS result E_J^{BCS} in Eq. (3.19). Compared to the off-diagonal matrix element E_J^0 (dotted line), E_J (dashed line) is reduced by a factor of up to 2 due to the finite-size kinetic energy term $E(\nu)$ of Eq. (3.17). The logarithmic plot in the inset shows how the BCS result of Eq. (3.19) is recovered as $d \to 0$.

as $\nu_0 = 1/2$, such that the two lowest-lying states are degenerate and at least one pair can tunnel at no energy cost between these states no matter how large d is. For this case, the total reduction of the Josephson energy due to the finite-size kinetic term amounts to a factor of at most 2, even for very large level spacing d. This is because for $d \to \infty$, all but the lowest two states "freeze out", so that the tight-binding Hamiltonian (3.14) effectively reduces to a two-level system for the states $|\nu = 0\rangle$ and $|\nu = 1\rangle$, whose tunnel splitting is $E_J^0/2$ (hence the reduction by a factor of 2). Nevertheless, the reduction in Fig. 3.2 is seen to be considerable even for fairly large grains (still of order 20 % for $\Delta_{\mathrm{BCS}}/d \sim 100$, corresponding to $n \sim 3000$ levels), because it depends on the ratio d/E_J^0, where E_J^0 typically is a small number itself. For $d \ll E_J$, the asymptotic behaviour $E_J = E_J^0(1 - \sqrt{2d/E_J^0})$ (thin dashed line in the inset of Fig. 3.2) is found in analogy to the treatment of small charging energies in section 7.3 of [Tin96], by using an ansatz wave function given by Eq. (3.4) with $\varphi = 0$ and C_ν of Gaussian form. This ansatz wave function turns out to be asymptotically correct for $d \ll E_J^0$ [Tin96].

Next, I discuss the increase of E_J^0 in the small-grain limit (ii). It is due to the fact that matrix elements $\langle N_L|b_l|N_L+1\rangle$ (and likewise $\langle N_R+1|b_r^\dagger|N_R\rangle$) that contribute to E_J^0 in Eq. (3.15) are taken between states with the number of electron pairs differing by 1. This fact is unimportant in standard BCS theory, where the total number of pairs is assumed to be macroscopically large anyway. When the level spacing d becomes large, however, this is the main reason for the increase of E_J^0:

The increase of E_J^0 is easy to understand for the Fermi state ($\lambda = 0$) and in the BCS limit ($\lambda > 2/\ln N$, see [SILvD01]). In the Fermi state, the matrix element $\langle N|b_i|N\rangle$ is zero for all values of i, but $\langle N|b_i|N+1\rangle$ gives a contribution of 1 for the one level $i = i_N$ that is below the Fermi surface of $|N+1\rangle$ and above the Fermi surface of $|N\rangle$. In the BCS case, the matrix element is given by $\langle N|b_i|N+1\rangle = u_i^N v_i^{N+1}$. The upper indices on u and v, N and $N+1$, indicate the total pair occupation numbers of the respective states, the effect being that v^{N+1} has the chemical potential shifted upwards with respect to v^N by the level spacing d. Thus, the product $u_i^N v_i^{N+1}$ becomes larger as the level spacing d increases, as is illustrated in Fig. 3.3. I call this modification of the BCS calculation the "finite-d" BCS calculation.

In Fig. 3.3, the finite-d BCS matrix elements (solid line) are also compared to the exact values obtained using the DMRG (filled dots). The comparison shows that for the levels close to the Fermi energy (i.e. the central level i_0 and the next, say, 2 levels), the finite-d BCS result overestimates the pairing correlations: the (quasi-)exact DMRG solution is seen to have a more pronounced peak at the central level i_0, whereas the contribution of the neighbouring two levels is somewhat reduced, resembling, for these levels, qualitatively

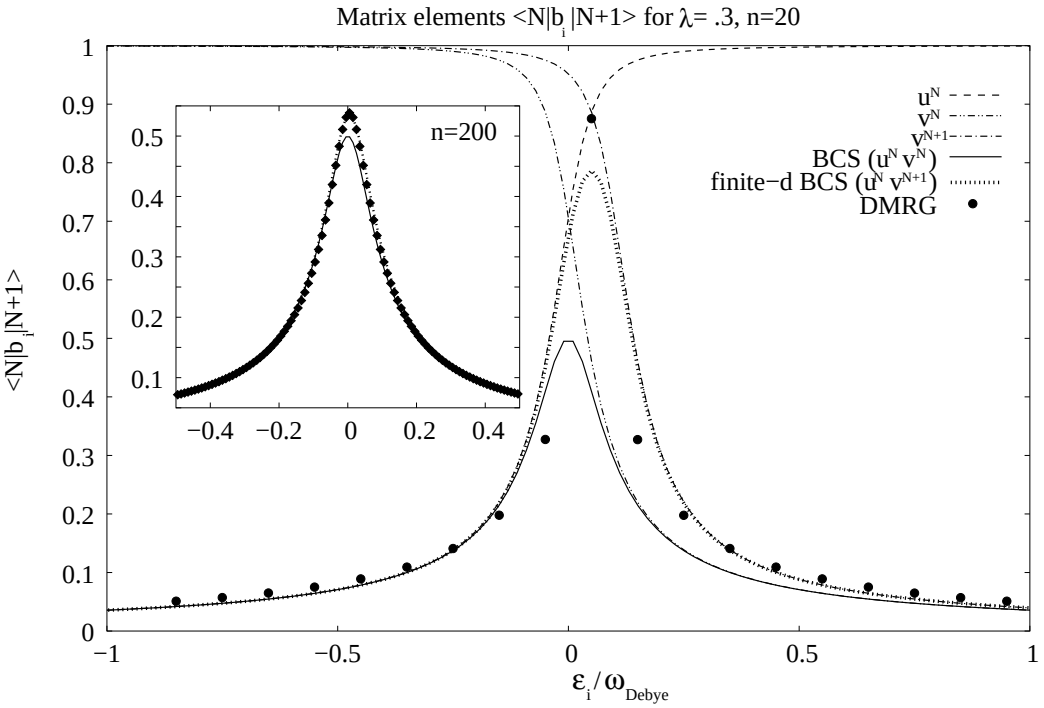

Figure 3.3: Various approximations for the matrix element $\langle N|b_i|N+1\rangle$ are compared. The product of the BCS coherence factors $u^N v^N$ (BCS, thin dashed line) is compared to $u^N v^{N+1}$ (finite-d BCS, solid line) in a grain of $n = 20$ levels. Because v^{N+1} in the latter product is shifted to the right by an amount of d with respect to v^N, the finite-d curve must obviously be larger than the BCS curve for all values of i. Also shown (filled dots) are the exact matrix elements $\langle N|b_i|N+1\rangle$, calculated using the DMRG approach. The inset compares the BCS, the finite-d BCS and the DMRG results for a larger grain with $n = 200$ levels. While the finite-d BCS curve shows excellent agreement with the quasiexact DMRG result in this regime, the standard BCS curve still deviates from it.

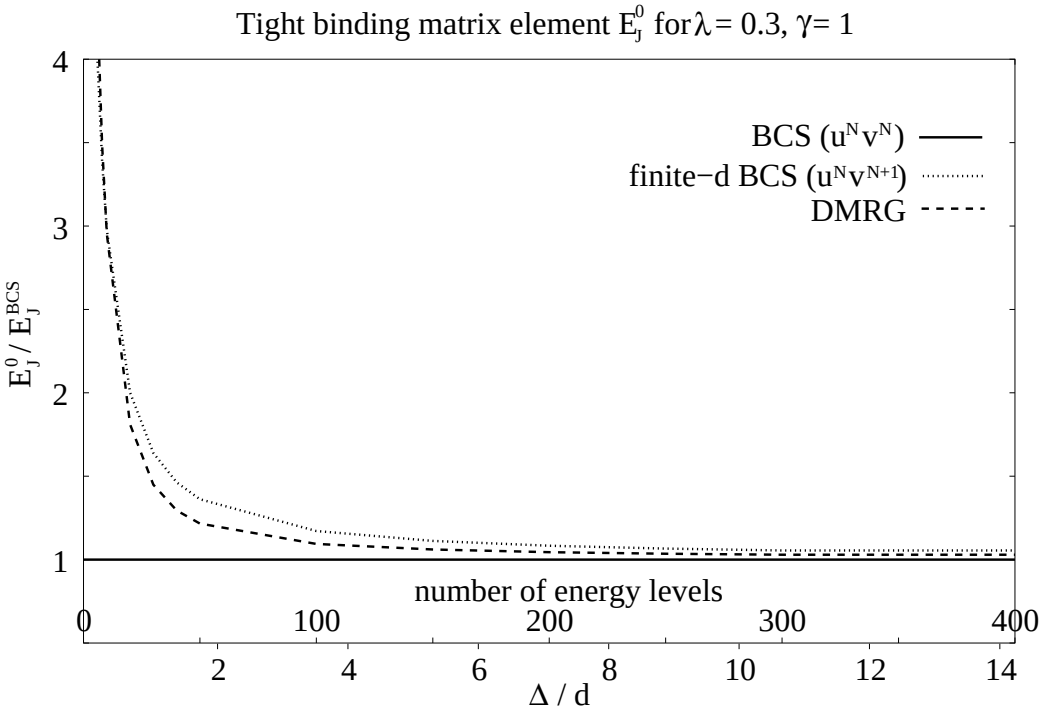

Figure 3.4: E_J^0 is evaluated in the BCS, the finite-d BCS and the DMRG method. Although BCS theory is not valid in the regime of large level spacings d, the finite-d-BCS reproduces, at least qualitatively, the correct behaviour seen in the DMRG curve.

more closely the $\lambda = 0$ case discussed above. For the energy levels further away from the Fermi energy than that, the finite-d BCS calculation is seen to slightly underestimate the matrix elements. This is not unexpected, because BCS theory is known [SILvD01] to underestimate the superconducting correlations of energy levels much farther away from the Fermi surface than Δ_{BCS}, which for the parameters of Fig. 3.3 is $\Delta_{\mathrm{BCS}} \approx 0.07\omega_{\mathrm{Debye}}$.

E_J^0, however, being a weighted sum over all products of these matrix elements, is nevertheless not so far off in the finite-d BCS approach even for very small grains, as can be seen in Fig. 3.4. This is surprising and somewhat fortituous, since the BCS theory does not self-consistently describe the grains in the limit that they are small. The reason that the finite-d BCS works so well seems to be that the underestimation of the matrix elements for level i_0 and and their overestimation for the other levels cancel each other to a large degree.

In conclusion, the main reason why E_J^0 increases as the grains become small is very simple: the chemical potential of the grains shifts due to the finite level spacing whenever a pair tunnels from one grain to the other. Note that the BCS ansatz without taking this effect into account is not accurate near the Fermi energy even for fairly large grains (see the inset in Fig. 3.3), for which the finite-d BCS theory agrees perfectly with the DMRG result.

The competition between the finite-size kinetic term on the one hand and the increase of E_J^0 on the other leads to the reentrant behaviour of E_J as seen in Fig. 3.2. This is one of my main results. Two regimes can be distinguished as a function of Δ_{BCS}/d: For very small grains ($\Delta_{\mathrm{BCS}}/d < 1$), superconducting correlations are only weakly present, but the 1-level effect outlined above leads to a strong enhancement of E_J^0 and, therefore, of the Josephson energy E_J. Despite not being a well-justified approximation in this regime, the finite-d BCS result nevertheless gives a surprisingly good estimate of the Josephson energy. On the other hand, for larger values of Δ_{BCS}/d ($>$ 10, say), E_J^0 is almost constant and very close to the BCS value. The kinetic energy term in Eq. (3.17), however, reduces the Josephson energy below the BCS value, and vanishes only rather slowly. The reentrant behaviour of E_J occurs at the intermediate region $1 < \Delta_{\mathrm{BCS}}/d < 10$, in which both effects are competing, and in which E_J^0 is slowly approaching its BCS value from above.

3.4.2 Limitations of the tight-binding approach

The tight-binding approximation, which neglects excitations of the individual grains, is valid only for small couplings, such that E_J^0 lies well below the lowest excitation energy Δ_{sp}. In Fig. 3.2, however, E_J^0 is seen to grow strongly with

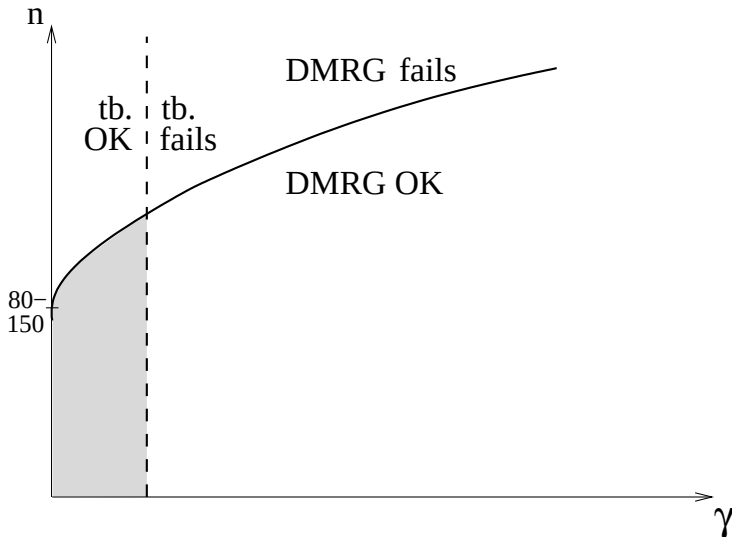

Figure 3.5: A rough sketch of the regimes of validity for the DMRG and the tight-binding approach in parameter space (inter-grain coupling γ vs. the number n of energy levels). There is only a small overlap (shaded region) at small γ and small n, in which both approaches simultaneously work well.

increasing level spacing d. Thus, for sufficiently large d, the tight-binding approach invariably becomes unreliable, and a different method is needed. In order to complement the tight-binding approach and to check its quality, I apply the two-grain DMRG solution that does not rely on the inter-grain coupling being weak.

The DMRG, however, has its own limitations, as was explained in subsection 3.3.3: Firstly, it requires a pair tunneling Hamiltonian (3.22) that describes a somewhat different model. This implies, of course, that it has to be compared to a tight-binding model using the same pair tunneling Hamiltonian as well. Secondly, as discussed in section 3.3.3, the two-grain DMRG can break down at small couplings if the number of energy levels is large, for precisely the same reason that the tight-binding model works well: The correlations between the two grains, which the DMRG relies on, become very weak.

The regimes of validity of the two complementary approaches are schematically depicted in Fig. 3.5. The tight-binding method only works well at small coupling, $\Delta_{\mathrm{sp}} \ll E_J$ (region left of dashed line), whereas the DMRG works well only at large coupling (region right of solid line). A simple (analytical) condition for the validity of the DMRG approach cannot be given, which is why the axes in Fig. 3.5 are drawn without units. However, the quality of

the DMRG approach is found to depend sensitively on the number of energy levels n. In particular, the DMRG turns out to be reasonably accurate for all values of γ down to 0, as long as $n < 80 - 150$ (depending on other parameters), as is motivated in subsection 3.3.3 and seen in Fig. 3.6 and Fig. 3.7.

In Fig. 3.6 and Fig. 3.7, the tight-binding approximation for the Josephson energy is compared to the two-grain DMRG as a function of the grain size, for two different values of the inter-grain coupling γ (corresponding to vertical lines in Fig. 3.5). The Josephson energies are again plotted in units of their BCS values, now given by Eq. (3.23). In Fig. 3.6, both methods are seen to agree for small numbers of energy levels, $n < 80 - 100$. For larger values of n, the two-grain DMRG breaks down, for the reasons outlined in 3.3.3. The DMRG method itself signals its own breakdown: Convergence as function of the kept DMRG states m is no longer achieved, as a comparison of the two curves in Fig. 3.6 corresponding to $m = 330$ and $m = 360$ reveals.

Because both the two-grain DMRG and the tight-binding approach are ultimately variational methods, the one that produces the higher value of E_J (i.e. the lower total condensation energy) must be the better approximation. Also in this respect, the DMRG method is seen to be failing for $n > 80 - 100$ in Fig. 3.6, in agreement with Fig. 3.5.

Fig. 3.7 shows the result of a similar calculation as Fig. 3.6, at a higher value of the inter-grain coupling $\gamma = 0.01$. Now, the two-grain DMRG is seen to be valid up to somewhat larger values of n. For small n, $n < 100$, the DMRG now produces a higher value of E_J, indicating that in this regime, it produces a better result than the tight-binding method, as anticipated in Fig. 3.5.

The results from Fig. 3.6 and Fig. 3.7 are similar to the ones in Fig. 3.2, where only a tight-binding calculation had been performed. In particular, the two-grain DMRG reproduces the increase in E_J for small values of n, corresponding to large level spacing d, and thereby confirms the reentrant behaviour observed in the tight-binding approach (cf. Fig. 3.2).

In Fig. 3.8, the tight-binding and the two-grain DMRG results are plotted as a function of the inter-grain coupling γ (corresponding a horizontal line in Fig. 3.5). The plot is extended to very large values of the inter-grain coupling γ in order to show the point at which the two-grain DMRG can be compared to the exact result at $(d/\Delta_{\mathrm{BCS}})\gamma = \lambda$, which it reproduces nicely. I emphasize that in the regime of large γ, some of the physical assumptions (e.g. the use of a tunneling Hamiltonian) of the present calculation are not justified anymore, and that the plot in that regime has no other physical significance than to provide an important cross check for the DMRG.

The exact result at $(d/\Delta_{\mathrm{BCS}})\gamma = \lambda$ describes the two grains as a single

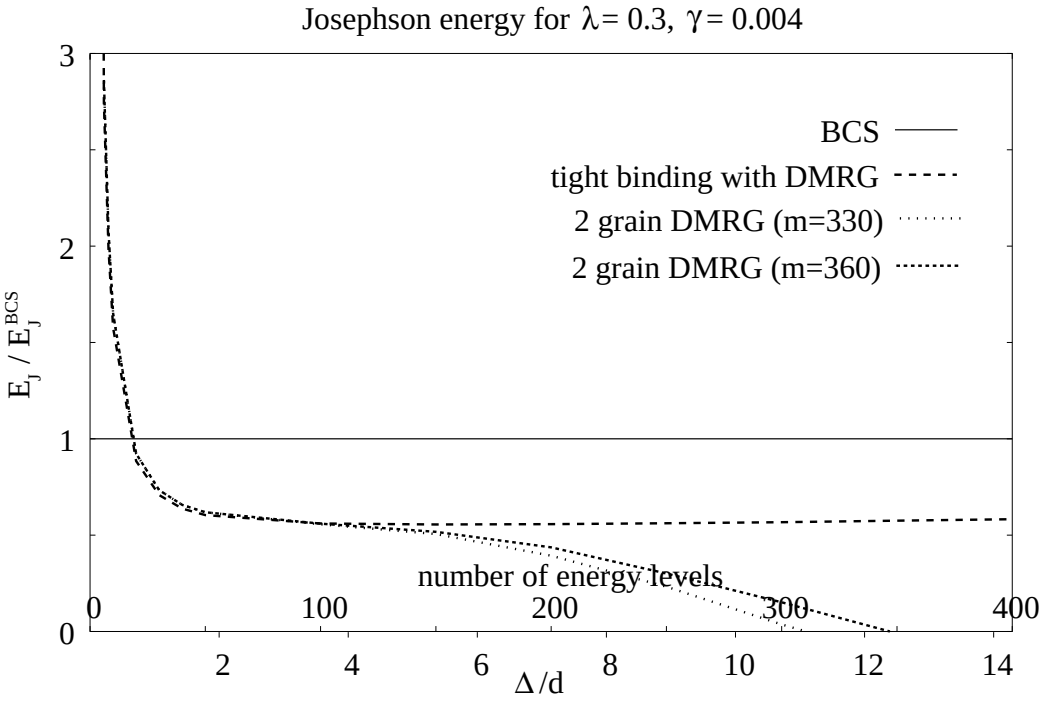

Figure 3.6: The Josephson energy is calculated in the tight-binding and in the DMRG approach. In agreement with Fig. 3.5, both curves agree if the number of energy levels n is small, but the DMRG fails for $n > 80 - 100$.

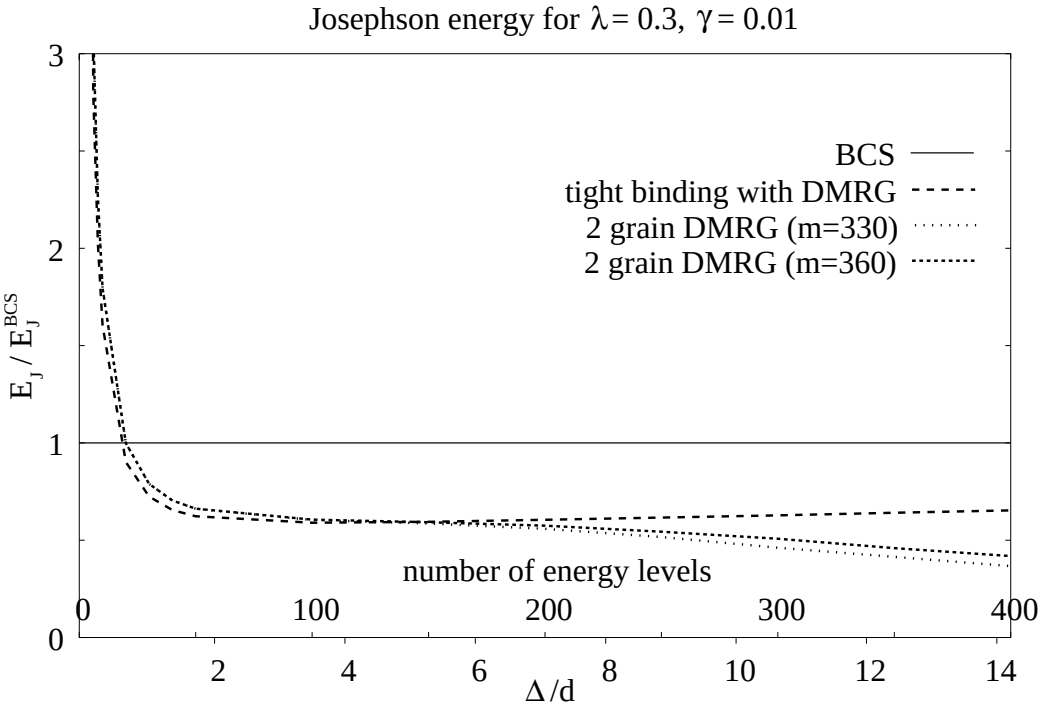

Figure 3.7: Same calculation as in Fig. 3.6, but at larger inter-grain coupling. Now, the DMRG has a somewhat larger range of validity. For small grains, the DMRG curve lies higher (i.e. the tight-binding approach is not as good as the DMRG anymore).

superconductor with half the level spacing $d_2 = d/2$ and with the interaction Hamiltonian

$$H_2 = -\lambda_2 d_2 \sum_{i\in R,L,\ j\in R,L} b_i^\dagger b_j, \tag{3.24}$$

with $\lambda_2 = 2\lambda$. In the large-coupling regime, the Josephson energy $E_J = E_{\mathrm{cond},2} - 2E_{\mathrm{cond},1}$ is entirely dominated by the condensation energy $E_{\mathrm{cond},2}$ of the large superconductor described by Eq. (3.24), which is much larger than the condensation energies $2E_{\mathrm{cond},1}$ of the isolated grains (i.e. for $\gamma = 0$). In the BCS limit, $E_J \approx E_{\mathrm{cond},2} = \omega_{\mathrm{Debye}} n \sinh^2(1/\lambda_2)$. In particular, E_J is seen to be an extensive quantity, i.e. $E_J/\omega_{\mathrm{Debye}} \propto n$ for the particular choice $\gamma = (\Delta_{\mathrm{BCS}}/d)\lambda$, for which the two superconductors are described as one. In this case the inter-grain coupling acts like a bulk term (and no longer as a surface effect), which is manifest in the way that γ scales with the system size: γ scales no longer as a constant, but with the volume of the system.

As is evident from Fig. 3.8, the tight-binding method, which is only applicable at very small values of γ, ceases to be valid long before the point $(d/\Delta_{\mathrm{BCS}})\gamma = \lambda$ is reached. The inset of Fig. 3.8 shows an enlargement of the main figure for small γ. It is seen that for $E_J^0 \ll \Delta_{\mathrm{BCS}}$, the results from the tight-binding method and from the DMRG agree, as expected.

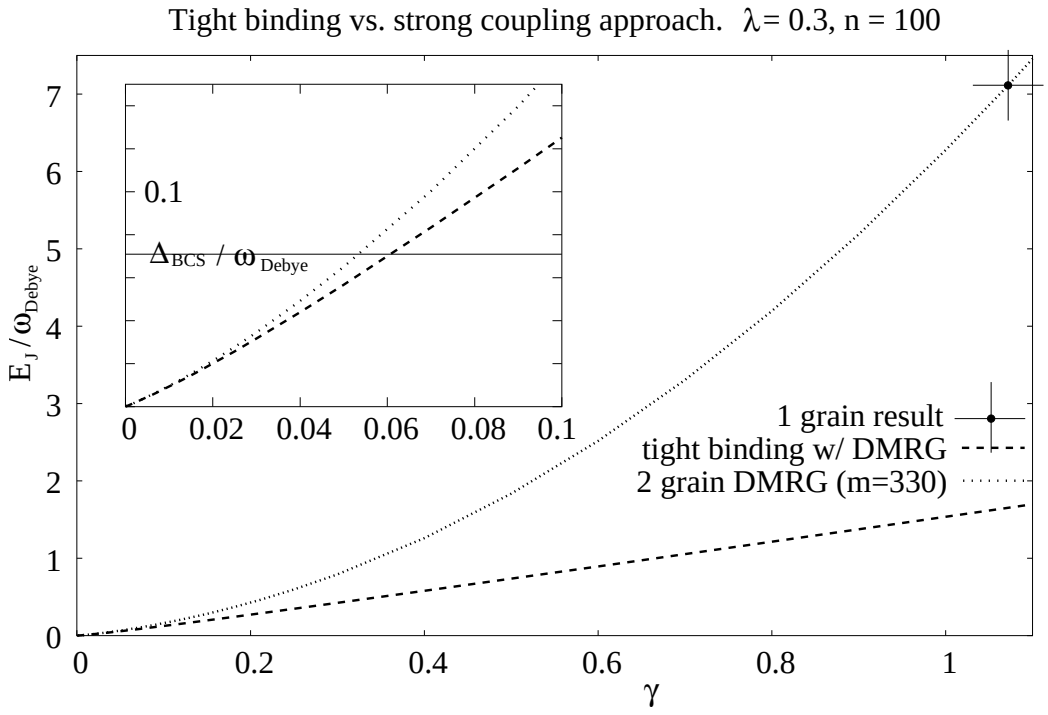

Figure 3.8: The Josephson energy is plotted as a function of the inter-grain coupling γ in grains that are small enough so that the DMRG approach works for all values of γ down to zero. Once the coupling is too large ($\gamma \gtrsim 0.06$), the tight-binding model fails as asserted in Fig. 3.5. The inset shows an enlargement for small values of γ, and illustrates the condition $E_J \ll \Delta_{\rm sp} \sim \Delta_{\rm BCS}$ for the tight-binding model to be valid, which was motivated at the beginning of section 3.2

.

Chapter 4

Well-defined quasiparticles in interacting metallic grains

4.1 Introduction

The pairing Hamiltonian of Bardeen, Cooper and Schrieffer (BCS), Eq. (4.1), is established as the paradigmatic framework for describing superconductivity [CBS57; Tin96]. The BCS *solution* is, however, an approximate one, valid (and exceedingly successful) only as long as the mean level spacing d is much smaller than the superconducting band gap Δ_{BCS} [vDR01; SILvD01]. One of the main features of the BCS solution is the description of the excitation spectrum by well-defined (i.e. infinite-lifetime) Bogoliubov quasiparticles, responsible for many of the features of the superconducting state.

In this chapter, I address the question whether this quasiparticle picture prevails in the entire regime of parameters – including the case that the samples are so small or so weakly interacting that $d \geq \Delta_{\mathrm{BCS}}$, and the BCS solution is inapplicable – by analyzing spectral functions. For example, the spectral function corresponding to the (noninteracting) particle creation operator $c^{\dagger}_{k\sigma}$ is given, within the BCS solution, by a sharp line in k-ω-space; this reflects the infinite lifetime of the quasiparticles. For an interacting system, this is a very peculiar property, since the interactions usually shift a significant portion of the spectral weight to a background of excitations, responsible for the finite lifetime of the quasiparticles. Here I show that the unusual property of finding well-defined quasiparticles persists to a very good approximation over the entire parameter range of the pairing Hamiltonian Eq. (4.1), and is not merely a property of the mean field approximation in the BCS regime. I also give a condition for more general spectral functions to show analogous behaviour.

Of central importance is that this result is relevant not only in the context of mesoscopic superconductivity, but more generally for disordered systems with large dimensionless conductance g. (Here, g is given by the ratio between the Thouless energy E_T and the mean level spacing d, and large values of g indicate that a system is a good conductor [ABG02]). This is because to lowest order in g^{-1}, the electron-electron interactions can be described by a remarkably simple "universal Hamiltonian" [KAA00; ABG02] which has (besides the kinetic energy term H^0) only three couplings:

$$\begin{aligned} H &= H^0 + H^c + H^s + H^p, \text{ where} \\ H^0 &= \sum_{i\sigma} \epsilon_i c^\dagger_{i\sigma} c_{i\sigma}, \\ H^c &= E_c(\hat{n} - N_0)^2, \\ H^s &= J_s \hat{\vec{S}}^2, \\ H^p &= -\lambda d \sum_{i,j\in\mathcal{N}} c^\dagger_{i\uparrow} c^\dagger_{i\downarrow} c_{j\downarrow} c_{j\uparrow}. \end{aligned} \tag{4.1}$$

Here, $\hat{n}$ and $\hat{\vec{S}}$ are the electron number and the total spin operator, and E_c, J_s and $-\lambda d$ are coupling constants. Although λ may have either sign, the present analysis is restricted to the case of positive λ only. The sum includes all energy levels around the Fermi energy ϵ_F up to some cutoff $\omega_{\rm co}$ at the Thouless energy, denoted by the set $\mathcal{N}$. It turns out that H^c and H^s do not affect my results, because they commute with $H^0 + H^p$ and thus leave the eigenstates invariant. Therefore, it suffices to take H^p – the BCS pairing Hamiltonian – as the only interaction term. Thus, the difference between the BCS model and the universal Hamiltonian is for the present purposes only in the cutoff $\omega_{\rm co}$, being at the Debye energy for the former and at the Thouless energy for the latter. In either case, I define $\Delta_{\rm BCS} = \omega_{\rm co} e^{-1/\lambda}$.

The fact that the zero-temperature spectral function $\mathcal{A}_{\hat{O}}(\omega)$ of an operator $\hat{O}$ is sharply peaked translates to a strong condition on the matrix elements of the Lehmann representation, which is given (for $\omega > 0$) by

$$\mathcal{A}_{\hat{O}}(\omega) = \sum_{|I\rangle} \langle {\rm gs}|\hat{O}^\dagger|I\rangle\langle I|\hat{O}|{\rm gs}\rangle \delta(\omega - E_I). \tag{4.2}$$

Here $|{\rm gs}\rangle$ denotes the ground state, $|I\rangle$ the excited states with energies E_I. For only one sharp peak to be present in the spectral function, the sum in Eq. (4.2) must be dominated by one single eigenstate, say $|I\rangle^0$, whereas all other states $|I\rangle \neq |I\rangle^0$ do not contribute. Obviously, it will depend on the operator $\hat{O}$ whether this is the case, and if so, which is the state $|I\rangle^0$. I

show that it suffices that $\hat{O}$ satisfies a rather unrestrictive condition, given after Eq. (4.5) below and fulfilled for many physically relevant quantities. Furthermore, I show that under this condition, the state $|I\rangle^0$ is from a very limited subset of all possible excitations, which I characterize in section 4.2 below as the "No-Gaudino states". The finding of well-defined quasiparticles therefore implies that only these No-Gaudino states are relevant for many physical properties of systems that satisfy the conditions of the universal Hamiltonian.

Calculating the spectral function nonperturbatively (e.g. by the route of Eq. (4.2)) is usually a formidable task, equivalent to diagonalizing the full Hamiltonian. Although an exact solution [RS64; vDR01] exists for the Hamiltonian H^p of Eq. (4.1), its complexity in practice does not allow to calculate spectral functions. Instead, I use for this purpose the density-matrix renormalization group (DMRG) method outlined in chapter 2. Details about the adaptation of the method to the present problem are given in section 4.3. For suitable operators $\hat{O}$, the method presented here allows to obtain the spectral function from the DMRG without the usual complications [KW99; Jec02], because the state $|I\rangle^0$ – the only one that contributes significantly to the spectral function – can be constructed explicitly. In section 4.4, I quantify the contribution of other states $|I\rangle \neq |I\rangle^0$ by using a sum rule, which turns out to be negligibly small. Finally, I illustrate in section 4.5 the use of the possibility of calculating spectral functions by evaluating the tunneling density of states and the magnetic response of mesoscopic rings.

4.2 Excitation spectrum, No-Gaudino states

Let me begin by describing the excitations of the Hamiltonian H^p in Eq. (4.1). H^p has the well-known property that singly occupied energy levels do not participate in pair scattering. Therefore, their labels (and spins) are good quantum numbers. Therefore, the eigenstates factorize into one part living on the singly occupied levels and another part living on the remaining, i.e. the doubly occupied or empty levels. Hereby, the singly occupied levels decouple from the interaction with the other levels. More explicitly, each state $|\psi^{\mathcal{B}}_{\mathcal{N}}\rangle$ with singly occupied levels, say, $\mathcal{B} = \{j_1, \cdots, j_l\}$ (with spins $\sigma_1, \cdots, \sigma_l$) out of a total set of energy levels $\mathcal{N}$ can be mapped onto a particular state $|\psi^{\emptyset}_{\mathcal{N}\setminus\mathcal{B}}\rangle$ in a Hilbert space with levels $\mathcal{B}$ removed (i.e. with $\mathcal{N}$ replaced by $\mathcal{N} \setminus \mathcal{B}$ in Eq. (4.1)), but with no singly occupied levels, via the mapping

$$|\psi^{\mathcal{B}}_{\mathcal{N}}\rangle = c^\dagger_{j_1\sigma_1} \cdots c^\dagger_{j_l\sigma_l} |\psi^{\emptyset}_{\mathcal{N}\setminus\mathcal{B}}\rangle. \tag{4.3}$$

A given state can thus contain two kinds of excitations: Pair-breaking

excitations that go hand in hand with a change of the quantum numbers $\mathcal{B}$, and other many-body excitations that do not change $\mathcal{B}$, but instead contain excitations within the state $|\psi^{\emptyset}_{\mathcal{N}\setminus\mathcal{B}}\rangle$ in Eq. (4.3). The latter were studied in [RSD03] and dubbed "Gaudinos". In this spirit, I define the No-Gaudino state as the lowest-energy state within a certain sector of the Hilbert space characterized by the quantum numbers $\mathcal{B}$, i.e. the state that is mapped via Eq. (4.3) onto the ground state $|\psi^{\emptyset}_{\mathcal{N}\setminus\mathcal{B}}\rangle = |\mathrm{gs}^{\emptyset}_{\mathcal{N}\setminus\mathcal{B}}\rangle$. For example, the No-Gaudino state with no singly occupied levels, $\mathcal{B} = \emptyset$, is trivially given by the ground state itself.

In the BCS limit, the No-Gaudino state of the form of Eq. (4.3) is given by

$$|j_1^{\sigma_1} \cdots j_l^{\sigma_l}\rangle^0 \approx \gamma^\dagger_{j_1\sigma_1} \cdots \gamma^\dagger_{j_l\sigma_l} |gs\rangle_{\mathrm{BCS}}, \tag{4.4}$$

where $|gs\rangle_{\mathrm{BCS}}$ is the BCS ground state and γ are the Bogoliubov quasiparticle operators from BCS theory [Tin96]. As is shown below, these states are easily obtained within the DMRG algorithm.

Let me now specify under which condition the spectral function, Eq. (4.2), is dominated by such a No-Gaudino state. Any operator can be written as a linear superposition of operators

$$\hat{O} = c_{i_1\sigma_1} \cdots c_{i_k\sigma_k} c^\dagger_{j_1\sigma'_1} \cdots c^\dagger_{j_l\sigma'_l}. \tag{4.5}$$

Let me first consider single operators $\hat{O}$; linear superpositions will be discussed at the end of this section. *The central condition that must be imposed on $\hat{O}$ is that all indices $i_1, \cdots, j_l$ be mutually different.* $\hat{O}$ then takes a state with no singly occupied levels, $\mathcal{B} = \{\}$, to the sector of the Hilbert space characterized by $\mathcal{B} = \{i_1, \cdots, j_l\}$. I show below that under the above condition, $\hat{O}$ moreover has the crucial property that when acting on the ground state, it creates to an excellent approximation just the No-Gaudino state in this sector, see Fig. 4.1 for an illustration. Therefore, the state $\hat{O}|\mathrm{gs}\rangle$ contributing to the spectral function, Eq. (4.2), is seen to be not only a well-defined eigenstate of the system, but moreover a No-Gaudino state. This is my central result. It is ultimately based on the large number of good quantum numbers in the universal Hamiltonian model: they subdivide the Hilbert space into "narrow" sectors, each of which is well represented by the respective No-Gaudino state. Note that the condition stated after Eq. (4.5) excludes operators such as $\hat{O} = c^\dagger_{i\sigma} c_{i\sigma}$. Such operators do have a substantial amplitude of creating a pair excitation, and therefore a "Gaudino state", as can be easily verified in the BCS limit.

In the BCS limit $d \ll \Delta_{\mathrm{BCS}}$ (i.e. at $\lambda \gg 1/\ln N$, where N is the number of energy levels between the Fermi energy and ω_{co}), the result follows from

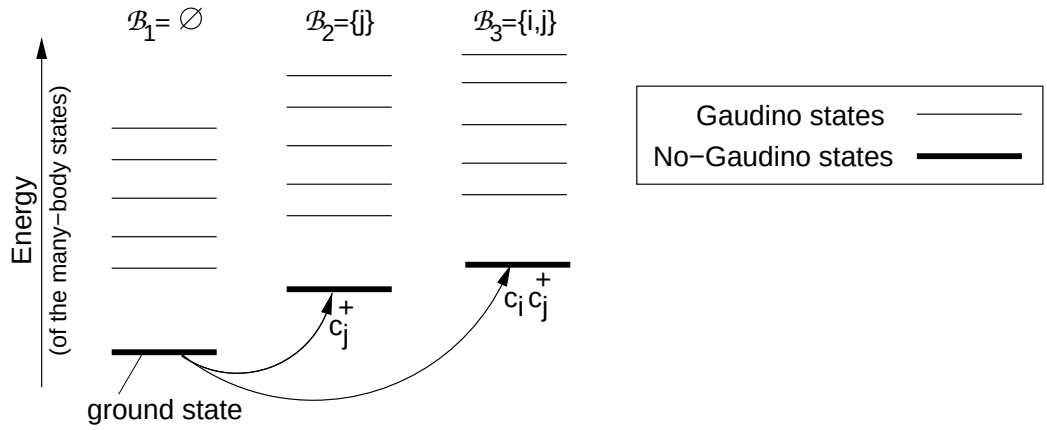

Figure 4.1: Illustration of the Hilbert space structure for the pairing Hamiltonian H^p of Eq. (4.1): The horizontal lines represent the many-body eigenstates of $H^0 + H^p$, ordered vertically along an energy axis and grouped according to their respective Hilbert space sector, which is defined by the set of singly occupied single-particle energy levels $\mathcal{B}$. Three sectors are shown, namely the ones given by $\mathcal{B}_1 = \emptyset$ (no singly occupied level), by $\mathcal{B}_2 = \{j\}$ (one singly occupied level j), and by $\mathcal{B}_3 = \{i, j\}$ (two singly occupied levels i, j). The lowest energy state in each of the sectors is the "No-Gaudino state" (thick lines). I also illustrate that the operators $c_j^\dagger$ and $c_i c_j^\dagger$ (with mutually different indices $i \neq j$) produce to an excellent approximation the No-Gaudino states in the respective sectors when acting on the ground state.

the relation

$$\hat{O}|gs\rangle \approx v_{i_1}\cdots v_{i_k}u_{j_1}\cdots u_{j_l}|i_1^{-\sigma_1}\cdots j_l^{\sigma_l'}\rangle^0, \tag{4.6}$$

where the state $|i_1^{-\sigma_1}\cdots j_l^{\sigma_l'}\rangle^0$ is the BCS limit of a No-Gaudino state of the form of Eq. (4.4). Here, u, v are the coherence factors from BCS theory [Tin96].

In the opposite limit $\Delta_{\mathrm{BCS}} \ll d$ ($\lambda \ll 1/\ln N$), where perturbation theory in λ is valid [SILvD01], the ground state is given by

$$|\mathrm{gs}\rangle = \left(1 + \lambda \sum_{i>\mu, j<\mu} \frac{c_{i\uparrow}^\dagger c_{i\downarrow}^\dagger c_{j\downarrow} c_{j\uparrow}}{\epsilon_i - \epsilon_j}\right)|\mathrm{Fermi}\rangle + O(\lambda^2), \tag{4.7}$$

and No-Gaudino excited states by $\hat{O}|\mathrm{gs}\rangle + O(\lambda^2)$, where $|\mathrm{Fermi}\rangle$ is the Fermi state, and $\hat{O}$ satisfies the "central condition" introduced after Eq. (4.5). Therefore, the same conclusion as in the BCS limit is obtained to first order in λ (i.e. up to errors of order λ^2): $\hat{O}|\mathrm{gs}\rangle$ again creates precisely the No-Gaudino state.

There is no such simple analytic argument that the Gaudino admixture to $\hat{O}|\mathrm{gs}\rangle$ will be negligible also in the intermediate regime, where neither BCS nor perturbation theory is applicable. However, this assertion can be checked numerically by a sum rule, which follows from Eq. (4.2):

$$\int \mathcal{A}(\omega)d\omega = \sum_{|I\rangle} \langle gs|\hat{O}^\dagger|I\rangle\langle I|\hat{O}|gs\rangle = \langle gs|\hat{O}^\dagger\hat{O}|gs\rangle. \tag{4.8}$$

The right hand side is a simple ground state expectation value and is therefore easily evaluated using the DMRG. I define the lost spectral weight $w_{\mathrm{L}} \equiv \langle gs|\hat{O}^\dagger\hat{O}|gs\rangle - |\langle gs|\hat{O}^\dagger|I\rangle^0|^2$ as the part of Eq. (4.8) that is not carried by the No-Gaudino state $|I\rangle^0$, but instead lost to other background states. As is shown in Fig. 4.2 below, this lost weight turns out to be negligibly small.

Creating a linear superposition $\hat{O} = \alpha_1\hat{O}_1 + \cdots + \alpha_N\hat{O}_N$ of operators of the form of Eq. (4.5) poses no particular difficulties: This sum leads to a sum of spectral functions as in Eq. (4.2) Under the condition that all operators $\hat{O}_n$, $n = 1..N$, are different, and that each $\hat{O}_n$ contains each energy level at most once, each operator takes the ground state into a sector of the Hilbert space whose quantum numbers are *different* from the other operators. Therefore, the intermediate states $|I\rangle_n$ that contribute to a given operator $\hat{O}_n$ are orthogonal to the others, $|I\rangle_{n'\neq n}$. Consequently, the spectral function Eq. (4.2) is just given by a sum of spectral functions for each $\hat{O}_n$ without interference terms:

$$\mathcal{A}_{\hat{O}}(\omega) = |\alpha_1|^2\mathcal{A}_{\hat{O}_1}(\omega) + \cdots + |\alpha_N|^2\mathcal{A}_{\hat{O_N}}(\omega). \tag{4.9}$$

Therefore, it is sufficient to consider operators of the form of Eq. (4.5).

4.3 DMRG implementation of the No-Gaudino Approximation

I now give a brief description of the DMRG algorithm as applied to calculating spectral functions within the universal Hamiltonian. The general algorithm is as described in section 3.3: Energy levels are added one by one to the system until it obtains its final size. For simplicity, I assume the energy levels to be equally spaced, although none of the methods presented here require this assumption. After adding a level, only a limited number m of basis vectors are kept, such that the size of the Hilbert space remains numerically manageable. These basis vectors are selected in order to represent a number of so-called target states accurately; this is achieved by the DMRG projection described in [WN99]. By varying m between 60 and 140, I estimate the relative error in the spectral function from the DMRG projection to be of the order of $\sim 10^{-5}$ (for $m = 60$). This accuracy is sufficient for the present purpose; it can be improved by increasing m.

In order to calculate the spectral function corresponding to the operator $\hat{O}$ in Eq. (4.5), I use as target states the ground state and a state representing the No-Gaudino state $|i_1^{-\sigma_1};\cdots;j_l^{\sigma_l'}\rangle^0$, with levels $i_1,\cdots,j_l$ singly occupied, in the BCS limit given by Eq. (4.4).

In fact, rather than using the No-Gaudino state itself, the state

$$|i_1\cdots j_l\rangle^0 \equiv \hat{O}^\dagger |i_1^{-\sigma_1}\cdots j_l^{\sigma_l'}\rangle^0, \tag{4.10}$$

is targeted, with $\hat{O}$ given by Eq. (4.5). In Eq. (4.10), the levels $i_1,...,j_l$ do, again, not participate in pair scattering, but levels $i_1,...,i_k$ are now doubly occupied, and levels $j_1,...,j_l$ are empty. This state is obtained by calculating the ground state of a modified Hamiltonian, namely Eq. (4.1) with all pair scattering involving the levels i,j removed. The levels i (j) are arranged to be occupied (empty) by assigning them a positive (negative) kinetic energy term $\Delta\epsilon_i$ ($\Delta\epsilon_j$) of the order $-\omega_{\rm co}$ ($+\omega_{\rm co}$). The main advantage of this choice of the target state is that no singly occupied levels occur at any point in the algorithm, hence only doubly occupied or empty levels have to be considered. Furthermore, it allows to express the matrix element occurring in the spectral function (4.2) as a simple scalar product:

$$|^0\langle i_1^{-\sigma_1}\cdots j_l^{\sigma_l'}|\hat{O}|gs\rangle|^2 = |^0\langle i_1\cdots j_l|gs\rangle|^2. \tag{4.11}$$

In order to obtain the excitation energy of the state $|i_1^{-\sigma_1}\cdots j_l^{\sigma_l}\rangle^0$, the kinetic energy of the singly occupied levels $i_1\cdots j_l$ must of course be properly accounted for: The nonphysical kinetic energy terms $2(\epsilon_i+\Delta\epsilon_i)$ of the doubly

occupied energy levels in Eq. (4.10) must be removed, and the energies ϵ_i, ϵ_j of the singly occupied levels must be added. In this way, all the ingredients for the evaluation of the No-Gaudino contribution to Eq. (4.2) are provided by the DMRG.

The sum rule, i.e. the right hand side of Eq. (4.8), is evaluated in a separate run with $|\mathrm{gs}\rangle$ and $\hat{O}^\dagger|\mathrm{gs}\rangle$ as the target states.

As is seen e.g. in Fig. 4.5 below, the DMRG results for the spectral function reproduce the BCS result, valid for $d \ll \Delta_{\mathrm{BCS}}$, and the result from first order perturbation theory in the interaction, valid for $d \gg \Delta_{\mathrm{BCS}}$, in the respective limits, but the DMRG is accurate in the entire crossover regime as well.

4.4 Dominance of a single No-Gaudino state

The fact that the spectral function is dominated by one single No-Gaudino state is displayed in Fig. 4.2. Here, the expectation value $\langle \mathrm{gs}|c_{i\sigma}c_{i\sigma}^\dagger|\mathrm{gs}\rangle$, which occurs in the sum rule, Eq. (4.8), with $\hat{O} = c_i^\dagger$, is plotted (for $i = 10$, i.e. 10 levels above E_{Fermi}) against the coupling λ. It is practically indistinguishable from the contribution $|{}^0\langle I|c_{i\sigma}^\dagger|\mathrm{gs}\rangle|^2$ from the No-Gaudino state only.

The lost weight w_{L}, shown in the inset of Fig. 4.2, is seen to be less than 0.2% of the total spectral weight throughout the entire parameter regime. The data is again shown for $i = 10$; the plots for other values of i, not shown, look similar. The maximum lost weight somewhat increases as the level i approaches E_{Fermi}, but always remains below 1% of the total weight.

The lost weight is seen to be vanishingly small for small λ, as expected in the perturbative regime $\lambda \ll 1/\ln N$. Interestingly, the lost weight also decreases for *large* λ. This is very untypical for interacting systems, and the underlying reason is that the dominance of the No-Gaudino state is protected also in the BCS regime as shown in Eq. (4.6), which is valid for $\lambda \gg 1/\ln N$. Consequently, the lost weight shown in the inset of Fig. 4.2 displays a maximum in the intermediate regime around $\lambda \sim 1/\ln N$, indicated by the dotted line, in which neither bulk BCS theory nor perturbation theory in λ are reliable. This peak is a universal feature for all values of i (not shown).

In Fig. 4.3, the position $\lambda_{\max}(N)$ and the value $w_{L,\max}(N)$ of this maximum is shown for the tunneling density of states, i.e. the sum of the above spectral function over all levels i (see section 4.5 below). As expected, $\lambda_{\max}(N)$ lies in the shaded crossover region around $\lambda_{\max}(N) \sim 1/\ln N$. The maximum value $w_{L,\max}(N)$ turns out to be a monotonically decreasing function of N, i.e. the lost weight vanishes *for all couplings* as the continuum limit is approached.

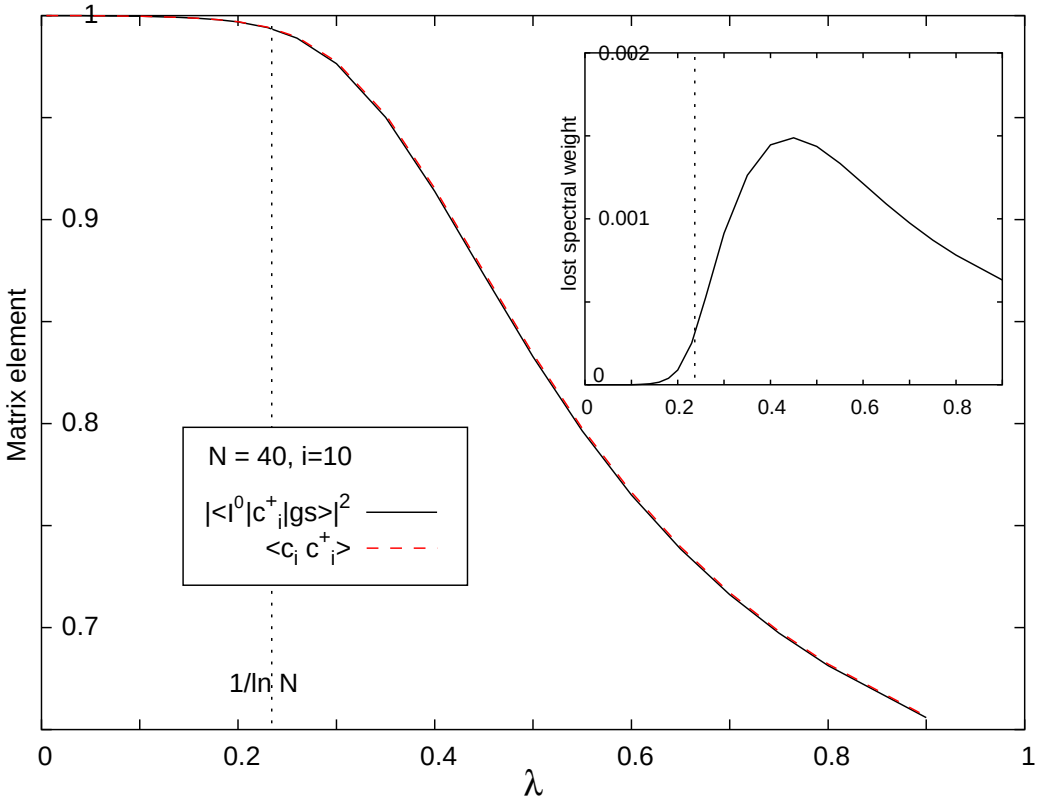

Figure 4.2: The matrix element $\langle c_{i\sigma} c_{i\sigma}^\dagger \rangle$ from Eq. (4.8) with $\hat{O} = c_{i\sigma}^\dagger$ (dashed line) and the contribution from the No-Gaudino state (solid line) as a function of λ. Here, $i = 10$, i.e. the tenth out of a total of $N = 40$ energy levels above E_{Fermi}. The lost weight w_{L}, i.e. the difference between both, is plotted in the inset. It shows a maximum in the intermediate regime around $\lambda \sim 1/\ln N$ (indicated by the dotted line), but even there, w_{L} is less than 0.2% of the total spectral weight.

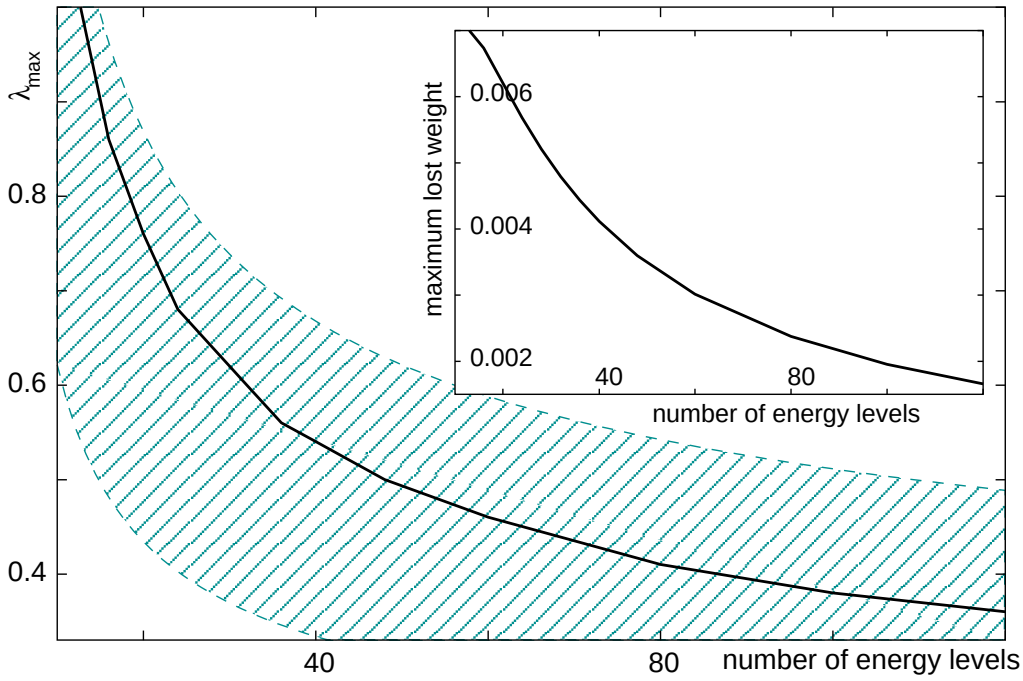

Figure 4.3: Position of the maximum of the lost weight w_{L} in the plane spanned by the coupling constant λ and the number of energy levels. This position lies in the crossover region $\lambda \sim 1/\ln N$ (namely in the shaded region $1/\ln N < \lambda < 2/\ln N$), where N is the number of energy levels. Inset: Value of the lost weight along the maximum curve, as a function of the number of energy levels.

4.5 Applications

The dominance of the No-Gaudino state in the spectral function is not only remarkable by itself, but has also high practical value: it allows to calculate the spectral function with high precision using the DMRG in what I call the "No-Gaudino approximation", in which only the No-Gaudino state is kept in Eq. (4.2). From the spectral function, in turn, many important physical quantities can be obtained. The lost weight w_{L}, defined after Eq. (4.8), controls the quality of this approximation: when w_{L} vanishes, the No-Gaudino approximation is exact.

4.5.1 Tunneling density of states

As a first application, I calculate the tunneling density of states $\nu(\omega) = \sum_{i\sigma} \mathcal{A}_{c_{i\sigma}^\dagger}(\omega)$ (for $\omega > 0$). Fig. 4.4 illustrates that during the crossover from the few-electron ($d \gg \Delta_{\mathrm{BCS}}$) to the bulk limit ($d \ll \Delta_{\mathrm{BCS}}$), the familiar BCS gap of width Δ_{BCS} emerges together with a strongly pronounced peak at $\omega \approx \Delta_{\mathrm{BCS}}$ as the quasiparticle energies are kept away from the Fermi surface by the pairing interaction and accumulate at Δ_{BCS}. In the BCS limit, the familiar expression (shown in dashed lines)

$$\nu_{\mathrm{tunn}}(\omega) = v(\omega)^2 \nu(\omega), \tag{4.12}$$

is recovered, where

$$v(\omega)^2 = \frac{1}{2}\left(1 + \frac{\omega^2}{\omega^2 + \Delta_{\mathrm{BCS}}^2}\right), \tag{4.13}$$

$$\nu(\omega) = \begin{cases} \frac{\omega}{\sqrt{\omega^2 - \Delta_{\mathrm{BCS}}^2}} & \text{if } \omega > \Delta_{\mathrm{BCS}}, \\ 0 & \text{otherwise.} \end{cases} \tag{4.14}$$

As shown in Fig. 4.2 and 4.3, the lost weight again shows a maximum at $\lambda \sim 1/\ln N$, but is found to never exceed fractions of 1%, thus confirming the accuracy of the No-Gaudino approximation.

4.5.2 Magnetic response of rings

As a second example of a quantity that is well captured by the No-Gaudino approximation, I calculate the prediction of the pairing Hamiltonian for the magnetic response ΔE_2 of small metallic rings, [1] i.e. the derivative of the

[1] For the purposes of this thesis, the calculation of the persistent current using the BCS model should be regarded as a "toy calculation", whose sole purpose is to illustrate the

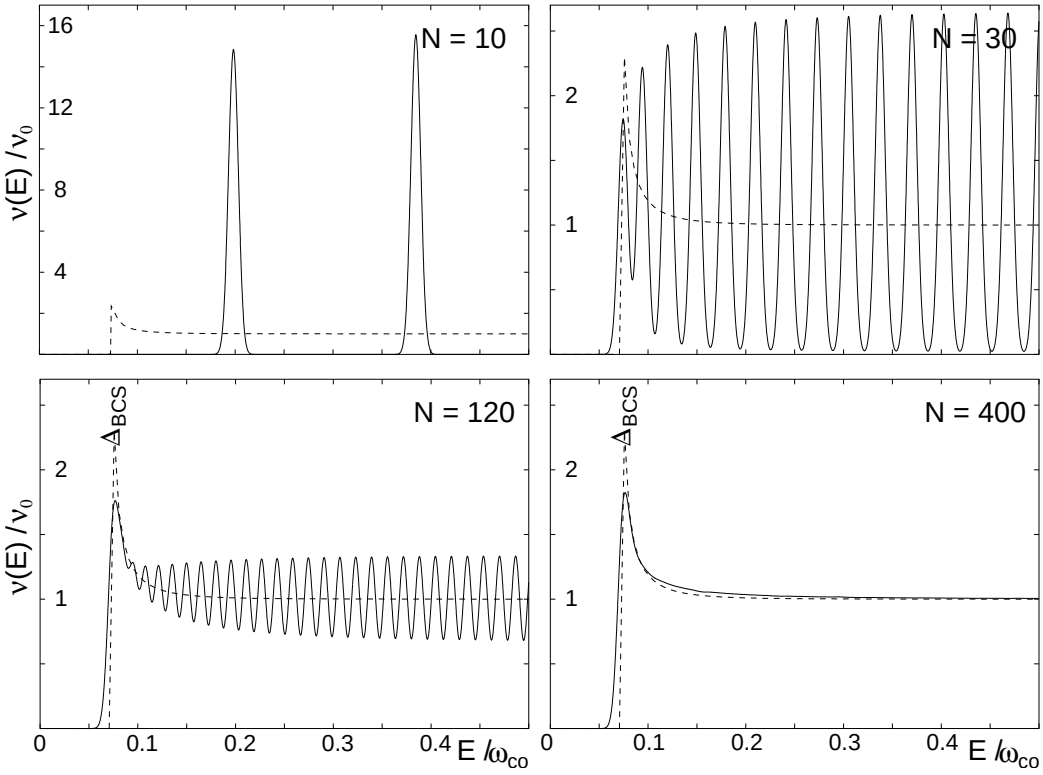

Figure 4.4: The tunneling density of states $\nu(E)$ for $\Delta_{\rm BCS} = 0.07\omega_{\rm co}$ and $N = 5, 30, 60, 200$ energy levels above $E_{\rm Fermi}$, in the No-Gaudino approximation (solid line; for the sake of better visibility, the delta peaks in Eq. (4.2) have been replaced by Gaussians of width $0.005\omega_{\rm co}$). The familiar gap $\Delta_{\rm BCS}$ emerges during the crossover from the few-electron ($d \gg \Delta_{\rm BCS}$) to the bulk limit ($d \ll \Delta_{\rm BCS}$). In the latter limit, one observes agreement with the BCS result (dashed line).

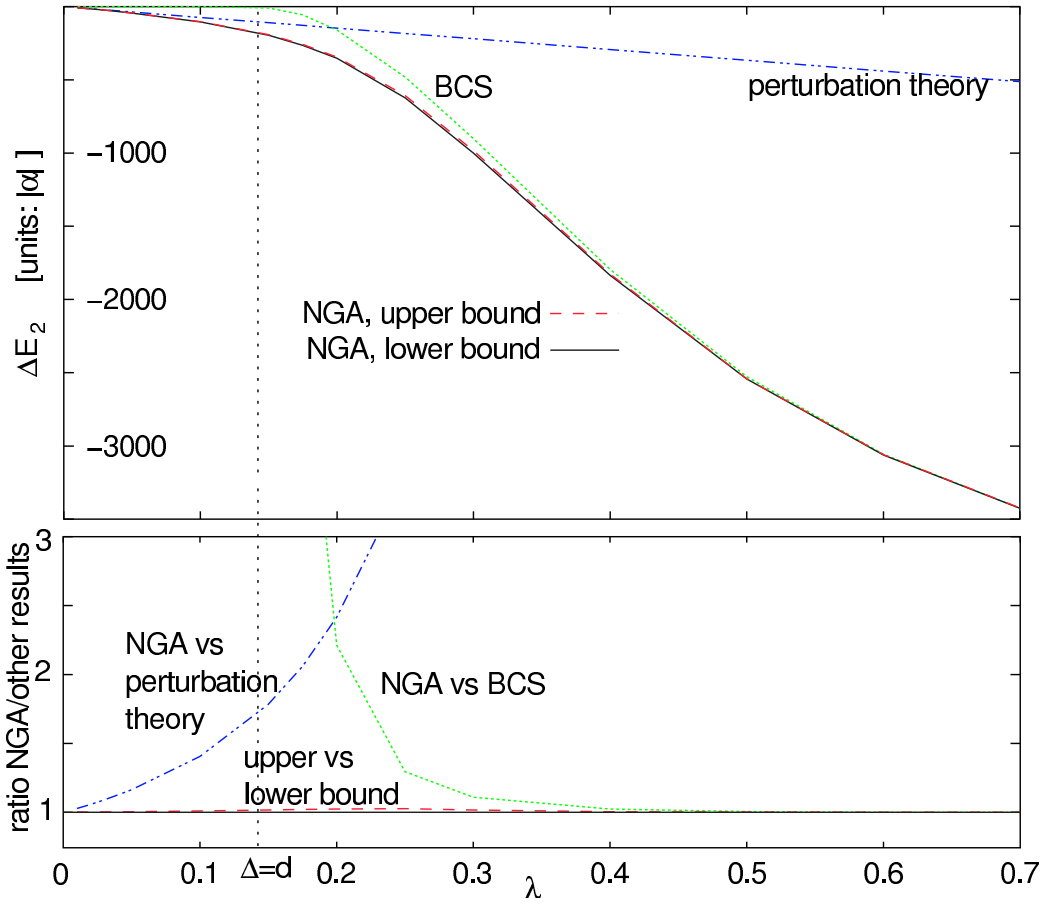

Figure 4.5: Upper part: The magnetic response ΔE_2 from Eq. (4.15) as function of λ for $N = 40$ energy levels above E_{Fermi}. The upper and lower bound from the No-Gaudino approximation (solid and dashed line) practically coincide and interpolate between the perturbative and the BCS results (dashed-dotted and dotted line), valid for small and large λ, respectively. Lower part: The ratio between the No-Gaudino approximation and the other results. In the regime $\lambda \sim 1/\ln N$, the perturbative and the BCS results underestimate the true result (which must lie between the upper and lower bound) by a factor of more than 2.

persistent current with respect to flux at zero flux. For $\lambda \ll 1/\ln N$, ΔE_2 was calculated in perturbation theory, for $\lambda \gg 1/\ln N$ the BCS approximation was used [SILO03]. Here, using the No-Gaudino approximation, I calculate ΔE_2 for all values of $\lambda > 0$, and specifically in the crossover regime between the perturbative and the BCS regimes.

The linear response to the magnetic flux through a ring is given by $\Delta E_2 = E_2^{\rm par} - E_2^{\rm dia}$, where

$$E_2^{\rm par} = -2\left(\frac{e}{m_e L}\right)^2 \sum_{mn,|I\rangle} |P_{mn}|^2 \frac{|\langle I|c^\dagger_{m\uparrow}c_{n\uparrow} - c^\dagger_{n\downarrow}c_{m\downarrow}|gs\rangle|^2}{E_I}. \qquad (4.15)$$

and $E_2^{\rm dia}$ equals the $\lambda = 0$ value of $E_2^{\rm par}$ [SILO03]. Here, m_e,e are the electron mass and charge, L is the circumference of the ring. P_{mn} is the momentum operator between the disordered 1-particle states, labelled by m and n. In the highly diffusive regime ($\omega_{\rm co} < 1/\tau$, where τ is the elastic mean free time), which I assume here for simplicity, $|P_{mn}|^2 \equiv P^2$ can be taken to be constant for $m \neq n$, and zero otherwise [SOIL03]. $E_2^{\rm par}$ can then be extracted from the spectral functions for $\hat{O}_{mn\sigma} = c^\dagger_{m\sigma}c_{n\sigma}$.

In the No-Gaudino approximation, only the states $|i = m, n; j = n, m\rangle^0$ defined in Eq. (4.10) are retained in Eq. (4.15). Because the contribution of the other states, which are neglected, is always positive, the No-Gaudino approximation produces a lower bound for E_2. An upper bound can be found as well, namely by replacing the energy denominator of Eq. (4.15) by the energy $E^0_{mn}$of the No-Gaudino state, which is known to be smaller than the energy of any other contributing state. Then, the sum over $|I\rangle$ can be eliminated, and the resulting expression for the upper bound is

$$E_2^{>} = \alpha \sum_{m\neq n} \frac{\langle gs|(c^\dagger_{n\uparrow}c_{m\uparrow} - c^\dagger_{m\downarrow}c_{n\downarrow})(c^\dagger_{m\uparrow}c_{n\uparrow} - c^\dagger_{n\downarrow}c_{m\downarrow})|gs\rangle}{E^0_{mn}}. \qquad (4.16)$$

The results of my calculation are presented in Fig. 4.5, where the upper and lower bound is compared to the perturbative and to the BCS result, given in [SILO03]. The lower and upper bounds practically coincide (with an error of $< 0.5\%$) in the entire parameter regime; this reflects the high accuracy of the No-Gaudino approximation. As expected, the perturbative result is reproduced for small λ ($\Delta_{\rm BCS} \ll d$), the BCS result for large λ ($\Delta_{\rm BCS} \gg d$). However, both results underestimate the exact result by a factor of up to 2.5

merits of the No-Gaudino approximation within the BCS model. Whether this model can be expected to give a realistic description of real, quasi one-dimensional wires or not (a matter of some controversy [SOIL03; ESA04]) is irrelevant here.

in a large intermediate regime (Fig. 4.5 bottom). Interestingly, the magnetic response is found to be much larger than the BCS value also in a regime in which $\Delta \gg d$, where the BCS approximation is expected to be valid. This is due to a large contribution of the distant levels from Δ_{BCS} up to the interaction cutoff, which the BCS approximation neglects. A similarly large contribution from distant levels has previously been found also for the condensation energy [SILvD01] and single particle properties [SvDIL03].

Chapter 5

Real-time dynamics in spin-1/2 chains with adaptive time-dependent DMRG

5.1 Introduction

The transport properties of spin chains have attracted much attention recently, not only due to the possible applications to information storage, spintronics, and quantum information processing, but also because they allow to study general aspects of nonequilibrium dynamics in a comparably simple system. Nonequilibrium phenomena are a vast and despite all progress still poorly understood field of statistical physics. It is therefore useful to have a simple model at hand that allows to study general questions rather explicitly. In order to study nonequilibrium phenomena, a real-time description is particularly intuitive and useful. In this chapter, I study the time-evolution of a spin-1/2 chain by solving the full many-body Schrödinger equation.

Recently, new developments in the area of non-equilibrium physics were stimulated by the experimental progress in the field of ultracold atoms. These systems have the advantage that their parameters can be tuned in time with high accuracy and on very short time-scales. It was proposed that spin-1/2 chains can be realized in these systems as well [KS03; DDL03; AHDL03; MGW$^+$03], namely as a mixture of atoms of two species, say A and B. If these atoms are studied in an optical lattice with an average filling of one atom per site and with a very strong repulsive interaction between the atoms, such that multiple occupancy is suppressed, the system can be mapped onto an effective spin-1/2 model. In this effective model the state with atom A occupying a given lattice site corresponds to, say, $\uparrow$, and likewise B to $\downarrow$.

In this chapter, I study the time evolution of an initial state $|\uparrow \ldots \uparrow \downarrow \ldots \downarrow\rangle$ (or $|A \cdots AB \cdots B\rangle$), i.e. with all spins on the left half pointing up along the z axis, and all spins on the right half pointing down, under the effect of a nearest-neighbour spin interaction (see Eq. (5.1)). This system can also be interpreted as an oversimplified picture for spin transport between two coupled reservoirs of completely polarized spins of opposite direction in the two reservoirs. I address the following questions: Does the state evolve into a simple long time limit? If so, how is this limit reached? On what properties does the long time behaviour depend?

Analytical results for this problem are essentially restricted to the XX-chain, which is amenable to an exact solution [ARRS99]. Here, a scaling relation for the long-time limit was found. However, it is presently not known whether this relation is general, or whether it relies on special properties of the XX model. If a long-time limit exists for other models as well, the question arises which of its characteristics are universal, and which depend on certain system properties.

Directly solving the time-dependent Schrödinger equation for interacting many-body systems is highly nontrivial. A recently developed numerical method, the adaptive time-dependent DMRG [Vid04; DKSV04; WF04] (adaptive t-DMRG), enables me to perform this task. The two main conditions for this method to be applicable, namely that the system must be one-dimensional and have nearest-neighbour interactions only, are met for the present model. Efforts to generalize the DMRG method to time-depending problems relaxing these constraints are under way [WF].

As so far no detailed error analysis of this new method has been performed, an important aspect of the present work is that besides their own physical interest, spin-1/2 chains provide an excellent benchmark for the adaptive time-dependent DMRG, because of the nontrivial exact solution for the XX model, against which the method can be compared. This allows me to analyze the accuracy of the adaptive time-dependent DMRG very explicitly, namely to address the questions what kinds of errors can occur in principle, which ones of these dominate in practice, and how they can be minimized.

The outline of this chapter is as follows: In section 5.2, I introduce the model and its characteristics. In section 5.3, I summarize the method, and perform a detailed error analysis in section 5.4. These two sections may be skipped by readers mainly interested in the physics and not in the details of the method. In section 5.5, I present the results for the long time limit of the time evolution for different interaction and dimerization strength.

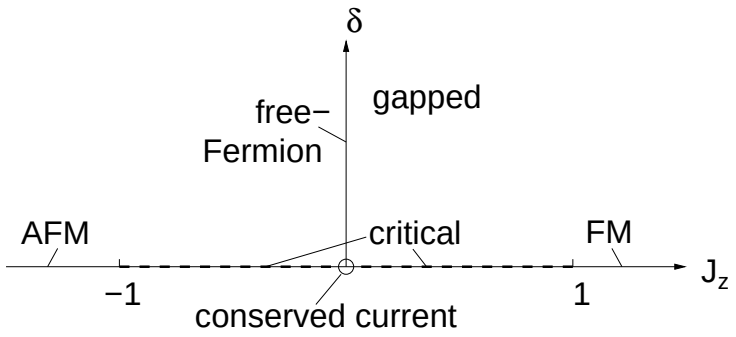

Figure 5.1: Quantum phase diagram of the Heisenberg model, Eq. (5.1). See [MK04; Sch94] for details.

5.2 Model and initial state

In this chapter I analyze the dynamics of the inhomogeneous initial state $|\text{ini}\rangle = |\uparrow \ldots \uparrow\downarrow \ldots \downarrow\rangle$ on the one-dimensional spin-1/2 chains with interactions given by the Heisenberg model

$$H = \sum_n J_n (S_n^x S_{n+1}^x + S_n^y S_{n+1}^y + J_z S_n^z S_{n+1}^z) \equiv \sum_n h_n. \tag{5.1}$$

Here, $\vec{S}_n$ is the spin operator on site n, and J_n, J_z are interaction constants. I consider dimerized models where $J^z = const$ and $J_n = (1 + (-1)^n \delta)$, δ being the dimerization coefficient. For $\delta > 0$, the "strong bond" with $J_n = 1 + \delta$ is chosen to be at the center, where the spin flip of the initial state is located.

I have chosen the energy unit such that $J_n = 1$ for the homogeneous case $\delta = 0$. I also set $\hbar = 1$, defining time to be 1/energy with the energy unit chosen as just mentioned.

The quantum phase diagram of this model at zero temperature is well known (see [MK04; Sch94]) and sketched in Fig. 5.1. For the homogeneous case, $\delta = 0$, the ground state has ferromagnetic (FM) / antiferromagnetic (AFM) order with a gap in the excitation spectrum for $J_z < -1$ and $J_z > 1$, respectively. The gap closes if $|J_z|$ approaches 1 from above, and the model becomes critical for $-1 < J_z < 1$, i.e. gapless in the thermodynamic limit, with correlation functions showing a power-law decay. The model at the point $J_z = \delta = 0$ is known as the XX model. It has the special property that the spin-current operator $J = \sum_n j_n$ is conserved, i.e. $[J, H] = 0$. Here $j_n = J_n \text{Im}\,(S_n^+ S_{n+1}^-)$ is the current operator on the bond between site n and $n + 1$. For finite dimerization, $\delta \neq 0$, the spectrum is again gapped for all values of J_z.

Often it is useful to map the Heisenberg model onto a model of spinless fermions:

$$\begin{aligned} H &= \sum_n J_n \left[\frac{1}{2}(c_n^\dagger c_{n+1} + c_{n+1}^\dagger c_n) \right. \\ &\quad \left. + J_z (c_n^\dagger c_n - \frac{1}{2})(c_{n+1}^\dagger c_{n+1} - \frac{1}{2}) \right]. \end{aligned} \tag{5.2}$$

In this picture, the first two terms in Eq. (5.1) describe nearest-neighbour hopping, whereas the third term (the one proportional to J_z) describes a density-density interaction between nearest neighbours. In particular, the case $J_z = 0$ describes free fermions on a lattice, and can be solved exactly [LSM61].

The time-evolution under the influence of a time-independent Hamiltonian H as in Eq. (5.1) is given by:

$$|\psi(t)\rangle = U(t)|\mathrm{ini}\rangle \quad \text{with } U(t) = \exp(-iHt). \tag{5.3}$$

In most of the phases shown in Fig. 5.1, the state $|\mathrm{ini}\rangle = |\uparrow \ldots \uparrow\downarrow \ldots \downarrow\rangle$ contains many high-energy excitations and is thus far from equilibrium. In the following, I briefly discuss these phases separately.

- Deep in the ferromagnetic phase, $J_z < -1$, $|\mathrm{ini}\rangle$ corresponds to a state with one domain wall between the two degenerate ground states. For $J_z \to -\infty$ it is identical to the ground state (with boundary conditions given by $|\uparrow\rangle$ and $|\downarrow\rangle$ and $S_z^{\mathrm{tot}} = 0$), and therefore stationary. For finite J_z, it is no longer identical to the ground state, but still close to it [MMR91].

- In the antiferromagnetic phase, $J_z > 1$, the state $|\mathrm{ini}\rangle$ is highly excited. One could view it as a state with almost the maximum number of domain walls of staggered magnetization.

  In this context, it is interesting to note that the sign of J_z does not matter for the time evolution of physical quantities, as long as the initial state is described by a purely real wave function (which is the case for my choice of $|\mathrm{ini}\rangle$), since the sign change in J_z can be compensated by a gauge transformation that inverts the sign of the hopping terms $S^x S^x$, $S^y S^y$ in Eq. (5.1), plus a complex conjugation of Eq. (5.3). In particular, the time-evolution of the low-energy one domain-wall state in the FM is the same as the evolution of the high-energy many domain-walls state in the AFM. I therefore restrict the analysis to the case $J_z > 0$.

- In the critical phase $\delta = 0$ and $|J_z| < 1$, the ground state is a state with power-law correlations in the xy-plane. Here, the state $|\text{ini}\rangle$ is not close to any particular eigenstate of the system, but contains many excited states throughout the energy spectrum, depending on the value of J_z: The energy expectation value of $|\text{ini}\rangle$ is low as $J^z \to -1$ and high as $J^z \to 1$.

  The time evolution delocalizes the domain wall over the entire chain. For $J_z = 0$, the time-evolution of the system can be solved exactly. For example, the magnetization profile for the initial state $|\text{ini}\rangle$ reads [ARRS99]:

$$S_z(n,t) = \langle\psi(t)|S_n^z|\psi(t)\rangle = -1/2 \sum_{j=1-n}^{n-1} J_j^2(t), \tag{5.4}$$

  where J_j is the Bessel function of the first kind. $n = \ldots -2, -1, 0, 1, 2 \ldots$ labels chain sites with the convention that the first site in the right half of the chain has label $n = 1$.

- In the dimerized phase, $\delta \neq 0$, the mentioned characteristics remain unchanged. However, here the delocalization becomes confined to pairs of neighbouring sites in the limit $\delta \to 1$.

I finally note that the total energy and magnetization of the system are conserved at all times, such that even for long times the state cannot relax to the ground state.

5.3 Outline of the adaptive time-dependent DMRG for spin chains

In order to determine the time-evolution Eq. (5.3), I use the adaptive t-DMRG method [DKSV04; WF04], which has been introduced as an extension of standard DMRG from chapter 2 using the TEBD algorithm of Vidal [Vid04]. It allows to evaluate the time-evolution for one-dimensional quantum chains with nearest-neighbour (possibly time-dependent) interactions. In this chapter, I consider the case of a time-independent Hamiltonian where the dynamics is introduced by a nonequilibrium initial state at $t = 0$. To set the stage for the error analysis, I review in this section the adaptive t-DMRG algorithm.

I begin by recapitulating some aspects of the standard finite-system DMRG (which was presented in chapter 2) that are of particular importance here. In

the DMRG, a quantum-mechanical state on a one-dimensional chain with L sites is represented in a particular tensor product basis as in Eq. (2.1) (with $L = l$), see the illustration in the upper part of Fig. 2.2 (with $L = l_f$). Here, $|\sigma\rangle_n$, $|\tau\rangle_{n+1}$ are complete bases on sites n, $n+1$; $|\alpha\rangle_{1..n-1}$ and $|\beta\rangle_{n+2..L}$ are states on the subchains with sites $1, ..., n-1$ and $n+2, ..., L$, respectively. The states $|\alpha\rangle_{1..n-1}$ and $|\beta\rangle_{n+2..L}$ form truncated bases, i.e. they do not span the full Hilbert space on their respective subchains, but only a subspace of dimension m, chosen to allow an optimal approximation of the true physical state. In the representation of Eq. (2.1), I call site n the "active site". The algorithm now consists in its essence of moving ("sweeping") the position of the active site several times from the left to the right end of the chain and back, and constructing optimized truncated bases for the subchains.

A DMRG step during such a sweep, say, to the right now involves a basis transformation from the old (truncated) basis $|\alpha\rangle_{1..n-1}|\sigma\rangle_n|\tau\rangle_{n+1}|\beta\rangle_{n+2..L}$ with active site n to a new one $|\alpha'\rangle_{1..n}|\sigma'\rangle_{n+1}|\tau'\rangle_{n+2}|\beta'\rangle_{n+3..L}$ with active site $n+1$ as shown in Fig. 2.2. The states $|\alpha'\rangle_{1..n}$ representing the sites $1, ..., n$ are linear combinations of the old basis vectors $|\alpha\rangle_{1..n-1}|\sigma\rangle_n$. Not all linear combinations are kept because of the DMRG truncation that limits the number of states $|\alpha'\rangle_{1..n}$ to m states. For this reason, the state $|\psi\rangle$ can in general be represented in the new basis only up to some truncation error. The DMRG truncation algorithm described in chapter 2 provides a unique optimal choice for the states $|\alpha'\rangle$ that minimizes this error (which is then typically as low as 10^{-10} or so) and thus allows for the optimal representation of particular target states. The basis vectors $|\beta'\rangle_{n+3..L}$ are taken from stored values from the previous sweep to the left. – A sweep to the left (i.e. from active site n to $n-1$) works in the same way, with the role of $|\alpha'\rangle$ and $|\beta'\rangle$ interchanged.

In standard DMRG, a mere transformation of the state $|\psi\rangle$ from one basis to the other – known as White's state prediction [Whi96] – is possible and accurate up to the (small) truncation error. However, in order to optimize the basis states iteratively for representing the target state(s) $|\psi\rangle$, new information must be provided about $|\psi\rangle$, i.e. it must be newly constructed using some unique criterion (typically as the ground state of some Hamiltonian). Without such a criterion to "sweep against", the accuracy cannot increase during sweeps, and the procedure would be pointless. Merely transforming $|\psi\rangle$ in this way is therefore of no use in standard DMRG, and is in fact never performed alone. It is, however, the basis of the adaptive t-DMRG.

The adaptive t-DMRG algorithm relies on the Trotter decomposition of the time evolution operator $U(t)$ of Eq. (5.3), which is defined as follows: Using the relation $U(t) = U(dt = t/M)^M$, the time evolution operator is decomposed into M time steps, where M is a large number such that the time interval $dt = t/M$ is small compared to the physical time scales of the

model. Since the Hamilton operator of Eq. (5.1) can be decomposed into a sum of local terms h_n that live only on sites n and $n+1$, $U(dt)$ can then be approximated by an n-th order Trotter decomposition [Suz76], e.g. to second order:

$$U(dt) = \prod_{\substack{n \\ \text{even}}} U_n(\frac{dt}{2}) \prod_{\substack{n \\ \text{odd}}} U_n(dt) \prod_{\substack{n \\ \text{even}}} U_n(\frac{dt}{2}) + O(dt^3). \tag{5.5}$$

The $U_n(dt)$ are the infinitesimal time-evolution operators $exp(-ih_n dt)$ on the bonds n (even or odd). The ordering *within* the even and odd products does not matter, because "even" and "odd" operators commute among themselves.

Eq. (5.5) allows to decompose the time-evolution operator $U(t)$ into many local operators U_n that live on sites n and $n+1$. The adaptive time-dependent DMRG now allows to apply the operators U_n successively to some state Ψ. Each operator U_n is applied exactly during sweeps in the DMRG step with n being the active site, i.e. where sites n and $n+1$ are represented without truncation (cf. Eq. (2.1)): This way, the basis states chosen to represent optimally the state before U_n is applied,

$$|\psi\rangle = \sum_{\alpha\sigma\tau\beta} \psi_{\alpha\sigma\tau\beta} |\alpha\rangle |\sigma\rangle_n |\tau\rangle_{n+1} |\beta\rangle \tag{5.6}$$

are equally well suited for representing the state

$$U_n|\psi\rangle = \sum_{\substack{\alpha\sigma\tau\beta \\ \sigma'\tau'}} (U_n)_{\sigma\tau,\sigma'\tau'} \psi_{\alpha\sigma'\tau'\beta} |\alpha\rangle |\sigma\rangle_n |\tau\rangle_{n+1} |\beta\rangle \tag{5.7}$$

without any additional error, because U_n only acts on the part of the Hilbert space (spanned by the vectors $|\sigma\rangle_n|\tau\rangle_{n+1}$) that is exactly represented.

To continue the sweep, a DMRG truncation is carried out with $U_n|\psi\rangle$ being the target state instead of $|\psi\rangle$. The key observation is that the new truncated basis is optimally adapted to $U_n|\psi\rangle$ and different from the one that would have been chosen for $|\psi\rangle$. In contrast to the conventional static DMRG [CM02], the optimally represented Hilbert space hence *follows the time-evolution of the state* $|\psi(t)\rangle$.

Then basis transformations to the left or right are performed, until the next part of Eq. (5.5) can be applied. Thus, the the full operator of Eq. (5.5) is applied by sweeping the active site n through the system. The price to be paid is that a truncation error is introduced at each iteration step of the sweep as is known from static DMRG.

To start time-dependent DMRG, some initial state has to be prepared. There is no unique recipe, the most effective one depending on the desired initial state. The procedure I adopt for the initial state $|\text{ini}\rangle$ is to calculate

it as the ground state of a suitably chosen Hamiltonian H_{ini} (which does in principle not have to have any physical significance). Such a choice is $H_{\text{ini}} = \sum_n B_n S_n^z$, with $B_n < 0$ for n on the left, $B_n > 0$ for n on the right half of the chain. In this case, a physical picture for H_{ini} does exist; it corresponds to switching on a magnetic field that aligns the spins and that is strong enough for all interactions in Eq. (5.1) to be negligible.

5.4 Accuracy of the adaptive time-dependent DMRG

As so far no quantitative analysis of the accuracy of the adaptive t-DMRG has been given in the literature, I provide a detailed error analysis for the time evolution of the initial state $|\text{ini}\rangle$ in a spin-1/2 quantum XX chain, i.e. $J_z = \delta = 0$. This system is an excellent benchmark for the adaptive t-DMRG due to its exact solution [ARRS99] that can be compared to the DMRG results. The exact solution reveals a nontrivial behaviour with a complicated substructure in the magnetization profile. From a DMRG point of view this Hamiltonian is not too specific in the sense that the experience from static DMRG suggests a relatively weak truncation error dependence on J^z.

5.4.1 Possible errors

Two main sources of error occur in the adaptive t-DMRG:
(i) The *Trotter error* due to the Trotter decomposition. For a nth-order Trotter decomposition [Suz76], the error made in one time step dt is of order dt^{n+1}. To reach a given time t one has to perform t/dt time-steps, such that the error grows linearly in time t and the resulting error is of order $(dt)^n t$. In the Trotter decomposition used here, the error scales linearly with system size L, and overall it is of order $(dt)^n Lt$ for the times of interest. (Eventually, the error must saturate at a finite value, as measured quantities are typically bounded.) The linear L dependence of the error is expected for generic initial states. For the particular choice of $|\text{ini}\rangle$ of this chapter, however, many of the $O(L)$ contributions to the Trotter error vanish, as many of the sites exhibit no dynamics at all for short times. – For the calculations presented in this chapter, I have chosen $n = 2$, but my observations should be generic.
(ii) The DMRG *truncation error* due to the representation of the time-evolving quantum state in reduced (albeit "optimally" chosen) Hilbert spaces and to the repeated transformations between different truncated basis sets.

While the truncation error ϵ that sets the scale of the error of the wave function and operators is typically very small, here it will strongly accumulate as $O(Lt/dt)$ truncations are carried out up to time t. This is because the truncated DMRG wave function has norm less than one and is renormalized at each truncation by a factor of $(1-\epsilon)^{-1} > 1$. Truncation errors should therefore accumulate roughly exponentially with an exponent of $\epsilon Lt/dt$, such that eventually the adaptive t-DMRG will break down at too long times. The error measure used here saturates at $O(1)$ and sets a limit on the exponential growth; also, partial compensations of errors in observables can in principle slow down the error growth. The accumulated truncation error should decrease considerably with an increasing number of kept DMRG states m. For a fixed time t, it should furthermore decrease as the Trotter time step dt is increased, as the number of truncations decreases with the number of time steps t/dt.

At this point, it is worthwhile to mention that the subsequent error analysis should also be pertinent to the very closely related time-evolution algorithm introduced by Verstraete *et al.* [VGRC04], which is different in one major point: In the algorithm I use, a basis truncation is performed after each *local* application of U_n. In their algorithm truncations are performed after all local time-evolutions have been carried out, i.e. after a *global* time-evolution using $U = \prod_n U_n$. In my approach, the wave function after such a full time evolution is not guaranteed to be the *globally* optimal state representing the time-evolved state. However, for small dt the state update via the operators U_n is likely to be small, I expect the global optimum to be rather well approximated using the present algorithm, as seems to be borne out by direct comparisons between both approaches [Ver]. Errors should therefore exhibit very similar behaviour.

I remind that no error is encountered in the application of the local time evolution operator U_n to the state $|\psi\rangle$, as is discussed after Eq. (5.7).

5.4.2 Error analysis for the XX-model

In this section, I analyze the errors from the adaptive t-DMRG in the time evolution of the XX-model by comparing it to the exact solution [ARRS99], with the ultimate goal of finding optimal DMRG control parameters to minimize the errors.

I use two main measures for the error:
(i) As a measure for the overall error I consider the *magnetization deviation* the maximum deviation of the local magnetization found by DMRG from the

exact result,

$$\mathrm{err}(t) = \max_n |\langle S^z_{n,\mathrm{DMRG}}(t)\rangle - \langle S^z_{n,\mathrm{exact}}(t)\rangle|. \tag{5.8}$$

In the present study, the maximum was typically found close to the center of the chain.
(ii) As a measure which excludes the Trotter error I use the *forth-back deviation* $FB(t)$, which I define as the deviation between the initial state $|\mathrm{ini}\rangle$ and the state $|fb(t)\rangle = U(-t)U(t)|\mathrm{ini}\rangle$, i.e. the state obtained by evolving $|\mathrm{ini}\rangle$ to some time t and then back to $t = 0$ again. If the the time evolution operator $U(-t)$ is Trotter-decomposed into odd and even bonds in the reverse order of the decomposition of $U(t)$, the identity $U(-t) = U(t)^{-1}$ holds without any Trotter error, and the forth-back deviation has the appealing property to capture the truncation error only. In contrast to the magnetization deviation, the forth-back error does not rely on the existence of an exact solution.

As the present DMRG setup does not allow easy access to the fidelity $|\langle \mathrm{ini}|fb(t)\rangle|$, I define the forth-back deviation to be the L_2 measure for the difference of the magnetization profiles of $|\mathrm{ini}\rangle$ and $|fb(t)\rangle$,

$$FB(t) = \left(\sum_n \left(\langle \mathrm{ini}|S^z_n|\mathrm{ini}\rangle - \langle fb(t)|S^z_n|fb(t)\rangle \right)^2 \right)^{1/2}. \tag{5.9}$$

In order to control Trotter and truncation error, two DMRG control parameters are available, the number of DMRG states m and the Trotter time step dt.

To study the effect of varying dt, consider the *magnetization deviation* as shown in Fig. 5.2. Two main observations can be made. At small times (regime A), the magnetization deviation decreases with dt and is linear in t as expected from the Trotter error. Indeed, as shown in the upper part of Fig. 5.3, the magnetization deviation depends quadratically on dt for fixed t, and the Trotter error dominates over the truncation error. At large times (regime B), the magnetization deviation is no longer linear in t, but grows almost exponentially, and also does no longer show simple monotonic behaviour in dt: The magnetization deviation in this regime is obviously no longer dominated by the Trotter error, but by the accumulated truncation error.

The two regimes A and B are very clearly separated by some *runaway time* t_R, with regime A for $t < t_R$ and regime B for $t > t_R$ (a precise procedure for its determination will be outlined below). The runaway time t_R increases when dt is increased: Because the total number of Trotter time steps t/dt is

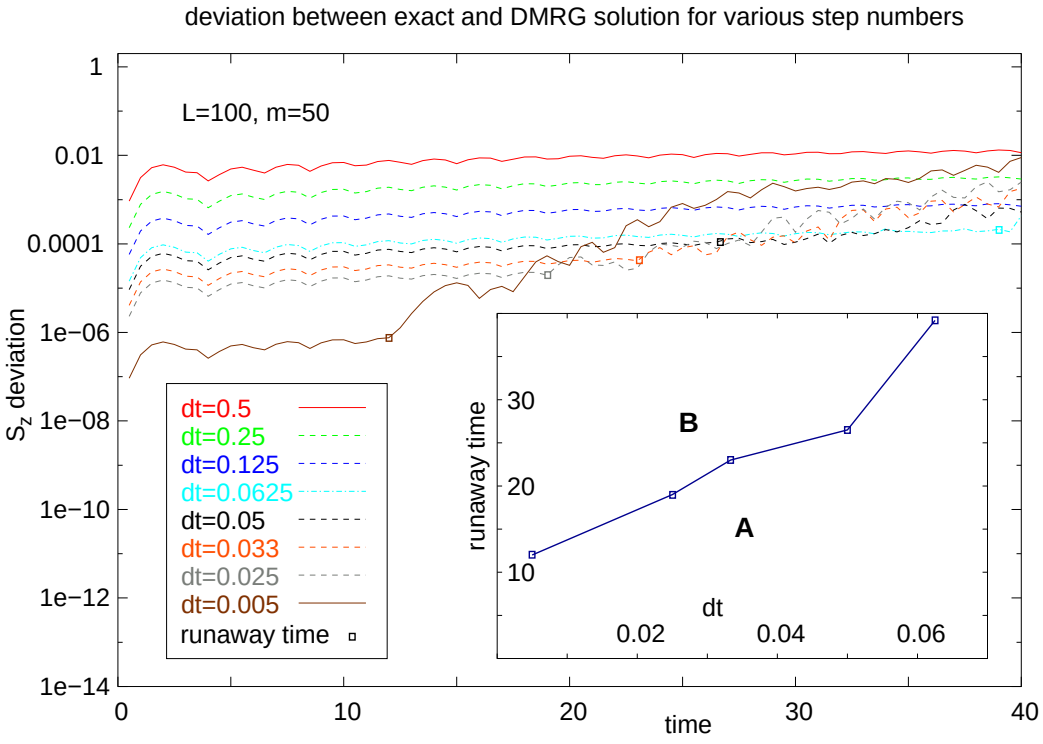

Figure 5.2: Magnetization deviation as a function of time for different Trotter time steps dt and for $m = 50$ DMRG states. At small times (region A in the inset), the deviation is dominated by the linearly growing Trotter error for small times. At later times (region B in the inset), much faster, non-linear growth of the deviation sets in at some well-defined runaway-time t_R. As shown in the inset, t_R increases with increasing dt.

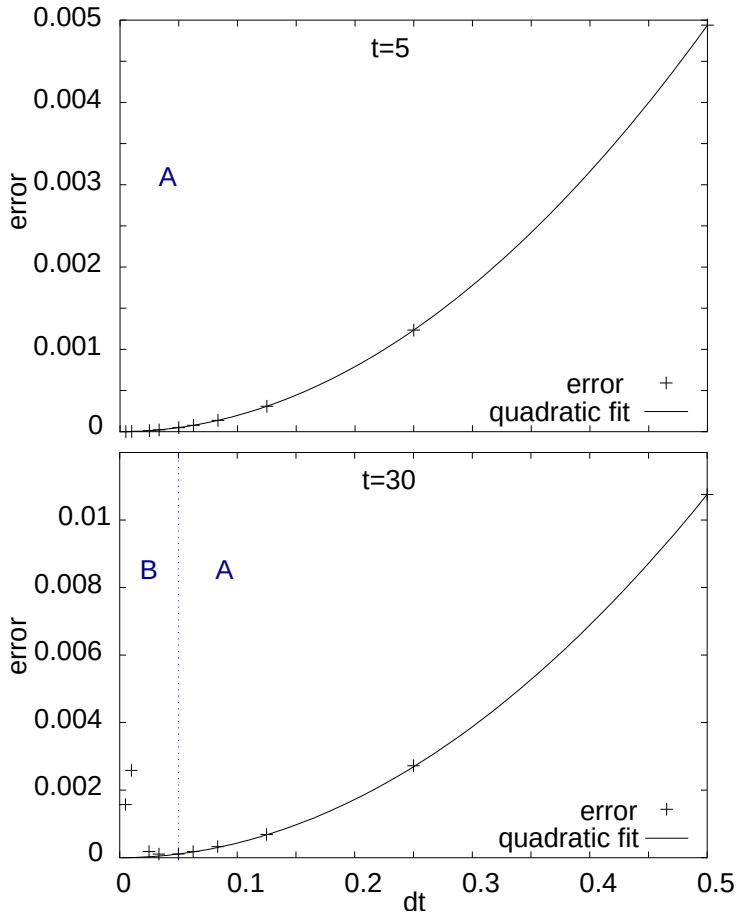

Figure 5.3: Magnetization deviation as a function of Trotter time step dt (system size $L = 100$, $m = 50$ DMRG states) at times $t = 5$ (upper figure) and $t = 30$ (lower figure). For $t = 5$, the magnetization deviation is quadratic in dt as expected from the Trotter error. For $t = 30$, at small dt the magnetization deviation is no longer quadratic in dt and larger than the Trotter error would suggests. This is a signal of the contribution of the accumulated truncation error.

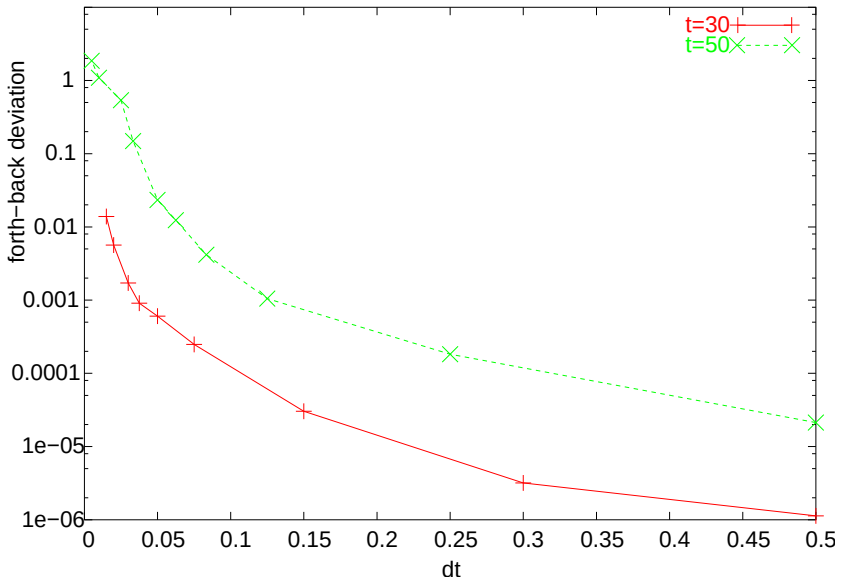

Figure 5.4: The forth-back error $FB(t)$ for $t = 30$ and $t = 50$, as function of dt. Here, $L = 100$, $m = 50$.

decreased, the accumulated truncation error decreases, and the Trotter error increases, hence the competing two errors break even later.

This dt-dependence of t_R is also seen in the lower part of Fig. 5.3, where the dt dependence of the magnetization deviation is plotted at some larger time ($t = 30$) than in the upper part. $t = 30$ is larger than the runaway time (i.e. in regime B) for $dt \leq 0.05$, in regime A otherwise. In the insert of Fig. 5.2, one sees for $dt > 0.05$ (region A) indeed the familiar quadratic Trotter error dependence. For small $dt \leq 0.05$ (region B), the deviation is dominated by the accumulated truncation error that increases as dt decreases. This is reflected in the growth of the magnetization deviation as dt is *de*creased.

The almost exponential growth of the truncation error with the number of Trotter steps can also be seen from the forth-back deviation that is not susceptible to the Trotter error. In Fig. 5.4, I show the forth-back deviation $FB(t)$ for $t = 30$ and $t = 50$ as a function of the Trotter time step dt. $FB(t)$ increases as a consequence of the stronger accumulation of the truncation error with decreasing Trotter step size dt and hence an increasing number of steps t/dt.

Let me now consider the dependence of the magnetization deviation $\mathrm{err}(t)$ on the second control parameter, the number m of DMRG states. In Fig. 5.5, $\mathrm{err}(t)$ is plotted for a fixed Trotter time step $dt = 0.05$ and different values

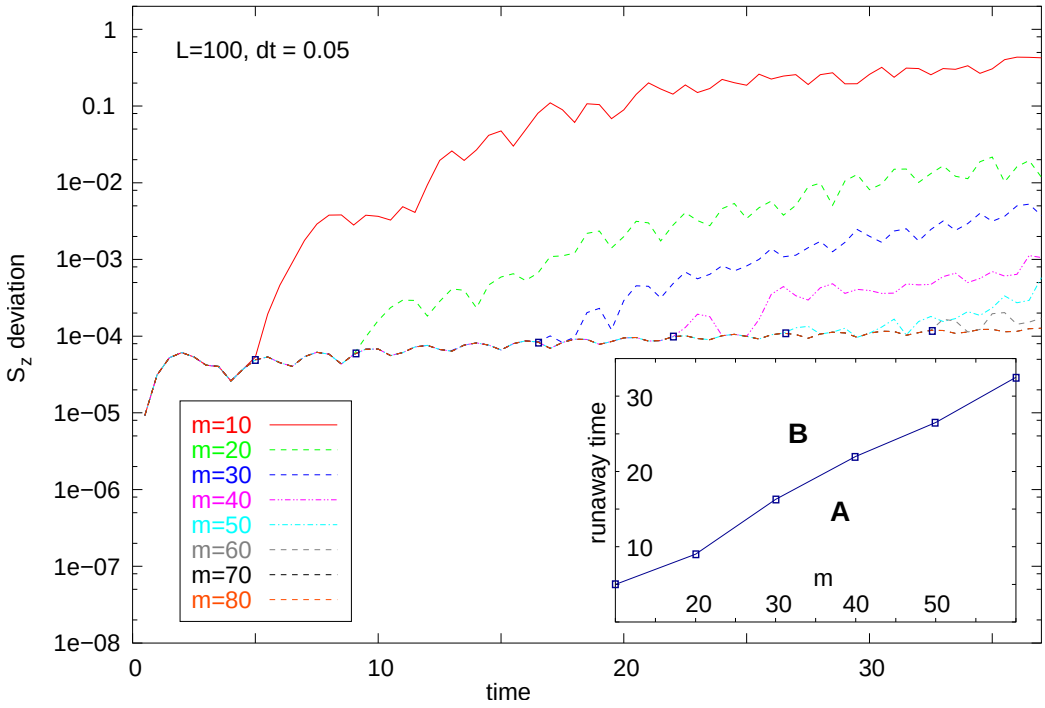

Figure 5.5: Magnetization deviation $\Delta M(t)$ as a function of time for different numbers m of DMRG states. The Trotter time interval is fixed at $dt = 0.05$. Again, two regimes can be distinguished: For early times, for which the Trotter error dominates, the error is slowly growing (essentially linearly) and independent of m (regime A); for later times, the error is entirely given by the truncation error, which is m-dependent and growing fast (almost exponential up to some saturation; regime B). The transition between the two regimes occurs at a well-defined "runaway time" t_R (small squares). The inset shows a monotonic, roughly linear dependence of t_R on m.

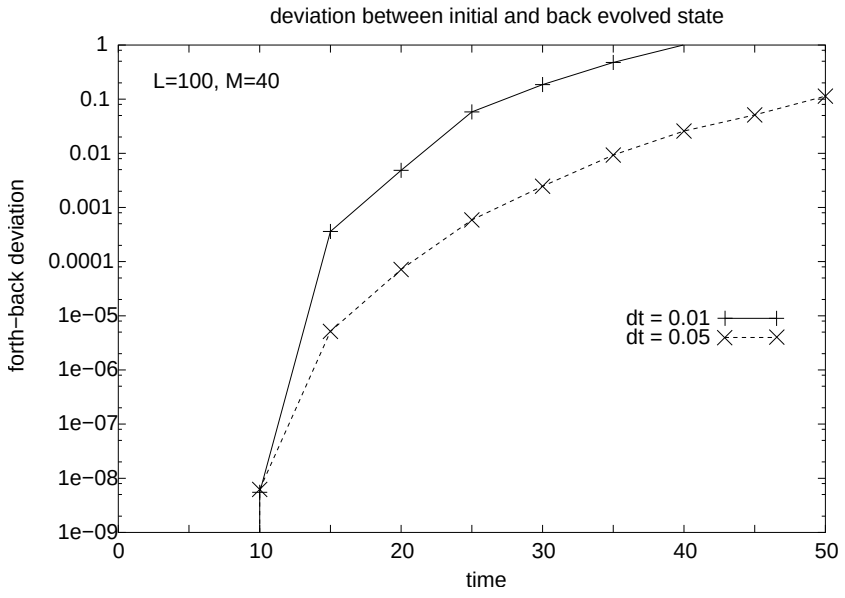

Figure 5.6: The forth-back error $FB(t)$ for $L = 100$, $m = 40$, $dt = 0.01$ and $dt = 0.05$, as function of t.

of m. In agreement with the previous observations, some m-dependent "runaway time" t_R, separates two regimes: for $t < t_R$ (regime A), the deviation grows essentially linearly in time and is independent of m, for $t > t_R$ (regime B), it suddenly starts to grow more rapidly than any power-law. The onset of a significant m-dependence has indeed been the operational definition of t_R in Fig. 5.2 and 5.5. In the inset of Fig. 5.5, t_R is seen to increase roughly linearly with growing m. As $m \to \infty$ corresponds to the complete absence of the truncation error, the m-independent bottom curve of Fig. 5.5 is a measure for the deviation due to the Trotter error alone and the runaway time can be read off very precisely as the moment in time when the truncation error starts to dominate.

That the crossover from a dominating Trotter error at short times and a dominating truncation error at long times is so sharp may seem surprising at first, but can be explained easily by observing that the Trotter error grows only linearly in time, but the accumulated truncation error grows almost exponentially in time. The latter fact is shown in Fig. 5.6, where the forth-back deviation $FB(t)$ is plotted as a function of t for some fixed m. Here, one finds that the effects of the truncation error are below machine precision for $t < 10$ and then grow almost exponentially in time up to some saturation.

By comparison, consider Fig. 5.7, where $FB(t)$ is plotted as a function

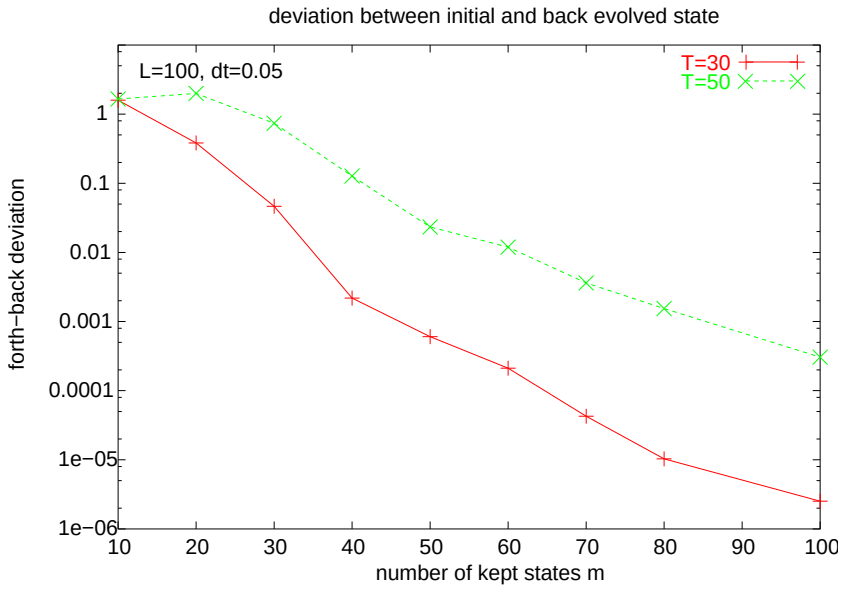

Figure 5.7: The forth-back error $FB(t)$ for $t = 50$ and $t = 30$, as function of m. Here, $L = 100$, $dt = 0.05$.

of m, for $t = 30$ and $t = 50$. An approximately exponential increase of the accuracy of the method with growing m is observed for a fixed time. My numerical results that indicate a roughly linear time-dependence of t_R on m (inset of Fig. 5.5) are the consequence of some balancing of very fast growth of precision with m and decay of precision with t.

Before concluding this section, let me briefly consider a number of other possible effects that might affect t_R. One might alternatively conceive that the well-defined runaway-time t_R results from a sudden failure (of stochastic or of fundamental nature) of the truncation algorithm to capture one important basis state. It can be refuted on the basis of Fig. 5.4, Fig. 5.6 and Fig. 5.7: Such an error should manifest itself as a pronounced step in $FB(t)$, depending on the time evolution having gone past t_R or not. Such a step is, however, not observed.

t_R might also be thought to reflect a fundamental DMRG limit, namely a growth of the entanglement within the time-evolved state which the limited number of DMRG states m is not able to capture adequately at $t > t_R$. This scenario can be excluded by observing the strong dependence of t_R on the number of time steps, which this scenario cannot explain. Indeed, a study of the entanglement entropy between the left and the right half of the chain

$$S_e(t) = \mathrm{Tr}\hat{\rho}\log_2\hat{\rho}, \tag{5.10}$$

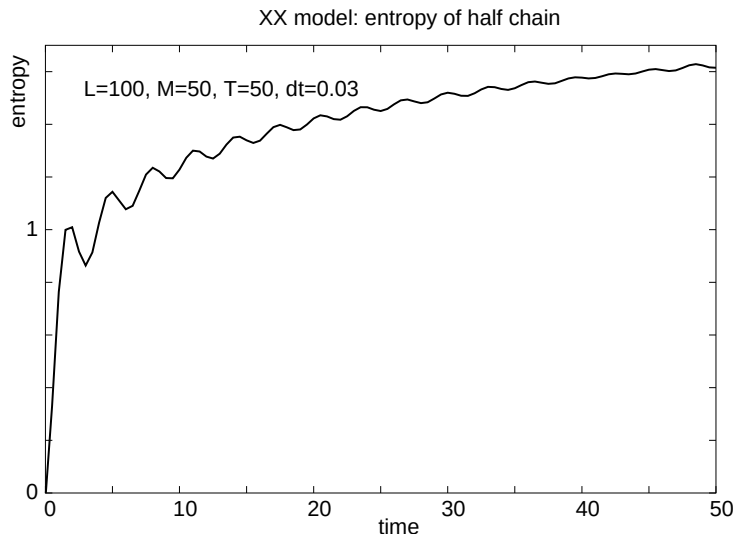

Figure 5.8: Entanglement entropy S_e from Eq. (5.10) between the left and the right half of the chain as function of time.

$\hat{\rho}$ being the reduced density matrix of the left (or equivalently the right) half of the chain, confirms this view: As shown in Fig. 5.8, $S_e(t)$ is only mildly growing with time and is well below the maximum entanglement entropy $S_{\max} \sim \log_2 m$ that the DMRG can reproduce.

Therefore I conclude that the error at short times is dominated by the Trotter error, which is independent of m and approximately growing linearly with time. At some runaway time, one observes a sharp crossover to a regime in which the m-dependent and almost expontially growing truncation error is dominating. This crossover is sharp due to drastically different growth of the two types of errors. The runaway time thus indicates an imminent breakdown of the method and is a good, albeit very conservative measure of available simulation times. I expect the above error analysis for the adaptive t-DMRG to be generic for other models. The truncation error will remain also in approaches that dispose of the Trotter error; maximally reachable simulation times should therefore be roughly the same or somewhat shorter if other approximations enhance the truncation error.

5.4.3 Optimal choice of DMRG parameters

How can the overall error – which was found to be a delicate balance between the Trotter and the accumulated truncation error – be minimized and the important runaway time be found in practice? From the above scenario it

should be expected that the truncated density matrix weight at each step does not behave differently before or after the runaway time and hence is no immediately useful indicator to identify the runaway time. This can in fact be seen from Fig. 5.9, where the truncated weight is shown for the same parameters as in Fig. 5.2. Also, it is not obvious to extract a precise relationship between the truncation errors at each DMRG truncation and the accumulated errors. Instead, a precise convergence analysis in m or dt seems to be more telling and easily feasible.

Of course, it is desirable to choose the number of kept states m as large as possible within the constraints regarding the available computer resources. This choice having been made, the runaway time t_R is determined for different Trotter time steps dt by comparing different values of m as in Fig. 5.5. Only two slightly different values of m are sufficient for that purpose. Now the Trotter time step dt is chosen such that the desired time t is just below t_R. This way, the optimal balance between the Trotter error and the truncation error is found, which corresponds in the lower part of Fig. 5.3 to the minimum of $\mathrm{err}(t)$ on the border between regime A and B: The total error would increase at larger dt due to the Trotter error, and at smaller dt due to the truncation error.

Thus, it is a good practice to choose for small times rather small values of dt in order to minimize the Trotter error; for large times, it makes sense to choose a somewhat coarser time interval, in order to push the runaway time to as large values as possible.

In terms of numbers of time steps, I conclude from Fig. 5.2 that for the present model and parameters ($L = 100 - 200$), the adaptive time-dependent DMRG seems to be able to perform about 1000-5000 time steps reliably even for $m = 50$, depending on the desired level of accuracy. I note that this is a very small value of m by DMRG standards, and that using an optimized code, one should be able to increase m by an order of magnitude.

5.5 Long-time properties of the time-evolution

In [ARRS99; HRS04], the time evolution of the initial state $|\mathrm{ini}\rangle$ on the XX chain at temperature $T = 0$ was examined in the long-time limit using the exact solution. It was found that the magnetization $S_z(n,t)$ given in Eq. (5.4) can be described for long times in terms of a simple scaling function, $S_z(n,t) \approx \Phi\left((n - n_c)/t\right)$, where n_c is the position of the chain center. The scaling function is the solution of the partial differential equation $\partial_t S_z + \partial_x j(S_z) = 0$ with the magnetization current $j(S_z) = 1/\pi \cos|\pi S_z|$ which has been shown to describe the macroscopic time evolution of the magnetization

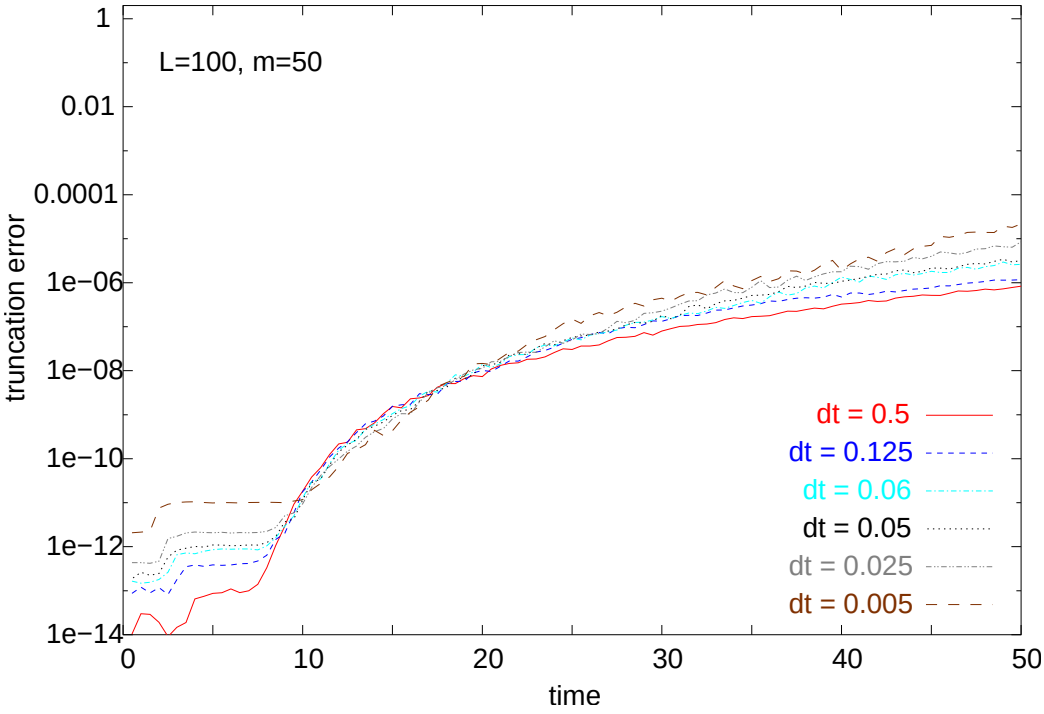

Figure 5.9: The lost weight in the density matrix truncation, summed over time intervals $\Delta t = 0.1$, is shown for the same parameters as in Fig. 5.2. A comparison with Fig. 5.2 reveals, however, that both values are not useful criteria for the DMRG truncation error and are in particular not suited to reveal the runaway time t_R.

profile [ARRS99]. The characteristics, i.e. the lines of constant magnetization S_z, have a slope $v = \sin|\pi S_z|$.

The magnetization profile $\Phi\left((n-n_c)/t\right)$ has a well-defined front at $(n-n_c)/t = \pm 1$, i.e. is moving outwards ballistically with velocity $v = 1$. On top of this overall scaling form an additional step-like substructure arises, which was analysed in detail in [HRS04]. It was found that while the step width broadens as $t^{1/3}$, the step height decreases as $t^{-1/3}$, such that the integrated transported magnetization within each step remains constant at 1. It was suggested that each of these steps corresponds to a localized flipped spin flowing outwards.

The XX model, however, has several very special properties: It corresponds to a free-fermion model and is therefore exactly solvable; it is critical; and its total current operator $J = \sum_n j_n$ commutes with the Hamiltonian, $[J, H] = 0$. One may ask whether the above findings are due to any of the particularities of the XX model or more generic.

The adaptive t-DMRG allows me to study the long-time evolution of $|\mathrm{ini}\rangle$ in different coupling regimes of Eq. (5.1). I chose two extensions of the XX model, namely a S^zS^z- interaction, and dimerization.

In Fig. 5.10 and 5.11, I visualize the time evolution of the local magnetization in density plots, with site index n on the x-axis, time t on the y-axis. Here, the absolute value of the magnetization is shown as a grayscale and in lines of constant magnetization at $|\langle S_z\rangle| = 0.2, 0.4$. In Fig. 5.10, the relation between the density plots and the actual magnetization profile for the XX model is shown at two times, $t = 0$ and $t = 40$. The exact solution is perfectly reproduced, including the detailed substructure of the magnetization profile.

In Fig. 5.11, density plots for various values of J_z between 0 and 1.1 are shown. For small J_z ($J_z < 1$), I observe ballistic transport of the magnetization. This regime is characterized by a constant transport velocity of the magnetization, hence the lines of constant magnetization shown in Fig. 5.11 are approximately straight for $J_z < 1$. The magnetization front propagation slows down as J_z increases, and almost comes to a halt when $J_z > 1$. Although the sharpness of this crossover at $J_z = 1$ is surprising, its general nature can be understood from the limits $J_z \to 0$ and $|J_z| \to \infty$: For small $J_z \to 0$ the S^xS^x- and S^yS^y-interactions dominate. Being spin flip terms, they smear out the initially hard step profile in the z magnetization. For large J_z, on the other hand, the S^zS^z-interaction dominates. This term does not delocalize the step profile, and in the limit $|J_z| \to \infty$, the initial state is even a stationary eigenstate of the Hamiltonian.

Besides the structure of the overall front, I also observe for $J_z \neq 0$ remnants of the steplike substructure from the XX model, individual pockets

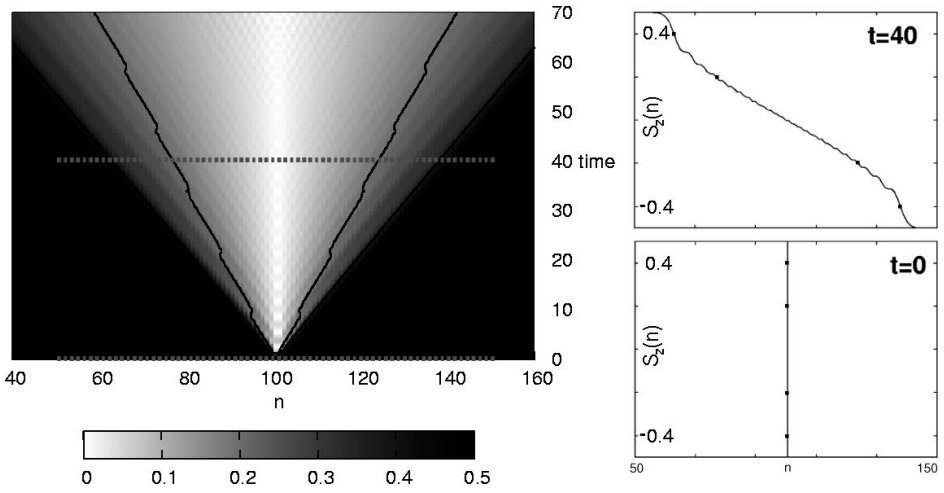

Figure 5.10: Left: Time evolution of the absolute value of the local magnetization $|\langle S_n^z(t)\rangle|$ for the XX model as a density plot, where the local magnetization itself is exactly antisymmetric with regard to the chain center. The lines of constant-magnetization $\langle S_n^z\rangle = \pm 0.2, \pm 0.4$ are shown as solid lines. As an illustration, local magnetizations $\langle S_n^z(t)\rangle$ for the time slices $t = 0$ and $t = 40$ are shown explicitly. A step-like substructure can be seen for $t = 40$ in perfect quantitative agreement with the exact solution. Error bars are below visibility.

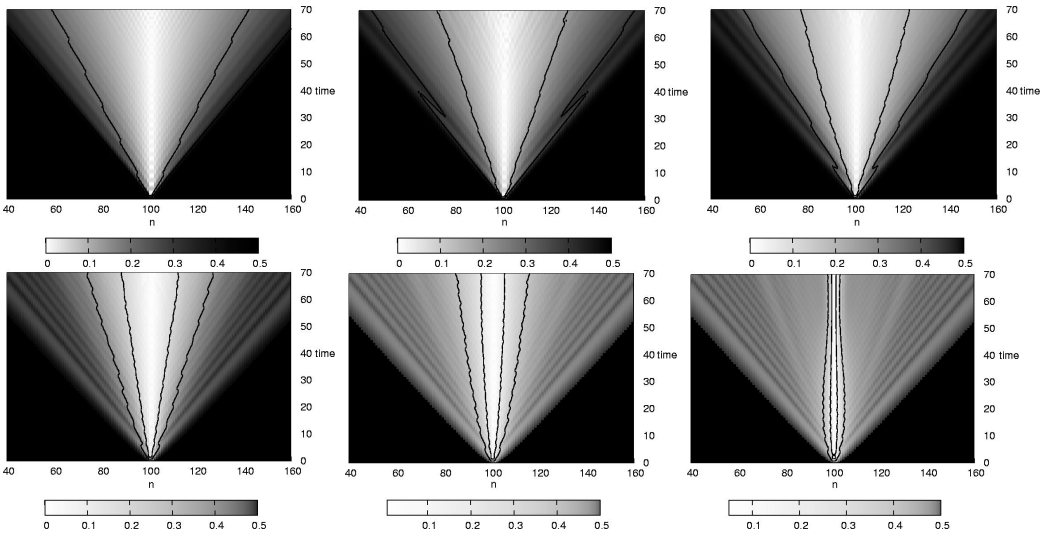

Figure 5.11: Density plots of the magnetization $|\langle S_n^z(t)\rangle|$ as in Fig. 5.10, the values of J_z being (from left to right, top to bottom) 0, 0.3, 0.6, 0.9, 1.0, 1.1, and $\delta = 0$. For better visibility of the profile, the grayscale mapping of $|\langle S_n^z(t)\rangle|$ was chosen differently in each plot as indicated by the legends. Solid lines: lines of constant magnetization $\langle S_n^z\rangle = \pm 0.2, \pm 0.4$; these allow for a direct comparison of the magnetization transport between different J_z. The ray-like structure indicates the "carriers".

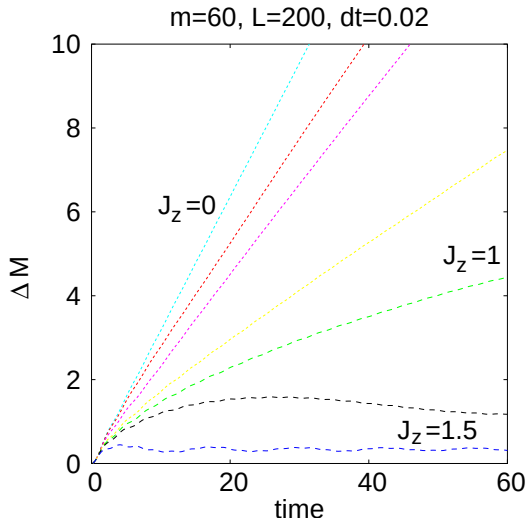

Figure 5.12: The change in the magnetization $\Delta M(t)$ is shown. The curves are plotted in the order J_z =0; 0.3; 0.6; 0.9; 1.0; 1.1; 1.5, where $J_z = 0$ is the steepest. The curves J_z =0; 0.3; 0.6; 0.9 show the same linear behaviour for the observed times, i.e. up to $t = 60$.

of transported magnetization at velocity 1, which I call "carriers". As J_z is increased, these carriers keep the velocity $v \approx 1$, but are increasingly damped and thus less and less effective in transporting magnetization.

In order to put the above observations on a more quantitative footing, I plot in Fig. 5.12 the integrated flow of magnetization through the center,

$$\Delta M(t) = \int_0^t \left\langle j_{L/2}(t')\right\rangle \mathrm{d}t' = \sum_{n>L/2}^{L} (\left\langle S_n^z(t)\right\rangle + 1/2). \tag{5.11}$$

This quantity has the advantage that unlike the lines of constant magnetization in Fig. 5.10 and 5.11, it shows the overall spin transport without being too much biased by single "carriers".

I observe in Fig. 5.12 roughly linear behaviour of $\Delta M(t)$ for $|J_z| < 1$, which suggests ballistic magnetization transport at least on the accessible time scales. As J_z increases, magnetization transport slows down until around $J_z = 1$ the behaviour changes drastically: For $J_z > 1$, $\Delta M(t)$ seems to saturate at a finite value, around which it oscillates. On the time scales accessible, I thus find a sharp crossover at $J_z = 1$ from ballistic transport to an almost constant magnetization.

This crossover is even more clearly visible in Fig. 5.13, where I plot the exponent a of the magnetization, $\Delta M(t) \propto t^a$, for values J_z between 0 and 1.5.

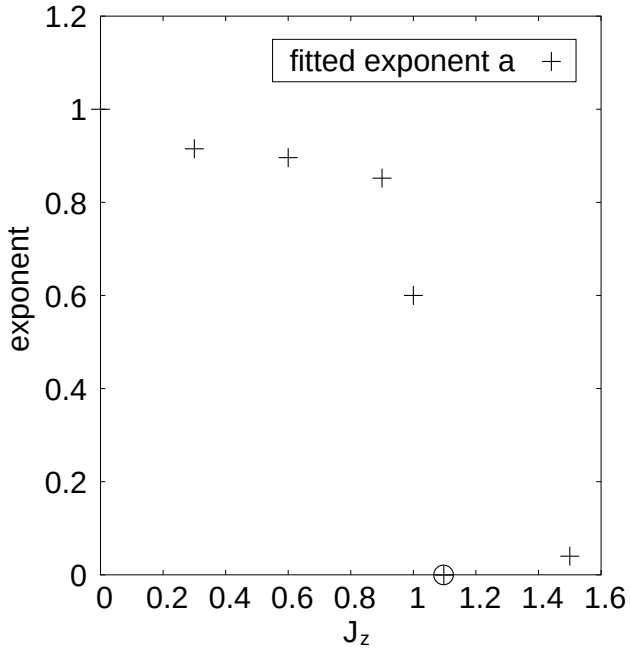

Figure 5.13: Best fit for the exponent a in $\Delta M(t) \propto t^a$, for the data shown in Fig. 5.12 and for times between $t = 20$ and $t = 60$. I estimate the uncertainty in a to be of the order of 0.1 due to the limited time available (cf. Fig. 5.14). It was not possible to fit the slow oscillations for $J_z = 1.1$. To the eye, however, the curve in Fig. 5.12 suggests slow oscillations around a constant value, hence I included in the data point $a = 0$ for $J_z = 1.1$ by hand (encircled).

Here, the exponent a is close to 1 for $J_z < 1$, confirming the roughly linear transport, and quickly drops to zero in the regime of constant magnetization for $J_z > 1$.

Fig. 5.14 illustrates how the exponent a was obtained, for the special case $J_z = 1$. Here the exponent $a = 0.6 \pm 0.1$ indicates that the magnetization transport is clearly not ballistic anymore. In fact, Fig. 5.15 reveals that for long times the magnetization collapses best for a scaling function of the form $S_z(n,t) \sim \phi(n/t^{0.6})$ with an uncertainty in the exponent of approximately 0.1, indicating superdiffusive or diffusive transport in the time range under consideration.

The proposed crossover from ballistic to almost no transport is also visible in the expectation value of the current $j_n = J_n \mathrm{Im}\left(\left\langle S_n^+ S_{n+1}^- 0 \right\rangle\right)$. For $J_z = \delta = 0$, it is known [ARRS99] that the current at the middle of the chain approaches a finite value as $t \to \infty$. This is only possible for ballistic

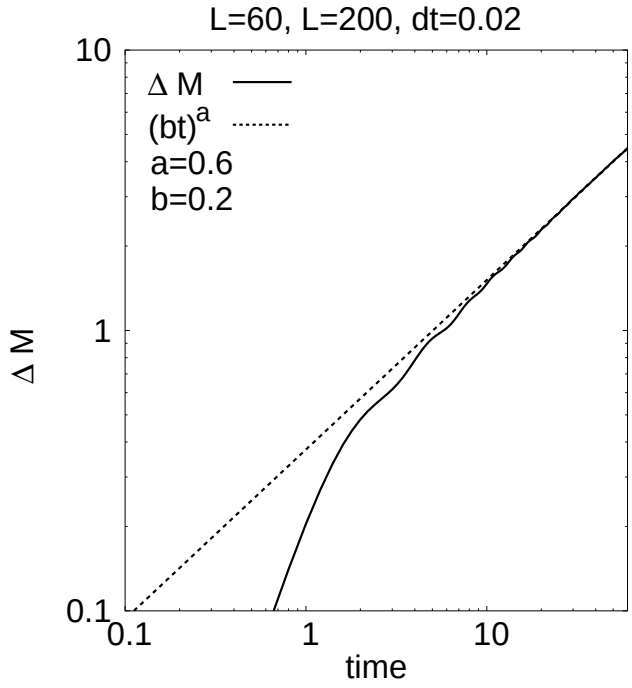

Figure 5.14: $J_z = 1$: The change of the magnetization in a double logarithmic plot with an algebraic fit.

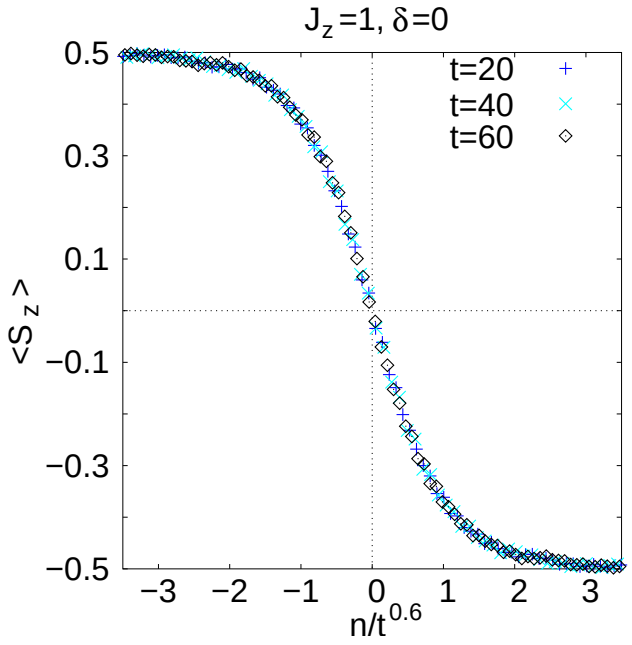

Figure 5.15: $J_z = 1$: Collapse of magnetization for a superdiffusive scaling form $(n/t^{0.6})$.

transport. In the case of (sub- / super-) diffusive transport or constant / oscillatory magnetization, on the other hand, the central current must fall off to zero as the magnetization gradient flattens or must even become negative to allow for the oscillations.

This expected behaviour is seen in Fig. 5.16, where the current at the center of the chain is plotted as a function of time for various values of J_z between 0 and 1.1. I averaged the current over the 5 middle sites in order to filter out local current oscillations. I observe that for relatively long times, the current approaches a constant value for $|J_z| < 1$, whereas the current falls off rapidly and then seems to exhibit damped oscillations around zero for $|J_z| > 1$. This strengthens the previous conclusion of a crossover from ballistic transport to a more or less constant magnetization at $|J_z| = 1$.

Remarkably, this crossover for the behaviour of a high-energy quantum state $|\mathrm{ini}\rangle$ is found at the location $J_z = 1$ of the quantum phase transition from the critical phase to the Néel antiferromagnetic state (see Fig. 5.1), a priori a low-energy event. To understand the subtle connection between the time evolution of $|\mathrm{ini}\rangle$ and the phase transition, I exploit that the time-evolution does not depend on the sign of J_z, as discussed in Sec. 5.2. Therefore the time evolution of the high-energy state $|\mathrm{ini}\rangle$ for $J_z > 1$ is identical to

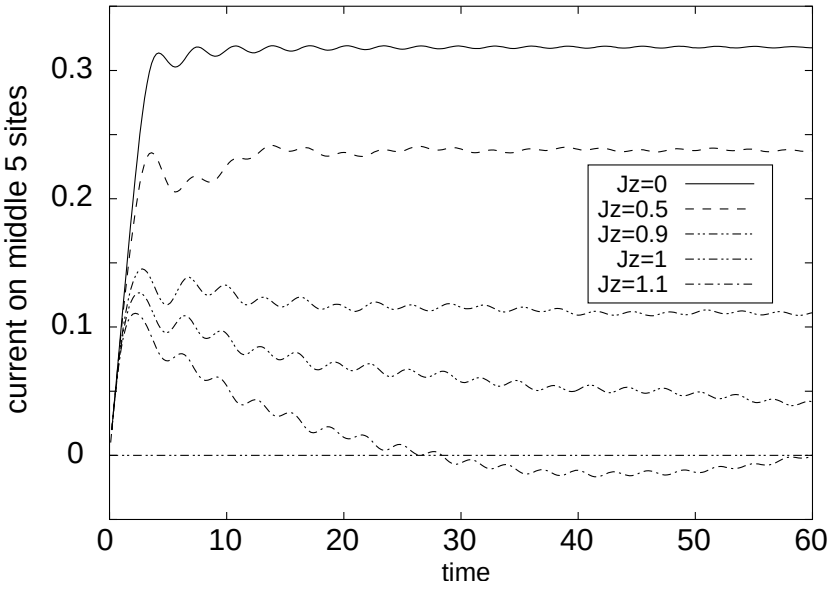

Figure 5.16: Current, averaged over the 5 middle sites, for various values of J_z between 0 and 1.1.

that for $J_z' = -J_z < -1$, where $|\mathrm{ini}\rangle$ is a low-energy state. At the quantum phase transition from the ferromagnetic state to the critical phase at $J_z' = -1$ the ground state, a kink state for $J_z' < -1$ (if one imposes the boundary condition spin up on the left boundary and spin down on the right boundary) [MMR91], changes drastically to a state with no kink and power-law correlations for $J_z' > -1$. Therefore, the initial state is very close to an eigenstate – the ground state – for $J_z' < -1$, but not for $J_z' > -1$. Thus, the harsh change in the time-evolution of the high-energy state $|\mathrm{ini}\rangle$ at $J_z = 1$ can be explained by the severe change in the ground state properties at $J_z' = -1$, and the crossover is linked to a quantum phase transition at a different location in the phase diagram.

I now study the influence of a nonzero dimerization δ in Eq. (5.1). I restrict the analysis to the case $J_z = 0$. The dimerized models can still be described in terms of the free-fermion picture and are exactly solvable (for static properties see [Sch94]). The current, however, is not conserved for nonzero dimerization. This example will shed light on the question whether the long-time limit depends on current conservation or on the free-fermion property, or yet on other special properties of the system. Nonzero dimerization has two obvious and rather trivial effects: Firstly, the overall front velocity should slow down, because the magnetization now propagates faster

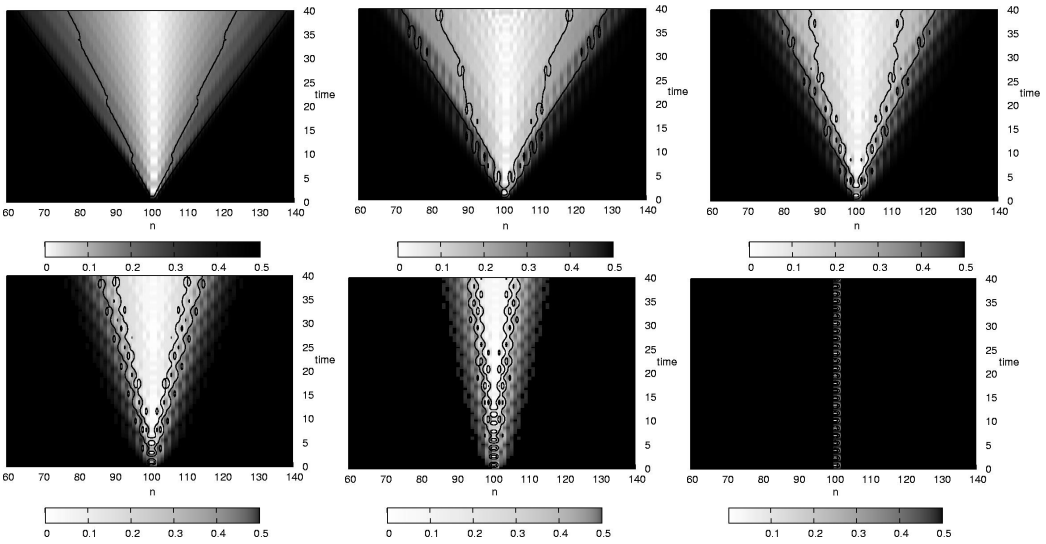

Figure 5.17: Density plots of the magnetization $\langle S_n^z(t)\rangle$ as in Fig. 5.11, for dimerization (from left to right, top to bottom) $\delta = 0$; 0.2; 0.4; 0.6; 0.8; 1.0, and $J_z = 0$. The grayscale mapping is different in each plot as indicated by the legends. Solid lines: lines of constant magnetization $\langle S_n^z\rangle = \pm 0.2, \pm 0.4$.

on half of the links, but slower on the other half, the net effect being a reduction of the total velocity. Secondly, one expects oscillations with a period of two lattice sites. This is obvious in the limit $\delta \to 1$, where each strongly coupled pair of sites can be viewed as an almost isolated subsystem, in which the magnetization oscillates back and forth. Remnants of this behaviour should be present also for dimerizations $|\delta| < 1$.

The data shown in Fig. 5.17 confirms this expectation qualitatively, but does not reveal any other qualitative change of the long-time limit for nonzero dimerization. For $\delta = 1$, the system is trivially given by isolated pairs of neighbouring sites, therefore the propagation velocity drops to zero.

Fig. 5.18 and Fig. 5.19 reveals explicitly that no qualitative change occurs as the dimerization is switched on: the change in magnetization $\Delta M(t)$ still shows the linear behaviour typical of ballistic transport. For increasing $\delta \to 1$ oscillations on top of this linear behaviour arise. I find that switching on finite dimerization does not change the long-time behaviour of the time evolution also for nonzero J_z (not shown). In particular, the time evolution here is drastically influenced by the transition at $J_z = 1$ as in the case $\delta = 0$ discussed above.

To summarize, I find the same long-time behaviour of the initial state $|\uparrow \ldots \uparrow\downarrow \ldots \downarrow\rangle$ in the dimerized system — a system with gapped excitation

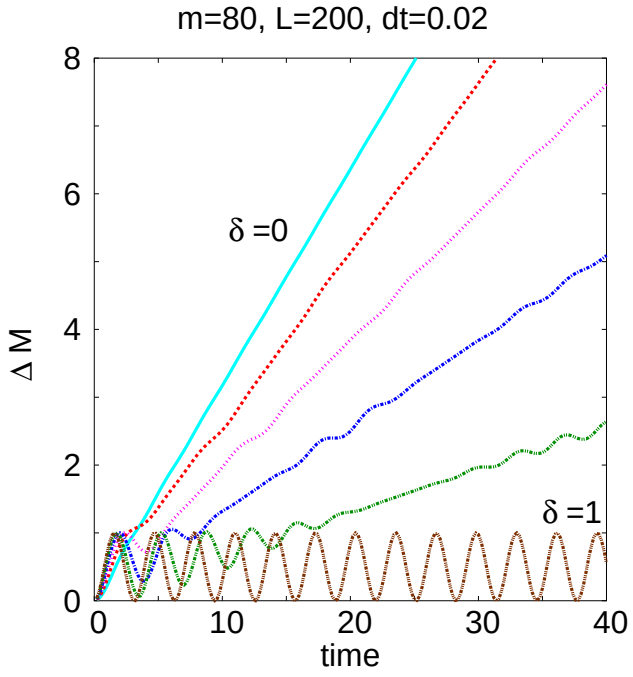

Figure 5.18: Change in magnetization $\Delta M(t)$ for different dimerizations, from top to bottom: $\delta = 0$, 0.2, 0.4, 0.6, 0.8, 1.0.

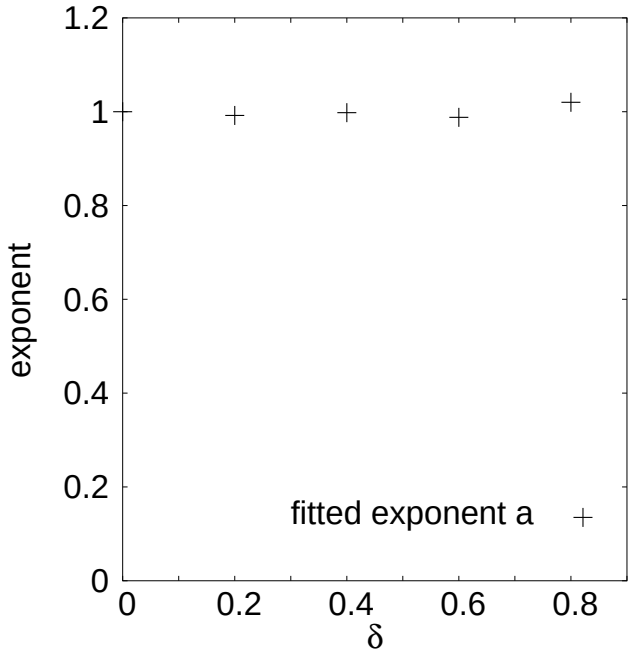

Figure 5.19: Best fit for the exponent a in $\Delta M(t) \propto t^a$, for the data shown in Fig. 5.12 and for times between $t = 20$ and $t = 40$.

spectrum and which is exactly solvable— as in the system with small S^zS^z-interaction, $|J_z| < 1$ — a system which is critical — whereas the behaviour changes drastically for larger S^zS^z-interaction, $|J_z| > 1$. Hence I cannot attribute the ballistic transport of the magnetization to the specific properties of the XX model; neither to be exactly solvable, nor to the continuous spectrum nor to the conserved current in the XX-model. The drastic change at $|J_z| = 1$ stems from the special property of the initial state to resemble the ground state in the ferromagnetic phase and the highest energy state in the antiferromagnetic phase.

Finally, let me include a note on the errors in the present analysis. A convergence analysis in m as in section 5.4 shows that the errors and the runaway time are roughly the same as for the XX model. The plot in Fig. 5.11 goes up to time $t = 95$, whereas the runaway time t_R is somewhat earlier, $t_R \approx 60 - 80$, depending on the precise value of J_z. Indeed, a convergence analysis in m reveals that the accuracy in the central region decreases for $t > t_R$. For dimerized models the runaway time t_R is somewhat shorter (between $t_R = 40$ and $t_R = 80$ for $m = 50$, depending on the dimerization). This fact reflects the reduced accuracy of the DMRG algorithm when dealing with inhomogenous systems. As always, it is possible to increase t_R by increasing m.

5.6 Conclusions

I have investigated the evolution of the initial state $|\uparrow \ldots \uparrow\downarrow \ldots \downarrow\rangle$ under the effect of nearest-neighbour interactions with the adaptive time-dependent DMRG.

For weak S^zS^z-interaction, i.e. $|J_z| < 1$ in Eq. (5.1), and arbitrary dimerization, $0 \leq \delta < 1$, I find that for long times the transport of the magnetization is ballistic as it was found for the XX-model [ARRS99]. The magnetization profile shows the same scaling form for long times, i.e. $S^z(n,t) = \varphi((n-n_c)/t)$, where n_c is the position of the chain center, but with different scaling functions φ. For stronger S^zS^z-interaction, i.e. $|J_z| > 1$, even in a homogeneous system, $\delta = 0$, a drastic change in the long-time evolution is seen. The magnetization transport is no longer ballistic, but shows oscillatory behaviour around a constant value. Hence my results suggest that the specific properties of the XX model are not responsible for ballistic transport at long times. The drastic change in the long time behaviour at the phase transition $J_z = 1$ can be attributed to the close resemblance of the initial state to the ground state for $J_z < -1$.

The error analysis presented here for the adaptive time-dependent DMRG

shows that for small times the error is dominated by the Trotter error whereas for long times the truncation error becomes the most important. This finding should be general and hold for non-exactly solvable models as well, and should therefore allow to control the accuracy of the results from the adaptive time-dependent DMRG in general models.

Chapter 6

Many-body scattering states via DMRG

6.1 Introduction

Transport properties of bulk metals and semiconductors are usually rather well described using perturbative techniques and linear response theory in the applied voltage. However, in mesoscopic structures such as quantum dots, quantum point contacts, or molecular devices, the electron-electron interactions can be particularly strong due to the spatial confinement of the electrons; therefore a number of their transport properties can only be explained by going beyond perturbation theory [GGSM$^+$98; COK98]. Furthermore, a strong bias voltage is usually applied in transport measurements, thus driving the leads far out of equilibrium. This may in some cases invalidate the use of linear response theory.

The goal of this chapter is to formulate a method that describes interacting many-body systems far from equilibrium, and that does not rely on perturbation theory. The approach presented here is based on scattering theory: The goal is to calculate the scattering state $|\psi\rangle$ that emerges when two leads with a chemical potential difference $\Delta\mu = eV$ are coupled via a quantum dot or a quantum point contact (scatterer). Being able to calculate $|\psi\rangle$ for arbitrary voltage V will allow one to obtain the $I-V$-characteristic $I(V) = \langle\psi|\hat{I}|\psi\rangle$ of the scatterer. In contrast to the well-known approach of Landauer and Büttiker [BILP85; Hew97], which is also based on scattering theory, the present approach uses a full many-body formalism in order to allow for a microscopic description of the interactions between the particles.

The strategy for constructing the many-body scattering state $|\psi\rangle$ is to solve the Lippmann-Schwinger equation for many-body states using the DMRG

method. This method, being a numerical one, can only deal with finite systems (of length L, say), whereas scattering theory is properly defined in an infinite system. Moreover, the Lippmann-Schwinger equation has to my knowledge only been used in the context of single-particle quantum mechanics so far. Because the setting is thus doubly unfamiliar, it is certainly worthwhile to have a close look at the foundations of scattering theory first. This is the subject of section 6.2. In section 6.3, I discuss the conditions under which scattering theory is applicable in finite systems. Up to that point, I mainly use one-particle scattering theory. In section 6.4, I generalize the results to many-body scattering states and discuss how the DMRG can be used to obtain these. In section 6.5, I finally give two examples, how the many-body scattering formalism can be implemented.

This entire chapter must be regarded as work in progress. Due to the complexity of the problem, I have been applying the method presented here to model systems only. Further investigations are in order before treatments of realistic physical systems can be expected to yield meaningful results – most notably of the question how to implement the energy shift operator introduced in section 6.3 and the current operator in section 6.5.2 efficiently. Nevertheless, the conceptual framework presented here should be helpful for a reader interested in pursuing this work further.

6.2 Scattering states and the Lippmann-Schwinger equation

In this section, the notion of a scattering state is introduced from a physical point of view. Mostly, the framework of single-particle quantum mechanics is used, but in a way that allows for a straightforward generalization to many-body states, which is the subject of section 6.4 below. The spirit of this section is to state well-known results in an informal way. A more thorough presentation of scattering theory can be found in [GMG53; Wei95; Joa76; Gro60; New82; Tay72; Rom65] Throughout this section, I assume an infinite system and a localized scatterer; systems of finite size are discussed in section 6.3 below.

A typical scattering experiment is illustrated in Fig. 6.1. A free wave comes in from the left; when it scatters on a potential H_s, additional scattered waves come out (implicitly, I have separated the Hamiltonian into a free part H_0 and a localized scattering potential H_s). Scattering theory provides the formal description of such a process.

Conceptually the cleanest way of doing scattering theory is within a time-

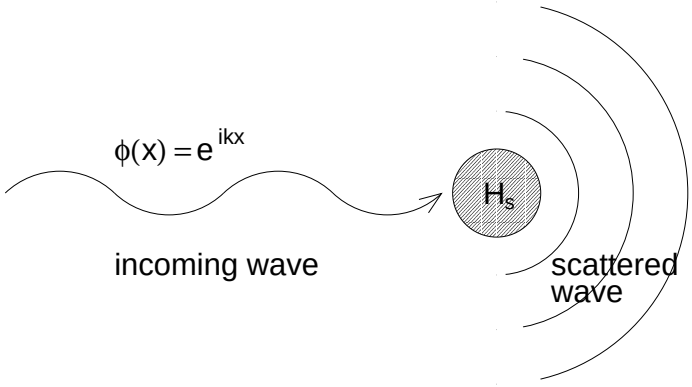

Figure 6.1: Sketch of the scattering process of a single particle on the potential $H_{\rm s}(x)$ in two dimensions. The incoming free wave $\phi(x) = e^{ikx}$ is scattered into a bunch of outgoing waves of the form $\sim e^{ik|r|}/r$. The entire process can be described in terms of a stationary scattering state that contains all of the waves shown.

dependent framework, using wave packets that undergo the scattering process in the temporal order just described. In the distant past (i.e. when the wave packet is far away from the localized scatterer), such a wave packet is given by

$$|\psi(t)\rangle = \int \frac{dk}{2\pi} f(k) e^{i\epsilon_k t} |\phi_k\rangle, \quad t \to -\infty, \tag{6.1}$$

where $f(k)$ is a suitably chosen function, peaked around some momentum k_0 (with width $1/l_{\rm scatt}$, say), such that $|\psi(t)\rangle$ is a wave packet (of width $l_{\rm scatt}$ [1]) that comes in from infinity (i.e. from $x \to -\infty$ as $t \to -\infty$) and hits the potential at $t \approx 0$. $|\phi_k\rangle$ are eigenstates of the free Hamiltonian H_0 with eigenvalues ϵ_k; therefore, Eq. (6.1) represents the true time evolution only as long as t is small enough so that the particles do not "see" the scattering potential $H_{\rm s}$. When the wave packet starts hitting the scatterer at $t \approx 0$, Eq. (6.1) is no longer a valid description of the time evolution. At this time, the scattered waves of Fig. 6.1 emerge.

In order to perform the full time evolution that replaces the asymptotic form of Eq. (6.1), the concept of scattering states is very useful. The retarded scattering states $|\psi_k^{\rm ret}\rangle$ are defined by two properties [Wei95]: Firstly, they

[1] Strictly speaking, the width can depend on time. $l_{\rm scatt}$ is the width of Eq. (6.1) at time $t = 0$.

are eigenstates of the *full* Hamiltonian,

$$H|\psi_k^{\mathrm{ret}}\rangle = \epsilon_k|\psi_k^{\mathrm{ret}}\rangle, \quad H = H^0 + H_{\mathrm{s}}, \tag{6.2}$$

where ϵ_k is the same energy that the free state $|\phi_k\rangle$ has with respect to H^0 (see, however, section 6.3). Secondly, the $|\psi_k^{\mathrm{ret}}\rangle$ satisfy retarded boundary conditions, which means that wave packets in the distant past ($t \to -\infty$) satisfy

$$\int dk f(k) e^{i\epsilon_k t}|\phi_k\rangle = \int dk f(k) e^{i\epsilon_k t}|\psi_k^{\mathrm{ret}}\rangle \quad (\text{for } t \to -\infty). \tag{6.3}$$

Unlike the left hand side, the right hand side of Eq. (6.3) is a perfectly good description of the time evolution for *all* times t because of Eq. (6.2).

Once that the scattering states $|\psi_k^{\mathrm{ret}}\rangle$ are known, it is not necessary anymore to form wave packets as in Eq. (6.1). Instead, it is possible to perform the limit that the k-width $1/l_{\mathrm{scatt}}$ goes to zero, thus producing the delocalized state $|\psi_{k_0}^{\mathrm{ret}}\rangle$ itself, from which all properties of the scattering process can be read off directly.

The scattering states $|\psi_k^{\mathrm{ret}}\rangle$ that satisfy the above two conditions can be obtained by solving the Lippmann-Schwinger equation [Wei95]

$$|\psi_k^{\mathrm{ret}}\rangle = |\phi_k\rangle + \frac{1}{E - H_0 + i\eta} H_{\mathrm{s}}|\psi_k^{\mathrm{ret}}\rangle, \tag{6.4}$$

where $E = \epsilon_k$ is the energy of the "incoming state" $|\phi_k\rangle$ with respect to the free Hamiltonian H^0, and $\eta \xrightarrow{>} 0$ is an infinitesimally small energy. I keep a distinction – which is at this point purely formal – between the parameter E that enters Eq. (6.4) and the free energy ϵ_k, because it turns out that in *finite* systems, it can become necessary to introduce an "energy shift" between E and ϵ_k. This issue is discussed in section 6.3 below.

Another useful form of the Lippmann-Schwinger equation is obtained from Eq. (6.4) using elementary algebra:

$$|\psi_k^{\mathrm{ret}}\rangle = \frac{i\eta}{E - H + i\eta}|\phi_k\rangle, \tag{6.5}$$

This latter form makes it obvious that $|\psi_k^{\mathrm{ret}}\rangle$ satisfies, in the limit $\eta \to 0$, the condition of Eq. (6.2): The operator on the right hand side of Eq. (6.5) projects the incoming state $|\phi_k\rangle$ onto the eigenspace of the full Hamiltonian $H = H_0 + H_{\mathrm{s}}$ with eigenvalue $E = \epsilon_k$.

Equivalently to the above discussion, the scattering state $|\psi_k^{\mathrm{ret}}\rangle$ can also be represented in terms of the time evolved free state $|\phi_k\rangle$ from $t = t' < 0$ to $t = 0$, in the interaction picture given by

$$|\phi_k(t', 0)\rangle = e^{-iH(-t')} e^{i\epsilon_k(-t')}|\phi_k\rangle. \tag{6.6}$$

Indeed, $|\psi_k^{\rm ret}\rangle$ is a coherent superposition of these states [GMG53], namely

$$|\psi_k^{\rm ret}\rangle = \eta \int_{-\infty}^{0} dt' e^{-\eta|t'|} |\phi_k(t',0)\rangle. \tag{6.7}$$

It is straightforward to show that integration of Eq. (6.6) and Eq. (6.7) indeed yields the Lippmann-Schwinger equation Eq. (6.5). In this picture, the factor $e^{-\eta|t'|}$ in Eq. (6.7) (again with $\eta \stackrel{>}{\to} 0$) is seen to switch on the potential smoothly and thus to provide a temporal cutoff at $t' = -\eta^{-1}$. In this sense, one may say that $|\psi_k^{\rm ret}\rangle$ is given by the time evolution of the free state $|\phi_k\rangle$ from $t = -\eta^{-1}$ to $t = 0$.

If one switches the sign of η to $\eta < 0$, one obtains the advanced scattering state, which evolves into the corresponding free state as $t \to +\infty$. This state is, however, of no further interest.

6.3 Scattering "theory" in a finite system

6.3.1 General considerations

So far, it was crucial that the system is infinite and therefore has continuous level spacing. This assumption entered twice in the previous discussion: Firstly in order to describe in Eq. (6.1) and Eq. (6.3) a wave packet coming in from infinity, and secondly to perform the limit that the wave packet becomes infinitely sharp in momentum. In the numerical application of the Lippmann-Schwinger equation using the DMRG, one is restricted to finite systems (of length L, say), and may perform the limit $L \to \infty$ as an extrapolation only. In this section, I address some of the general issues that are important for scattering theory at finite L.

1. In a finite system, the introduction of a localized scatterer $H_{\rm s}$ generally leads to energy shifts in the spectrum, i.e. the eigenvalues ϵ_k of the free Hamiltonian H_0 and E_k of the full Hamiltonian $H = H_0 + H_{\rm s}$ are in general not equal.[2] As a consequence, Eq. (6.2) cannot be fulfilled rigorously.

   A formal solution of this puzzle is given in [GMG53; Rom65], where a level shift operator $\Delta = \sum_k |\phi_k\rangle(E_k - \epsilon_k)\langle\phi_k|$ is defined. Then, $\tilde{H}_0 = H_0 + \Delta$ is considered as the free, $\tilde{H}_{\rm s} = H_{\rm s} - \Delta$ as the interacting Hamiltonian, such that $\tilde{H}_0$ and the full Hamiltonian $H = \tilde{H}_0 + \tilde{H}_{\rm s}$

[2] Such energy shifts can occur in infinite systems as well, see e.g. [GMG53].

now have the same spectrum $\{E_k\}$ by definition. If the Lippmann-Schwinger equation is evaluated as in Eq. (6.5) (which just contains the full Hamiltonian H), the only consequence of the level shift operator Δ is that the parameter E in Eq. (6.5) must be chosen not to be the free energy ϵ_k, but the interacting energy E_k instead.

Under the condition

$$\eta \gg |E_k - \epsilon_k|, \tag{6.8}$$

the difference between $E = \epsilon_k$ and $E = E_k$ is not important in Eq. (6.5), and thus the level shifts can be neglected entirely. If Eq. (6.8) is not fulfilled, however, the energy shifts must be accounted for: otherwise, Eq. (6.5) does not reproduce the correct scattering state.

Condition Eq. (6.8) is automatically fulfilled for a single particle in a local scattering potential (such as the one used in section 6.3.2): Here, the level shift is related to the scattering phase shift ϕ_k via $E_k - \epsilon_k = \phi_k \cdot v_k/L$. Because typically $\phi_k \leq 2\pi$, the level shift is of the order of the energy level spacing v_k/L, and Eq. (6.8) follows from Eq. (6.10) below [DeW56].

This argument is, however, not applicable for the many-particle scattering states discussed in section 6.4 below, the level shifts of all occupied levels may add up. For example, in the Kondo model, the sum of the energy shifts of all occupied levels is of the order of the Kondo temperature T_K and therefore even persists in the continuum limit $L \to \infty$. Therefore, it is crucial to have a good estimate of the difference between the free energy ϵ_k and the corresponding full energy E_k (where k now indicates a general index that characterizes a many-body state).

At this point, it is an open question how to calculate the energy E_k corresponding to the free energy ϵ_k most efficiently, and thus how to determine the parameter $E = E_k$ that enters the Lippmann-Schwinger equation (6.5). In the absence of level crossings, E_k can in principle be obtained by observing the evolution of the eigenenergy E_k^α of

$$H^\alpha = H_0 + \alpha H_s \tag{6.9}$$

as α is being switched on smoothly from 0 to 1. This approach is, however, not practical. A more feasible approach might be to assume that the energy shift is independent of the many-body state index k and thus can be obtained as the difference of the ground state energies of H_0 and H. Then, η must only be larger than the remaining uncertainty in E_k, which may be a much weaker condition than Eq. (6.8).

The DMRG algorithm – whose adaptation to the scattering problem is discussed in section 6.4 below – is an iterative method, in which sites or energy levels are added successively to an initially small system (in the "infinite-size" formulation of the algorithm, see chapter 2). Therefore, the total energy shift will gradually increase as the individual energy shifts of more and more particles accumulate. It may be a promising strategy to follow the evolution of the energy level shift as new levels are added in the DMRG algorithm, rather than following it for increasing α in Eq. (6.9). Details of this procedure have yet to be worked out.

2. The condition

$$\eta \gg v_k/L \tag{6.10}$$

must be fulfilled at finite L. Here, the right hand side of the inequality is the single-particle energy level spacing. This condition is necessary in order to obtain a meaningful distinction between retarded ($\eta > 0$) and advanced ($\eta < 0$) solutions of Eq. (6.5) (at least for the single-particle states). This condition makes sense on a less formal and more physical level as well: Because the precise boundary conditions imposed in a finite system should not matter, the time evolution had better be damped or cut off (at time η^{-1}) before the time L/v_k it takes for the particle to travel from the boundary to the scattering center.

3. Because one cannot perform the full limit $\eta \to 0$ right away, one should be aware that properties of the scattering state can only be trusted on a distance scale

$$l_{\mathrm{scatt}} < v_k/\eta \tag{6.11}$$

away from the scatterer: This is because the temporal cutoff η^{-1} allows the scattered particles to have propagated only to a distance v_k/η. Thus, a second length scale l_{scatt} must be introduced that corresponds to the distance to which the information about the scatterer has been spread.

Summarizing this section, if the system size L is finite, one must choose a finite value of η in Eq. (6.5) and introduce a length scale l_{scatt} such that the inequality

$$l_{\mathrm{scatt}} \ll v_k/\eta \ll L \tag{6.12}$$

is fulfilled. In many-body systems, Eq. (6.8) must be imposed additionally, or the level shifts must be compensated otherwise as discussed above.

6.3.2 Example: Single particle with a δ potential

It is instructive to illustrate the above considerations (in particular, the necessity of a second length scale l_{scatt}) using a simple example: a single particle in one dimension with a delta-like scattering potential $H_{\mathrm{s}}(x) = \lambda\delta(x)$, the incoming state having momentum k. Without loss of generality, I assume $k_0 > 0$. An elementary solution to this problem for $\eta = 0$ can be found in [Gri94].

In a finite system of length L, the momentum k is a discrete variable. Nevertheless, the sum over k is well approximated by an integral, $\sum_k \approx (L/2\pi)\int dk$ as long as η is kept finite (more precisely, as long as the conditions Eq. (6.10) and $k_0 x \ll 1$ are met in all equations of this section.[3]) Under these conditions – which I assume from now on – the only complication due to the finite system length L is that the strict limit $\eta \to 0$ is not possible. In this spirit, I use the above notation for sums over k.

For a delta potential, the solution of the Lippmann-Schwinger equation, Eq. (6.5), can be written in a closed form as

$$\psi(x)_{k_0} = \int \frac{dk}{2\pi}\tilde{\psi}_{k_0}(k)e^{ikx}, \quad \tilde{\psi}_{k_0}(k) = 2\pi\delta(k-k_0) + \frac{\alpha}{\epsilon_{k_0} - \epsilon_k + i\eta}. \quad (6.13)$$

Here, $\alpha = \lambda\psi(x{=}0)$ and $2\pi\delta(k-k_0)$ is a shorthand notation for $L\delta_{kk_0}$.

In order to evaluate Eq. (6.13) further, it is advantageous to linearize the dispersion relation; this is possible because only energies around ϵ_{k_0} (i.e. near the poles in Eq. (6.13)) matter. After an unimportant shift of the energy origin, I introduce left- and right-movers (which are distinguished by the sign of k) with energies $\epsilon_k = v_{k_0}\cdot|k|$ with $v_{k_0} = \partial\epsilon_k/\partial k|_{k_0}$.

Eq. (6.13) can then be recast as

$$\tilde{\psi}_{k_0}(k) = 2\pi\delta(k-k_0) + \frac{ir}{k_0 - k + i\eta/v_{k_0}} + \frac{ir}{k_0 + k + i\eta/v_{k_0}}, \quad k_0 > 0. \quad (6.14)$$

Here, $ir = \alpha/v_{k_0} = (\lambda/v_{k_0})\psi_{k_0}(x{=}0)$.

For the real-space representation, the Fourier transform can be performed by evaluating the k integral by contour integration. The result is

$$\psi_{k_0}(x) = e^{ik_0x} + r\left(\theta(x)e^{ik_0x} + \theta(-x)e^{-ik_0x}\right)\exp(-\eta/v_{k_0}|x|), \quad (6.15)$$

and is sketched, for $\eta = 0$, in Fig. 6.2. Eq. (6.15) at $x = 0$ can be used to calculate the parameter r self-consistently; the result is

$$r = \frac{1}{iv_{k_0}/\lambda - 1}. \quad (6.16)$$

[3] In the presence of an ultraviolet cutoff k_{uv}, one must also impose the condition $x > k_{\mathrm{uv}}^{-1}$.

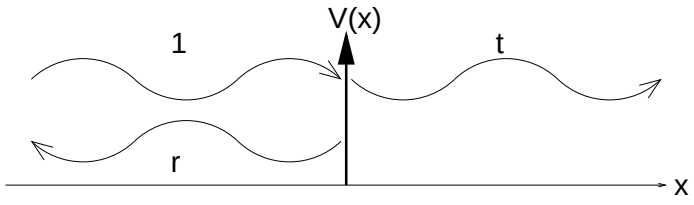

Figure 6.2: Scattering of a single left-moving particle in one dimension on a delta potential.

For $\eta = 0$, this solution coincides with the elementary solution in [Gri94], where the reflection coefficient is given by r, and the transmission coefficient by $t = 1 + r$. In particular, r is compatible with stationary current conservation at $x = 0$, i.e. with the requirement that the current on the left and the right side of the scatterer are identical (cf. Fig. 6.2), which is only met if

$$|1 + r|^2 = 1 - |r|^2 \Leftrightarrow \mathrm{Re}\, r = -|r|^2. \tag{6.17}$$

For finite η, the scattering state Eq. (6.15) is seen to decay exponentially as $e^{-\eta/v_{k_0}|x|}$ to the free state. This is precisely what one expects from Eq. (6.11): Due to the cutoff at time η^{-1}, the scattered wave can travel only as far as v_{k_0}/η.

As a side remark, the transformation matrix $A_{kk'} = \tilde{\psi}_k(k')$ from free to scattering states is unitary in the true continuum limit, i.e. when the limit $\epsilon \to 0$ is fully performed:

$$\lim_{\eta \to 0} \int \frac{dk'}{2\pi} A_{kk'} A^*_{lk'} = 2\pi\delta(k - l). \tag{6.18}$$

For the proof of Eq. (6.18), the delta function has to be represented as

$$\delta(k - k') = \frac{1}{2\pi i} \left(\frac{1}{k - k' - ia^{-1}} - \frac{1}{k - k' + ia^{-1}} \right), \tag{6.19}$$

with $a \to \infty$, and Eq. (6.17) has to be used.

From the scattering wave function, Eq. (6.14) or Eq. (6.15), one obtains the expectation value of the current operator, in x representation given by $\hat{j}(x) = \mathrm{Re}\,(-i\nabla)/m$, such that

$$j(x) = \frac{1}{2m}(\psi^*(x)(-i\nabla)\psi(x) + h.c.). \tag{6.20}$$

This result holds strictly speaking only for the quadratic dispersion relation $\epsilon_k = mk^2/2$; for a more general dispersion relation, $-i\nabla/m$ must be replaced by the operator $\partial\epsilon_k/\partial k$.

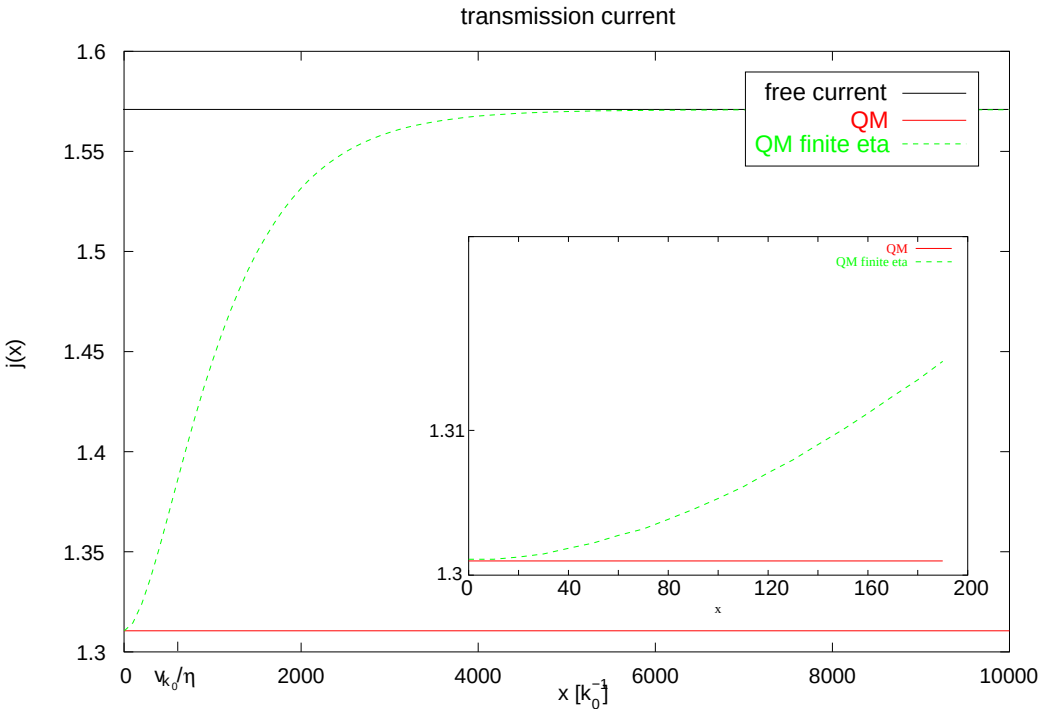

Figure 6.3: Current Eq. (6.20) from the scattering state Eq. (6.15). The curren for nonzero η (dashed line, for $v_{k_0}/\eta = 500/k_0$) agrees with the bulk scattering current $j = v_{k_0}|t|^2$ obtained for $\eta = 0$ (dotted line) only for $x < v_{k_0}/\eta$. for larger values of x, the current crosses over to the free current $j = v_{k_0}$ (solid line).
Inset: Blowup for small x.

In Fig. 6.3, the spatial dependence of the current $j(x)$ from Eq. (6.20) is shown. As one expects, the crossover of the scattering state to the free state on a length scale v_{k_0}/η is also seen in the current. This dependence of $j(x)$ on x does not violate the continuity equation, but reflects the fact that the scattering state is not a truly stationary state for finite $\eta \neq 0$.

As discussed in section 6.5.2 below, it can be advantageous for many-body calculations to work within the momentum-space DMRG method, which uses the k- rather than the x-eigenstates as a basis. In this basis, it may cumbersome (but is certainly possible) to compute the full spatial dependence $j(x)$ as in Eq. (6.20) using the DMRG, because $j(x)$ is highly nonlocal in momentum space. However, full knowledge of the entire function $j(x)$ is unnecessary anyway, since only the value around $x = 0$ is needed. Therefore, it may be a useful strategy to find a current operator that is, within the limits of the uncertainty principle, both reasonably simple in momentum representation and local enough in real space to resolve the spatial dependence of $j(x)$ on a length scale $l_{\text{scatt}} \leq \eta/v_{k_0}$ around the scatterer.

One possible such current operator is

$$\hat{I}_{l_{\text{scatt}}} = \frac{1}{l_{\text{scatt}}} \int dx \hat{j}(x) e^{-|x|/l_{\text{scatt}}}, \tag{6.21}$$

which has the momentum components

$$(I_{l_{\text{scatt}}})_{kk'} = \frac{i}{2l_{\text{scatt}}} v_{k'} \left(\frac{1}{k - k' + i{l_{\text{scatt}}}^{-1}} - \frac{1}{k - k' - i{l_{\text{scatt}}}^{-1}} \right). \tag{6.22}$$

The expectation value of $\hat{I}_{l_{\text{scatt}}}$ with respect to the scattering state wave function $\tilde{\psi}_{k_0}(k)$ given by Eq. (6.14)) is

$$I_{l_{\text{scatt}}} = \frac{v_{k_0}}{l_{\text{scatt}}} \left(l_{\text{scatt}} + \frac{2\text{Re}\, r}{\eta/v_{k_0} + {l_{\text{scatt}}}^{-1}} + \frac{|r|^2}{2\eta/v_{k_0} + {l_{\text{scatt}}}^{-1}} \right). \tag{6.23}$$

In the limit $l_{\text{scatt}} \gg v_{k_0}/\eta$, the free current $I_0 = v_{k_0}$ is obtained as anticipated in Eq. (6.26) above. In the opposite limit $l_{\text{scatt}} \ll v_{k_0}/\eta$, one obtains (using Eq. (6.17))

$$I = v_{k_0}|1 + r|^2 = v_k |t|^2, \tag{6.24}$$

which is the correct result [Gri94].

I finally note in passing that the simplest current operator in k space, namely $\hat{I} = \hat{v}_k$, is not a good choice, i.e. it fails to reproduce the correct scattering current. This is obvious in light of the above considerations, because this choice corresponds to the current spatially averaged over the entire length L,

$$\hat{I} = \hat{v}_k = \frac{1}{L} \int dx \hat{j}(x). \tag{6.25}$$

At finite η, however, the free state evolves into the scattering state only for $|x| < v_{k_0}/\eta$. Because one has to assume $v_{k_0}/\eta \ll L$, see Eq. (6.10), the free current $I_0 = v_{k_0}$ thus completely dominates the average. Indeed, a straightforward calculation using the scattering state in Eq. (6.14) (which I give in a similar form after Eq. (6.23) below) yields the expected result

$$\langle \psi_k^{\mathrm{ret}} | I | \psi_k^{\mathrm{ret}} \rangle = v_{k_0} = I_0. \tag{6.26}$$

This example again demonstrates the necessity for a length scale $l_{\mathrm{scatt}} < v_{k_0}/\eta$, within which the current must be evaluated, and which is missing in Eq. (6.25).

6.4 Generalization to many-body states and DMRG solution

The generalization of the formalism to many-body states is now straightforward, because I deliberately used abstract notations and in fact did not have to assume anywhere that the states are single-particle states. So one may simply use many-body states in all the above equations, and is done.

The main difference is now that E e.g. in Eq. (6.5) now denotes the energy of a many-body state. This leads to one complication, namely that the energy level shifts discussed in section 6.3.1 may have to be taken more seriously than in the single-particle case, because now the level shifts of many occupied single-particle states may accumulate. This difficulty is discussed to some further extent in section 6.3.1.

Now I present the strategy for calculating the scattering states using the DMRG algorithm. As shown in chapter 2, the DMRG allows to represent the many-body states in a truncated Hilbert space. Its basis is chosen, and optimized iteratively, for representing accurately certain target states. For the problem at hand, I choose as the target states the free state $|\phi\rangle$ and the scattering state $|\psi^{\mathrm{ret}}\rangle$. The latter is obtained by solving the Lippmann-Schwinger equation Eq. (6.5) numerically within the truncated Hilbert space. I emphasize that this approach for calculating scattering states does not require the usual assumption of the scattering potential H_s to be small.

In order to solve Eq. (6.5), it is convenient to exploit its striking resemblance to an equation for spectral functions that is widely used in DMRG calculations [KW99; Jec02]:

$$|\psi_A(E + i\eta)\rangle = \frac{1}{E + i\eta - H}|A\rangle \quad \text{with} \quad |A\rangle = \hat{A}|gs\rangle, \tag{6.27}$$

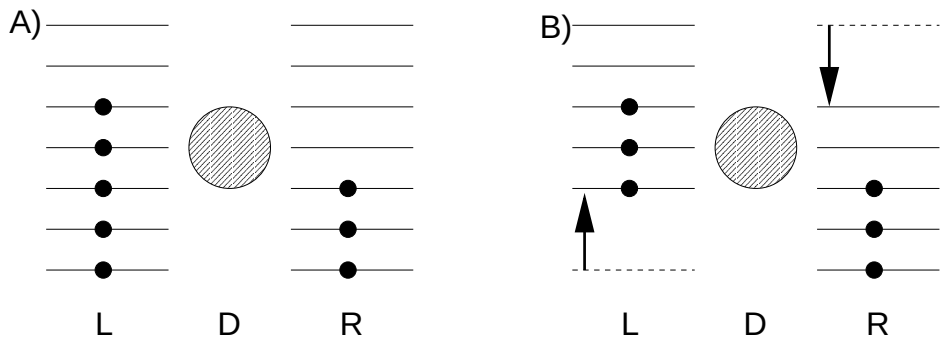

Figure 6.4: Illustration of the nonequilibrium situation considered in section 6.5: The lines represent energy levels of H_0, the full circles represent occupied energy levels of the free state $|\phi\rangle$

where $|gs\rangle$ is the ground state of the system, and $\hat{A}$ is some operator. The only major difference between Eq. (6.5) and Eq. (6.27) is that the state $|A\rangle = \hat{A}|gs\rangle$ of Eq. (6.27) is replaced by the free state $|\phi_k\rangle$ in Eq. (6.5). The strategy I adopt here for constructing $|\phi_k\rangle$ is to calculate it as the ground state of a suitably chosen Hamiltonian, e.g. $H = H_0 + eV(N_L - N_R)$. Details of this procedure depend on the precise model, and are discussed in section 6.5. In [KW99], Eq. (6.27) is solved using the conjugate gradient technique; in [Jec02], it is recast as an extremum condition. I use the former method.

The DMRG algorithm allows to represent the system either in real space or in energy space. Issues specific to each of these variants are presented in the following chapter.

6.5 Applications

6.5.1 Real-space representation

As a first application of the formalism, consider a system consisting of two leads L, R, and a scattering center D, as in Fig. 6.4. In a real-space representation, the leads and the scattering center are given by (finite) chains with nearest-neighbour hopping as illustrated in Fig. 6.5.[4] The model Hamiltonian

[4]The scattering center can in fact be described by an arbitrary model and needs not be given by a one-dimensional chain. The choice of Eq. (6.28) for H_D was made just for simplicity and definiteness, and has the advantage of being quadratic and therefore exactly solvable.

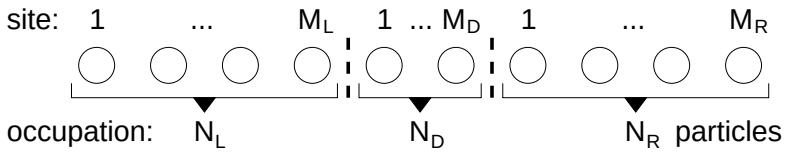

Figure 6.5: Illustration of the real-space scattering formalism of Eq. (6.28): The left and right leads and the scattering center are each represented by a tight-binding chain of length M_L, M_R, M_D, occupied by N_L, N_R, N_D particles.

is then given by $H_0 = H_L + H_R + H_D$, where

$$H_\alpha = \mu_\alpha \sum_{n\in\alpha} c^\dagger_{\alpha n} c_{\alpha n} - t_\alpha \sum_{\langle nn'\rangle\in\alpha} (c^\dagger_{\alpha n} c_{\alpha n'} + h.c.), \quad \alpha = L, R, D. \tag{6.28}$$

Here, $\langle nn'\rangle$ denotes nearest neighbours, the $c^\dagger_{\alpha n}$ create (spinless) Fermions on site αn, and μ_α, t_α are the chemical potential and the tunneling matrix element on lead/scatterer $\alpha = L, R, D$. The length of the chains is denoted by M_L, M_R, and M_D, respectively. In scattering theory, one has to extrapolate to the limit of infinite leads, $M_L, M_R \to \infty$, whereas the size of the scatterer M_D is kept finite. Being quadratic in $c_{\alpha n}$, the model of Eq. (6.28) has an exact solution, which is given in appendix B.

The scattering Hamiltonian entering the Lippmann-Schwinger equation then consists of hopping terms between the regions R, L and D:

$$H_s = -t_s \left(c^\dagger_{LM_L} c_{D1} + c^\dagger_{R1} c_{DM_D} \right) + h.c., \tag{6.29}$$

where the labelling of the sites is as in Fig. 6.5.

As a side remark, it may be advantageous to use in the leads (i.e. in Eq. (6.28) with $\alpha = L, R$) tunneling matrix elements $t_{\alpha n}$ that decay e.g. exponentially with the distance from the scatterer. This corresponds to a non-uniform spatial discretization of the underlying continuum model with high spatial resolution close to the leads and lower resolution away from the leads, and can be used to increase the effective system size that is represented using a given number of lattice sites [Wil75].

The free state $|\phi\rangle$ is constructed as an eigenstate of H_0, namely as the tensor product of the ground states of L, R, and D with N_L, N_R, N_D particles, respectively, as in Fig. 6.5. A source-drain (i.e. L-R-) voltage V can be introduced either by adjusting the relative occupation number $N_L - N_R$ in $|\phi\rangle$ (Fig. 6.4 A), or by tuning the chemical potentials such that $\mu_L - \mu_R = eV$

(Fig. 6.4 B). The scattering state $|\psi\rangle$ is then obtained from the Lippmann-Schwinger equation, Eq. (6.5).

In light of the derivation of the Lippmann-Schwinger equation in Eq. (6.7), the scattering state $|\psi\rangle$ can be seen as the result of slowly (at time $t = -\eta^{-1}$) switching on the tunneling contact H_s during the time evolution of the free initial state $|\phi\rangle$. This bears a striking resemblance to the physical idea behind Keldysh perturbation theory: A nonequilibrium situation is described by slowly switching on a coupling between systems that are not in mutual equilibrium at $t = -\infty$.

Physically, one expects an equilibrating current to flow between the reservoirs that quickly reaches a plateau value I (the current one hopes to be able to reproduce from the Lippmann-Schwinger equation). When, at longer times, the particles are reflected by the lead boundaries and / or the reservoirs are exhausted due to the finite system size, the current will drop to zero or even change sign. These unwanted effects are eliminated by the condition of Eq. (6.10), which assures that the long-time behaviour is damped out for long times by the finite value of η.

I emphasize that this approach is different from the standard applications of scattering theory: Usually, the free states are of the form e^{ikx}, i.e. they carry some momentum k and current $j = v_k$, as in the discussion in the previous sections and in [Dat95]. Here, in contrast, the free state does not carry any current. In fact, the open boundary conditions forbid the existence of a global stationary current and only permit eigenstates of H_0 that are, say, sine-like, without the cosine-like counterparts. Although I expect that one should be able to calculate the plateau value I of the current by tuning the parameters (such as η) appropriately, this nonstandard setting from the view of scattering theory may still pose some unexpected difficulties for the interpretation of the results.

On the other hand, two important advantages of the real-space approach are the experimental relevance of the model defined by Eq. (6.28), and the possibility to give a simple expression for the spatially localized current (on link $n\alpha$, say), namely $I_{n\alpha} = -it_\alpha(c^\dagger_{n\alpha}c_{n+1\alpha} - h.c.)$.

A DMRG code that performs the calculation of the free state $|\phi\rangle$ and the scattering state $|\psi\rangle$ for the model of Eq. (6.28), (6.29) was implemented in collaboration with Peter Schmitteckert. The scattering state $|\psi\rangle$ was obtained as the solution of Eq. (6.5), where the free state $|\phi\rangle$ is sketched in Fig. 6.4 (approaches "A" and "B" of the figure were both implemented). The energy shifts discussed in section 6.3 were not taken into account. As shown in Fig. 6.6, the DMRG could reproduce an exact solution of Eq. (6.5), given in the appendix B.

I emphasize that the results shown e.g. in Fig. 6.6 are a proof-of-principle

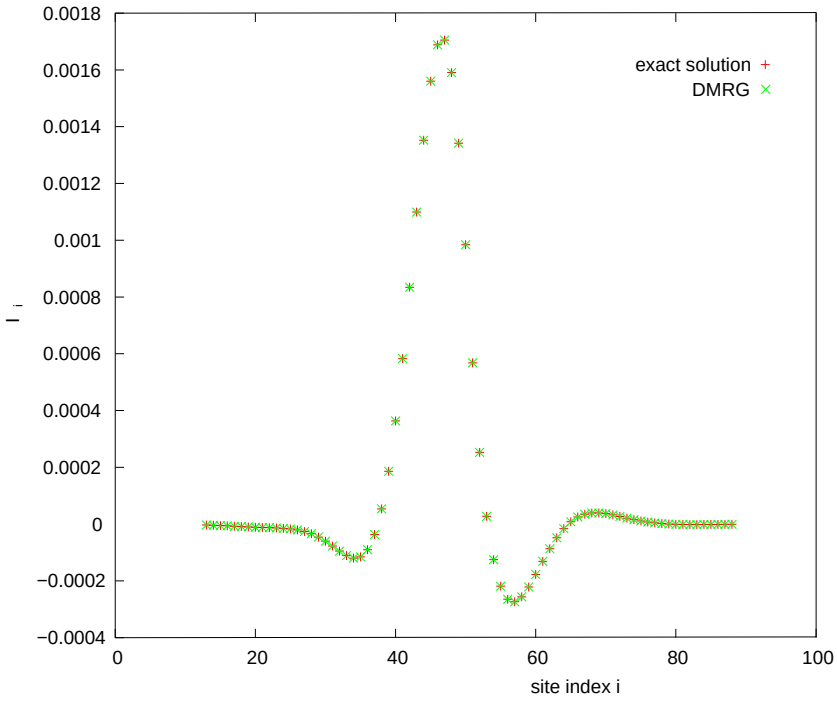

Figure 6.6: The current $\langle\psi|I_i|\psi\rangle/\langle\psi|\psi\rangle$ of the scattering state $|\psi\rangle$ in the real-space formalism is plotted as a function of the site index i. I plot both the result from the exact solution of appendix B (as "+") and from the DMRG solution implemented in cooperation with Peter Schmitteckert (as "x"). They are indistinguishable.
I use the model defined in Eq. (6.28) with the left and right lead each being $M_L = M_R = 50$ sites long (sites $i = 0 \cdots 49$ and $i = 52 \cdots 102$), and with the scattering center consisting of $M_D = 2$ sites ($i = 50, 51$). I show here the results using the approach illustrated in Fig. 6.4A. Here, $\mu_L = \mu_R = \mu_D = 0$, and the left and right lead and the scattering center are occupied by $N_L = 2$, $N_R = 1$, and $N_D = 1$ particle, respectively. The difference between the occupation of the left and the right lead corresponds to the applied source-drain voltage. The parameter η is chosen to have the value $\eta = 0.1$, and $t_\alpha = t_s = 1$.
I emphasize that the purpose of this figure is solely to demonstrate the agreement of DMRG and exact solution. As explained in the text, I cannot provide a physical interpretation of the results.

calculation only, and that I was not able to obtain a physically meaningful interpretation. This may be due to the fact that in the absence of a well-established continuum version of the approach presented here, the numerical parameters η, M_L, M_R were not tuned in the right way, or that the energy shifts discussed in section 6.3 were neglected. In my view, it would be highly instructive to examine the feasibility of this approach by a further study of simple, analytically solvable models. However, I did not pursue this work further.

6.5.2 Momentum representation

In order to avoid the complications of the real-space representation, namely the lack of current-carrying free states due to the open boundary conditions, it is advantageous to use directly the momentum representation instead. This framework allows to construct current-carrying free states in a straightforward way, and to generalize the physical picture behind the Landauer-Büttiker formalism [Hew97; BILP85] to the case of many-body states rather directly.

Here, I have in mind the Landauer-Büttiker formalism at zero temperature, applied to a point contact geometry that would be transparent in the absence of scattering. For this system, the free single-particle states describe electrons that flow through the point contact carrying a momentum k and current v_k. Their free Hamiltonian is given by

$$H_0 = \sum_k \epsilon_k c_k^\dagger c_k. \tag{6.30}$$

One may linearize the dispersion relation, $\epsilon_k = v_{k_{\mathrm{Fermi}}}|k|$, and identify $k > 0$ with right-moving, $k < 0$ with left-moving states as in section 6.3.2.

This model corresponds to the 1-particle model analyzed in section 6.3.2; its global (i.e. spatially averaged) current operator is given by $I = v_{k_{\mathrm{Fermi}}}(N_L - N_R)$, where $N_{R,L} = \sum_{k>,<0} c_k^\dagger c_k$. However, it was shown in section 6.3.2 that will be necessary to evaluate the current localized around the scatterer, e.g. the current

$$I_{l_{\mathrm{scatt}}} = \sum_{kk'} (I_{l_{\mathrm{scatt}}})_{kk'} c_k^\dagger c_{k'} \tag{6.31}$$

with $(I_{l_{\mathrm{scatt}}})_{kk'}$ given by Eq. (6.22).

The free Hamiltonian H_0 of Eq. (6.30) may also contain a part H_D that describes internal degrees of freedom of the scatterer as in the previous section. The scattering Hamiltonian H_s contains terms that scatter electrons into / out of the states k (and possibly of the states into / out of the scattering center D).

In the free state $|\phi\rangle$, the L, R-movers are assumed to be in electrochemical equilibrium with the reservoirs from which they were emitted, i.e. the L-movers with the right, the R-movers with the left reservoir. This assumption is valid if the tunneling at the contacts to the macroscopic leads is reflectionless [Dat95]. If a finite bias voltage is now applied between the leads, the chemical potential of the L- and R-movers is shifted with respect to each other.[5] The free state (at $T = 0$) is then of the form of Fig. 6.4, where in contrast to the real-space approach discussed above, L and R here denote left- and right-*moving* particles, not particles localized on the respective lead.

The Hamiltonian Eq. (6.30) may also describe a different physical picture than the one described above, namely particles localized in a left or right lead as in section 6.5.1. In this picture, the states are not momentum eigenstates, and k must be replaced by a general index for the energy level and the lead L, R. The current is then given by $I \propto \dot{N}_L = i[H_s, N_L]$. I do not pursue this picture any further here and refer instead to section 6.5.1.

The boundary conditions implicit in the discretization of k have a simple interpretation in the case of equidistant k spacing $\Delta k = 2\pi/L$: In this case, only periodic wave functions with period L can be constructed, so it corresponds to periodic boundary conditions.

The main advantage of the approach presented here is that it is very close in spirit to the well-established scattering formalism of Landauer and Büttiker. However, the price to pay from a DMRG perspective is that it is computationally demanding (albeit principally possible) to evaluate a localized current operator like the one in Eq. (6.22). This is because due to the Heisenberg uncertainty principle, such an operator is of long range in k representation, and therefore in general inefficient to implement in the DMRG. Although Eq. (6.22) is a possible candidate for a DMRG implementation, it may be very possible to find a current operator that provides a somewhat better compromise between sufficient spatial resolution and an efficient implementation in momentum DMRG.

I did not implement the algorithm presented in this chapter, which must therefore be regarded as work in progress. However, I hope that the "recipes" given here, as well as the existing implementation of the real-space algorithm, provide the interested reader with sufficient details to be able to pursue this work further.

[5] The periodic boundary conditions implicit in this approach do not contradict the picture of the L- and R-movers being coupled to leads. This is because in the scattering state, boundary effects are damped out on a distance scale $\eta/v_k \ll L$ away from the scatterer, whereas only local quantities on a scale $l_{\text{scatt}} \ll \eta/v_k$ around the scatterer are considered (cf. Eq. (6.12)). The only requirement on the boundary conditions in the present approach is that they allow for a current-carrying free state.

Chapter 7

Conclusions

In this thesis, the DMRG was used to analyze a number of mesoscopic systems that exhibit strong quantum correlations. It was found that the correlations can have, among others, a drastic influence on their transport properties. The specific topics addressed in this thesis were the Josephson effect between superconducting nanograins; the observation of well-defined quasiparticles in small metallic grains; the real-time dynamics of spin chains; and the calculation of many-body scattering states. Due to the diversity of these topics, I now summarize the main results and physical insights obtained in each of them separately.

Josephson effect between superconducting nanograins

I investigated in chapter 3 the fate of the Josephson effect – the dependence of the energy of two weakly coupled superconductors on the difference between their superconducting phase – in the regime that the level spacing d is comparable to the bulk superconducting gap Δ_{BCS}. In this regime, BCS mean-field theory is inapplicable and the notion of a superconducting order parameter with a well-defined phase is no longer valid.

I found that it is nevertheless possible to define a phase *difference*, and that the Josephson effect persists in its essence even as $d \sim \Delta_{\mathrm{BCS}}$ – albeit with the quantitative difference that its typical energy scale, the Josephson energy E_J, is in this regime no longer given by the standard BCS expression. Using the DMRG, I calculated the ground state of the two coupled superconductors and extracted E_J.

In the continuum limit $d \to 0$, I was able to reproduce the standard BCS result for E_J. As d is increased, the Josephson energy turned out to display a reentrant behaviour (decrease followed by increase). A tight-binding approximation for weak Josephson coupling explains the physical mechanism underlying this reentrance in a transparent way: The reason for the decrease with growing level spacing d is that the tunneling of more than

one electron pair is increasingly suppressed. The following increase is due to resonant tunneling of the remaining electron pair.

I examined the limitations of the tight-binding approximation by comparing it to the DMRG solution for two coupled superconductors in the limit of strong inter-grain coupling. Here, I found that, as one would expect, the approximation breaks down for $E_J \geq \Delta_{\mathrm{BCS}}$.

Well-defined quasiparticles in small metallic grains

I analyzed in chapter 4 zero-temperature spectral functions within the universal Hamiltonian / reduced BCS model and found that an important class of such functions is dominated by a single energy eigenstate only. I found that the one state contributing to the spectral function is, moreover, from a very limited subset of all possible excitations, which I characterized as "No-Gaudino states". This implies that only these No-Gaudino states are relevant for many physical properties of the systems under consideration.

I emphasize that this finding is not generalizable to models other than the universal Hamiltonian / reduced BCS model. However, it reveals a highly peculiar property of these models, namely that the excited states can be classified into two subsets, the Gaudino- and the No-Gaudino-states, which possess quite radically different physical properties. As an immediate physical consequence, I found an infinite lifetime of the quasiparticles that occur in many physically relevant spectral functions, which I explain by the fact that just one precise No-Gaudino state is excited.

Real-time dynamics in spin-1/2 chains

In chapter 5, I studied the nonequilibrium properties of spin-1/2 chains by solving the many-body Schrödinger equation for a non-stationary initial state $|\uparrow \ldots \uparrow\downarrow \ldots \downarrow\rangle$, using the adaptive time-dependent DMRG. I investigated the influence of different interaction strength and dimerization on the magnetization transport.

I found that the magnetization possesses a well-defined long-time limit, whose nature does not depend on the dimerization, but only on the strength J_z of the S^zS^z interaction: For $|J_z| < 1$ I found ballistic magnetization transport. For $|J_z| > 1$, on the other hand, I found almost no transport, with a sharp crossover at $|J^z| = 1$. I explained this crossover as a subtle consequence of a quantum phase transition which occurs at the precise value $|J_z| = 1$.

I also performed a detailed error analysis of the adaptive time-dependent DMRG method by comparing its result to an exact solution, available for the XX model. I found that the error at small times is dominated by the error from the Trotter decomposition, whereas for longer times, the DMRG truncation error becomes the most important, with a very sharp crossover at some "runaway" time. This finding should be general and hold for non-

exactly solvable models as well, and should therefore allow to control the accuracy of the results of adaptive time-dependent DMRG in general models.

Many-body scattering states

I presented in chapter 6 a general method for calculating many-body scattering states that does not rely on the assumptions of perturbation theory or near-equilibrium. The strategy is to solve the many-body Lippmann-Schwinger equation using the DMRG. This raised a number of conceptual issues, because the setting is from a scattering theory point of view doubly unfamiliar: Firstly, the algorithm must extrapolate finite-system results, whereas scattering theory is properly defined in an infinite system. Secondly, it is not entirely straightforward to generalize scattering theory from single-particle to many-body states, and has to my knowledge not been done before. The main difficulty here is that level shifts, negligible in single-particle scattering theory, become important.

This chapter must be regarded as work in progress. Due to the complexity of the problem, I have applyied the method to proof-of-principle calculations only. Nevertheless, the conceptual framework and the recipe for a DMRG implementation that I presented should be helpful for a reader interested in pursuing this work further.

Appendix A

DMRG algorithm in energy space

In this section, some technical aspects of the energy-space DMRG procedure for approximating the ground state $|\psi\rangle$ are explained. For a review of the DMRG algorithm itself, I refer to chapter 2, or to the review articles in [WN99; Sch04]. The application to superconducting grains is also discussed in [SD00; DS99]. Therefore, I only highlight the key concepts of the DMRG algorithm, before I discuss details of the DMRG algorithm as applied in energy space. Finally, a few peculiarities are mentioned that are of relevance when the algorithm is applied to the problem of two coupled superconductors.

First, I give an account of the procedure that projects out a reduced number of basis states. The Hilbert space is divided into two blocks A of states below and B of states above the Fermi surface, as depicted in Fig. A.1, each being represented by the respective basis state $|i\rangle_A$ and $|j\rangle_B$. A general many-body state is expressed as $\sum_{ij} \psi_{ij} |i\rangle_A \otimes |j\rangle_B$. The goal is to find a reduced number m of most relevant states $|u_\alpha\rangle_A$ and $|u_\beta\rangle_B$, in the sense that they allow for the best approximation of the state $|\psi\rangle$, such that the norm $\left| |\psi\rangle - \sum_{\alpha\beta} \psi_{\alpha\beta} |u_\alpha\rangle_A \otimes |u_\beta\rangle_B \right|$ is minimized, when variation over both $\psi_{\alpha\beta}$ and the states $|u_\alpha\rangle_A$, $|u_\beta\rangle_B$ are allowed, but only m states per block are to be kept. It turns out that the states with this property are precisely those eigenstates of the reduced density matrix of the respective block (A or B) that correspond to the m largest eigenvalues[WN99]. Of course, the larger m is, the more accurate the algorithm becomes, until convergence is achieved. Typical values for m are $m \sim 100 - 400$.

The prescription for the DMRG algorithm is the following: (i) Start with only a few (2 or 3, say) energy levels, few enough that the exact basis of the many-body system can be kept explicitly. (ii) Add an additional energy

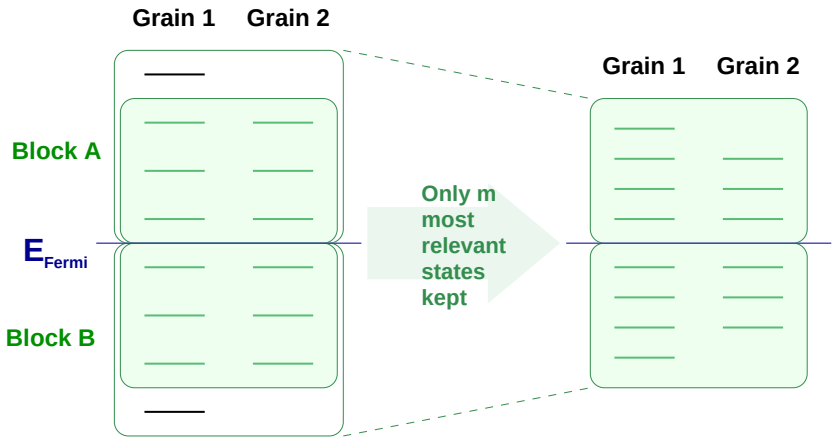

Figure A.1: Sketch of the procedure for projecting out the relevant states in the case of the two-grain DMRG. The shading indicates the part of the Hilbert space where only a limited number of states are kept. First, a new level is added on grain 1 (left part of figure). Then, the m most relevant states are projected out and kept (right part). Then, a new level on grain 2 is added (not shown).

level to block A and B, as depicted in Fig. A.1 for the case of the two-grain DMRG. Construct a basis $|u_\alpha\rangle_A$ for block A, using the basis states from the previous step and the exact basis of the newly added energy level. Do the same with block B. (iii) Calculate the target state $|\psi\rangle$, in this case the ground state of the BCS Hamiltonian, within the present Hilbert space. (iv) Calculate the reduced density matrix of $|\psi\rangle$ for block A and B, say ρ_A and ρ_B, by performing the trace of the full density matrix $|\psi\rangle\langle\psi|$ over the respective other block. Find the m eigenvectors $|u_\alpha\rangle_A$, $|u_\beta\rangle_B$, $\alpha, \beta = 1..m$, corresponding to the m largest eigenvalues of ρ_A and ρ_B. Those are the states to be kept as basis states. (v) Transform all operators to the new basis. If the blocks A and B are related by a symmetry, it may be sufficient to calculate only one set of states $|u_\alpha\rangle$. Continue with step (ii) and iterate, until the final number of energy levels is reached.

In step (iii), the ground state $|\psi\rangle$ is found using the Lanczos procedure, which is very efficient due to the sparse nature of the Hamiltonian, but which requires many multiplications of a state with the Hamiltonian. Since the Hamiltonian is a sparse but extremely large matrix (of order $m^2 \times m^2$), it is essential not to store it as a whole, but to reconstruct it from simple operators acting only on the blocks A and B when the multiplication is performed. For this to be numerically possible, it is necessary that the interactions between

the blocks factorize to a large degree, such that they can be expressed as a sum of only a few terms. In real-space DMRG, this is always the case as long as the interactions are more or less local, but the long-range interactions in energy space do not always factorize. Luckily, the reduced BCS interaction does factorize nicely: $H_{BCS} = -\lambda(b_A^\dagger b_A + b_A^\dagger b_B + A \leftrightarrow B)$, where $b_{A,B} = \sum_{i\in A,B} c_{i\uparrow}c_{i\downarrow}$. A similar factorisation is possible for the inter-grain coupling (3.22) in the two-grain DMRG, but not for (3.13).

It is also essential for numerical efficiency to make use of conserved quantum numbers. In the present case, due to particle number conservation, it is not necessary to keep all the m^2 states $|u_\alpha\rangle_A \otimes |u_\beta\rangle_B$ as a basis. In this algorithm, the number l_α, l_β of particle or hole excitations associated with each basis vector $|u_\alpha\rangle_A, |u_\beta\rangle_B$, respectively, is explicitly kept track of. Then, only the states $|u_\alpha\rangle_A \otimes |u_\beta\rangle_B$ have to be kept for which

$$l_\alpha - l_\beta = l_{\mathrm{tot}}, \tag{A.1}$$

where l_{tot} is the deviation of the total electron pair number from half filling.

In the tight-binding calculation, taking the matrix element $\langle n|b_i|n+1\rangle$ involves approximating two states simultaneously, namely the ground states $|n\rangle$ and $|n+1\rangle$ that correspond to the respective number of electron pairs n and $n+1$. This is simply done by calculating both states in step (iii), and by taking the reduced density matrix of the mixed state with equal weight in step (iv).

In the two-grain DMRG, the calculations are performed in the regime that two states, $|\nu\rangle$ and $|\nu+1\rangle$, as defined in Eq. (3.5), are degenerate. This is done by setting the offset between the energy levels on the left and the right grain to zero, and by including one more electron pair than there would be at half filling, which amounts to setting $l_{\mathrm{tot}} = 1$ in Eq. (A.1). This extra pair can, then, be on the left or the right grain at equal energy cost.

One complication arises away from half filling (i.e. when $l_{\mathrm{tot}} \neq 0$): When, in step (iv), the reduced basis of one block (block A, say) is calculated by tracing over the states in the other block, the part of the trace relevant for the states with quantum number l_α is, due to Eq. (A.1), performed over states which carry a different quantum number l_β. The dimensionality of the two subspaces $\mathcal{H}(l_\alpha)$ and $\mathcal{H}(l_\beta)$ spanned by the part of the reduced density matrix with the respective quantum numbers might be quite different. However, the rank of the reduced density matrix used in step (iv) is limited by the dimension of the space over which the trace is performed, and therefore, the DMRG only works well as long as the dimension of $\mathcal{H}(l_\beta)$ is larger than the number of states with quantum number l_α to be kept. This is not guaranteed away from half filling, i.e. when $l_\alpha \neq l_\beta$.

The problem is solved by mixing a small part (20%) into the reduced density matrix that corresponds to the ground state at half filling ($l_{\mathrm{tot}} = 0$). This state will have a similar information content as the target state away from half filling, as far as the relevant basis vectors are concerned, and adds enough to the rank of the reduced density matrix for the DMRG to work well.

In the two-grain DMRG, the energy levels are added one by one as depicted in Fig. A.1: First levels on grain 1, and only afterwards levels on grain 2 are added. They are added one by one in order to keep the Hilbert space as small as possible. It is also possible and, in fact, would be more symmetric, to add both levels at once, but only at the cost of having the Hilbert space larger by a factor of 4. As it turns out, it is numerically more efficient (yielding higher accuracy at the same computation time) to add the levels one by one.

Appendix B

Exact solution for noninteracting chain in real space

B.1 Single particle scattering state

Let us now consider an exact solution of the quadratic model in Eq. (6.28) for a single particle (nevertheless in second quantization). This introduces some notation and serves as a warmup for the following section, in which a many-body solution is discussed.

We will be using two basis sets: the eigenstates of H^0, $|\phi_k\rangle^0 = c_k^\dagger|0\rangle$ with energies E_k^0 (with some discrete index k that need not be momentum; in practical scattering problems, the index k will contain a distinction between a state on the left or the right lead), or by the eigenstates of the full Hamiltonian $H = H^0 + H_s$, $|n\rangle = d_n^\dagger|0\rangle$ with energies E_n. The transformation between both states is mediated by the mapping $|\phi_k\rangle^0 = \sum_n A_{kn}|n\rangle$.

Now the scattering state $|\psi_k\rangle$ is obtained from the free incoming state $|\phi_k\rangle^0$ via the Lippmann-Schwinger equation Eq. (6.5). In energy representation, $|\psi_k\rangle$ is given by $|\psi_k\rangle = \sum_{n=0}^{N-1} \psi_{kn}|n\rangle$ with

$$\psi_{kn} = \frac{i\eta}{E_k^0 - E_n + i\eta} A_{kn}. \tag{B.1}$$

Once the matrix elements are known, the current is easy to compute. The current on the link between site j and site $j+1$ is given by the expectation value of the current operator $I^j = \frac{1}{i}(tc_j c_{j+1}^\dagger - h.c.)$, [1] which has in the $|n\rangle$

[1] The operator $c_i^\dagger$ creates a particle localized on site $i = 0..N-1$. It will be distinguished from the energy eigenstate creator by the use of letters i and j, instead of k, as an index.

basis the matrix elements $I^j_{nn'} = \langle n|I^j|n'\rangle$, as

$$I(k,j) = \frac{\langle\psi_k|I^j|\psi_k\rangle}{\langle\psi_k|\psi_k\rangle} = \frac{\sum_{nn'} I^j_{nn'}\psi^*_{kn}\psi_{kn'}}{\sum_n |\psi_{kn}|^2}. \tag{B.2}$$

Now the strategy is to diagonalize H and H^0, and thus to obtain the matrix elements $I^j_{nn'}$ and A_{kn}. This allows the evaluation of Eq. (B.1) and Eq. (B.2).

As an important example, let us consider a free particle on a chain. The Hamiltonian is given by Eq. (6.28), with M_L, M_R sites on the leads L, R, and M_s degrees of freedom on the scattering region.

We take the free incoming states $|\phi_k\rangle^0$ to be an eigenstate of the left lead, i.e. eigenstates of the Hamiltonian H^0 with the particle being localized on the sites $i \in L$. There are M_L such states; we denote their energies (with respect to H^0) as E^0_n, $n = 1..M_L$

If all u_i in Eq. (6.28) are the same (e.g. $u_i \equiv 0$), our model is nothing but the tight binding model, and I^j can be evaluated from Eq. (B.1), Eq. (B.2) in closed form. For nonconstant t_i, the states $|\psi_k\rangle$ have to be evaluated numerically (e.g. using the tqli algorithm from Numerical Recipes), which is still relatively simple even for large matrices.

B.2 Many-body scattering state

In this appendix, we construct explicitly a many-body scattering state $|\psi\rangle$ for a toy model, namely a discrete quadratic Hamiltonian, which may be otherwise completely general. We rely on notation introduced in the previous section. From $|\psi\rangle$, we derive a closed formula for the current. This formula is, however, computationally demanding, the number of terms growing exponentially with system size.

Because the full Hamiltonian $H = H^0 + H_s$ is quadratic, it can be written in diagonal form as $H = \sum_n E_n d^\dagger_n d_n$. Here, the $d^\dagger$ operators are single-particle creation operators for eigenstates of H, related to the corresponding free operators $c^\dagger_n$ of H^0 via a unitary transformation

$$c^\dagger_k = \sum_n A_{kn} d^\dagger_n \tag{B.3}$$

with some transformation coefficients A_{kn}.

Our goal is to calculate the expectation value of the current operator I^j on site j, which can (after a transformation into the eigenbasis of H) be written as

$$I^j = \sum_{pq} I^j_{pq} d^\dagger_p d_q = -\sum_{pq} I^j_{pq} d_q d^\dagger_p + I^j_{tr}, \tag{B.4}$$

with $I^j_{tr} = \sum_p I^j_{pp}$.

This expectation value is to be taken using the scattering state from Eq. (6.5), with the free state

$$|\phi\rangle = c^\dagger_{k_1} \cdots c^\dagger_{k_N}|0\rangle = \sum_{l_1 \cdots l_N} A_{k_1 l_1} \cdots A_{k_N l_N} d^\dagger_{l_1} \cdots d^\dagger_{l_N}|0\rangle. \tag{B.5}$$

Eq. (6.5) then gives for the scattering state

$$|\psi\rangle = \sum_{l_1 \cdots l_N} A_{k_1 l_1} \cdots A_{k_N l_N} \frac{i\eta}{E^0 - E(\{l\}) + i\eta} d^\dagger_{l_1} \cdots d^\dagger_{l_N}|0\rangle, \tag{B.6}$$

where $E^0 = \sum_i E^0_{k_i}$, $E(\{l\}) = \sum_i E_{l_i}$.

We now calculate the current expectation value $\langle\psi|I^j|\psi\rangle/\langle\psi|\psi\rangle$. Let us start with the denominator:

$$\begin{aligned}
\langle\psi|\psi\rangle &= \sum_{\substack{l_1 \cdots l_N \\ m_1 \cdots m_N}} A^*_{k_1 l_1} A^*_{k_N l_N} \frac{-i\eta}{E^0 - E(\{l\}) - i\eta} \\
&\quad A_{k_1 m_1} A_{k_N m_N} \frac{i\eta}{E^0 - E(\{m\}) + i\eta} \langle 0|d_{l_N} \cdots d_{l_1} d^\dagger_{m_1} \cdots d^\dagger_{m_N}|0\rangle \qquad \text{(B.7)} \\
&= \sum_{\substack{l_1 \cdots l_N \\ \text{(all different)}}} \sum_P \sigma(P) A^*_{k_1 l_1} A^*_{k_N l_N} A_{k_1 P(l_1)} A_{k_N P(l_N)} \frac{\eta^2}{(E^0 - E(\{l\}))^2 + \eta^2},
\end{aligned}$$

where we used that the fact that $\langle 0|d_{l_N} \cdots d_{l_1} d^\dagger_{m_1} \cdots d^\dagger_{m_N}|0\rangle$ is nonzero only if $(m_1, ..., m_N)$ is a permutation P of $(l_1, ..., l_N)$ and in particular, if all l_i (and thereby all m_i) are mutually different, and is then equal to the sign $\sigma(P)$ of P.

The numerator is only slightly more complicated:

$$\begin{aligned}
\langle\psi|I^j|\psi\rangle &= I^j_{tr}\langle\psi|\psi\rangle - \sum_{\substack{l_0, \cdots l_N \\ m_0 \cdots m_N}} I^j_{l_0 m_0} A^*_{k_1 l_1} A^*_{k_N l_N} \frac{-i\eta}{E^0 - E(\{l_1 \cdots l_N\}) - i\eta} \\
&\quad A_{k_1 m_1} A_{k_N m_N} \frac{i\eta}{E^0 - E(\{m_1 \cdots m_N\}) + i\eta} \langle 0|d_{l_N} \cdots d_{l_0} d^\dagger_{m_0} \cdots d^\dagger_{m_N}|0\rangle \\
&= I^j_{tr}\langle\psi|\psi\rangle - \sum_{\substack{l_0 \cdots l_N \\ \text{(all different)}}} \sum_P \sigma(P) I^j_{l_0 P(l_0)} A^*_{k_1 l_1} A^*_{k_N l_N} A_{k_1 P(l_1)} A_{k_N P(l_N)} \\
&\quad \frac{-i\eta}{E^0 - E(\{l_1 \cdots l_N\}) - i\eta} \frac{i\eta}{E^0 - E(\{P(l1) \cdots P(l_N)\}) + i\eta}. \qquad \text{(B.8)}
\end{aligned}$$

Note that in Eq. (B.8), the first coefficient l_0 does not enter the many-body energy $E(\{l_1 \cdots l_N\})$.

Eq. (B.7) and Eq. (B.8) simplify enormously in the case that Eq. (6.5) mediates a unitary transformation – in fact, Eq. (B.7) then becomes equal to 1. However, as we are not assuming the continuum limit, we have to leave Eq. (B.7) as it is, i.e. as a huge sum that grows exponentially with the number of particles.

So the strategy is the following: Diagonalize the 1-particle versions of H and H_0; thereby obtain the parameters A_{kn} and I^j_{mn}. Then evaluate Eq. (B.8) and Eq. (B.7).

Bibliography

[Aa00] E. Anderson and al. *LAPACK user's guide*. Society for Industrial and Applied Mathematics, 2000.

[AB63] V. Ambegaokar and A. Baratoff. Tunneling between superconductors. *Phys. Rev. Lett.*, 10:486, 1963.

[ABG02] I. Aleiner, P. Brouwer, and L. Glazman. Quantum effects in coulomb blockade. *Phys. Reports*, 358:309, 2002.

[AHDL03] E. Altman, W. Hofstetter, E. Demler, and M. D. Lukin. Phase diagram of two-component bosons on an optical lattice. *New J. Phys.*, 5:113, 2003.

[AL99] D. Averin and K. Likharev. Single electronics: A correlated transfer of single electrons and Cooper pairs in systems of small tunnel junctions. In B. Altshuler, P. Lee, and R. Webb, editors, *Mesoscopic phenomena in solids*. Elsevier, 1999.

[And59] P. W. Anderson. Theory of dirty superconductors. *J. Phys. Chem. Solids*, 11:26, 1959.

[ARRS99] T. Antal, Z. Racz, A. Rakos, and G. Schütz. Transport in the XX chain at zero temperature: Emergence of flat magnetization profiles. *Phys. Rev. E*, 59:4912, 1999.

[BILP85] M. Büttiker, Y. Imry, R. Landauer, and S. Pinhas. Generalized many-channel conductance formula with application to small rings. *Phys. Rev. B*, 31:6207, 1985.

[BRT96] C. Black, D. Ralph, and M. Tinkham. Spectroscopy of the superconducting gap in individual nanometer-scale aluminum particles. *Phys. Rev. Lett.*, 76:688, 1996.

[CAR04] D. S. Jin C. A. Regal, M. Greiner. Observation of resonance condensation of fermionic atom pairs. *cond-mat/0401554; to be published in PRL*, 2004.

[CBS57] L. Cooper, J. Bardeen, and J. Schrieffer. Theory of superconductivity. *Phys. Rev.*, 108:1175, 1957.

[CM02] M. Cazalilla and J. Marston. Time-dependent density-matrix renormalization group: A systematic method for the study of quantum many-body out-of-equilibrium systems. *Phys. Rev. Lett.*, 88:256403, 2002.

[COK98] S. Cronenwett, T. Oosterkamp, and L. Kouwenhoven. A tunable Kondo effect in quantum dots. *Science*, 281:540, 1998.

[Dat95] S. Datta. *Electronic transport in mesoscopic systems.* Cambridge University Press, 1995.

[DDL03] L.-M. Duan, E. Demler, and M.D. Lukin. Controlling spin exchange interactions of ultracold atoms in optical lattices. *Phys. Rev. Lett.*, 91:090402, 2003.

[DeW56] B. DeWitt. Transition from discrete to continuous spectra. *Phys. Rev.*, 103:1565, 1956.

[dG99] P.-G. de Gennes. *Superconductivity of metals and alloys.* Perseus books, 1999.

[DKSV04] A. Daley, C. Kollath, U. Schollwöck, and G. Vidal. Time-dependent density-matrix renormalization group using adaptive effective Hilbert spaces. *J. Stat. Mech.: Theor. Exp.*, page P04005, 2004.

[DMDNS98] J. Dukelsky, M. Martin-Delgado, T. Nishino, and G. Sierra. Equivalence of the variational matrix product method and the density matrix renormalization group applied to spin chains. *Europhys. Lett.*, 43:457, 1998.

[DS99] J. Dukelsky and G. Sierra. Density matrix renormalization group study of ultrasmall superconducting grains. *Phys. Rev. Lett.*, 83:172, 1999.

[ESA04] U. Eckern, P. Schwab, and V. Ambegaokar. Comment on "Magnetic response of disordered metallic rings: Large contributions of far levels". *cond-mat/0402561*, 2004.

[Fer88] R. Ferrell. Josephson effect and Anderson's theorem. *Phys. Rev. B*, 38:4984, 1988.

[GGSM+98] D. Goldhaber-Gordon, H. Shtrikman, D. Mahalu, D. Abusch-Magder, U. Meirav, and M. Kastner. Kondo effect in a single-electron transistor. *Nature*, 391:156, 1998.

[GMG53] M. Gell-Mann and M. Goldberger. The formal theory of scattering. *Phys. Rev.*, 91:398, 1953.

[Gri94] D. Griffiths. *Introduction to quantum mechanics*. Prentice Hall, 1994.

[Gro60] C. Grosjean. *Formal theory of scattering phenomena*. Inst. Interuniversitaire des Sciences Nucleaires, 1960.

[Hew97] A. Hewson. *The Kondo problem to heavy fermions*. Cambridge University Press, 1997.

[HRS04] V. Hunyadi, Z. Racz, and L. Sasvari. Dynamic scaling of fronts in the quantum XX chain. *Phys. Rev. E*, 69:066103, 2004.

[ITJ+89] M. Iansiti, M. Tinkham, A. Johnson, W. Smith, and C. Lobb. Charging effects and quantum properties of small superconducting tunnel junctions. *Phys. Rev. B*, 39:6465, 1989.

[Jec02] E. Jeckelmann. Dynamical density-matrix renormalization-group method. *Phys. Rev. B*, 66:045114, 2002.

[Joa76] C. J. Joachain. *Quantum Collision Theory.* Elsevier, 1976.

[KAA00] I. L. Kurland, I. L. Aleiner, and B. L. Altshuler. Mesoscopic magnetization fluctuations for metallic grains close to the Stoner instability. *Phys. Rev. B*, 62:14886, 2000.

[KL73] K. Knorr and J. Leslie. Metal-insulator-metal tunnel junctions. *Solid State Commun.*, 12:615, 1973.

[KS03] A.B. Kuklov and B.V. Svistunov. Counterflow superfluidity of two-species ultracold atoms in a commensurate optical lattice. *Phys. Rev. Lett.*, 90:100401, 2003.

[KW99] T. Kühner and S. White. Dynamical correlation functions using the density matrix renormalization group. *Phys. Rev. B*, 60:335, 1999.

[Lev03] B. Gross Levi. Ultracold fermionic atoms team up as molecules: Can they form Cooper pairs as well? *Physics Today*, 10 2003.

[LH02] J. Links and K. Hibberd. Integrable coupling in a model for Josephson tunneling between non-identical BCS systems. *cond-mat/0206331*, 2002.

[LSM61] E. Lieb, T. Schultz, and D. Mattis. Two soluble models of an antiferromagnetic chain. *Ann. Phys.*, 16:407, 1961.

[MGG+93] K. Matveev, M. Gisselfält, L. Glazman, M. Jonson, and R. Shekhter. Parity-induced suppression of the Coulomb blockade of Josephson tunneling. *Phys. Rev. Lett.*, 70:2940, 1993.

[MGW+03] O. Mandel, M. Greiner, A. Widera, T. Rom, T. W. Hänsch, and I. Bloch. Coherent transport of neutral atoms in spin-dependent optical lattice potentials. *Phys. Rev. Lett.*, 91:010407, 2003.

[MK04] H.-J. Mikeska and A. Kolezhuk. One-dimensional magnetism. In U. Schollwöck, J. Richter, D. Farnell, and R. Bishop, editors, *Quantum magnetism*, volume 645 of *Lecture Notes in Physics*, page 1. Springer, 2004.

[MMR91] H.J. Mikeska, S. Miyashita, and G.H. Ristow. $S = \frac{1}{2}$ magnetic chains as domain wall systems. *J.Phys.: Cond. Matter*, 3:2985, 1991.

[New82] R. G. Newton. *Scattering Theory of Waves and Particles*. Springer, 1982.

[NO95] T. Nishino and K. Okunishi. Product wave function renormalization group method. *J. Phys. Soc. Jpn.*, 67:3066, 1995.

[NPT99] Y. Nakamura, Y. Pashkin, and J. Tsai. Coherent control of macroscopic quantum states in a aingle-Cooper-pair box. *Nature*, 398:786, 1999.

[OR95] S. Östlund and S. Rommer. Thermodynamic limit of density matrix renormalization. *Phys. Rev. Lett.*, 75:3537, 1995.

[Pes99] I. Peschel, editor. *Density matrix renormalization: a new numerical method in physics*. Springer, 1999.

[PG04] M. Pustilnik and L. Glazman. Kondo effect in quantum dots. *cond-mat/0401517*, 2004.

[Rom65] P. Roman. *Advanced Quantum Theory.* Addison-Wesley, 1965.

[RS64] R. Richardson and N. Sherman. Exact eigenstates of the pairing-force Hamiltonian. *Nucl. Phys.*, 52:221, 1964.

[RSD03] J. Roman, G. Sierra, and J. Dukelsky. Elementary excitations of the BCS model in the canonical ensemble. *Phys. Rev. B*, 67:064510, 2003.

[Saa03] Y. Saad. *Iterative Methods for Sparse Linear Systems, Second Edition.* Society for Industrial and Applied Mathematics, 2003.

[Sch94] G. Schütz. Berry's phase in a one-dimensional quantum many-body system. *Phys. Rev. E*, 49:2461, 1994.

[Sch04] U. Schollwöck. Density-matrix renormalization group. *accepted by Rev. Mod. Phys*, 2004. cond-mat/0409292.

[SD00] G. Sierra and J. Dukelsky. Crossover from bulk to few-electron limit in ultrasmall metallic grains. *Phys. Rev. B*, 61:12302, 2000.

[SILO03] M. Schechter, Y. Imry, Y. Levinson, and Y. Oreg. Pairing and persistent currents - the role of the far levels. In H. Takayanagi and J. Nitta, editors, *Towards the Controllable Quantum States*, page 314. World Scientific, Singapore, 2003. cond-mat/0211315.

[SILvD01] M. Schechter, Y. Imry, Y. Levinson, and J. von Delft. Thermodynamic properties of a small superconducting grain. *Phys. Rev. B*, 63:214518, 2001.

[SOIL03] M. Schechter, Y. Oreg, Y. Imry, and Y. Levinson. Magnetic response of disordered metallic rings: Large contribution of far levels. *Phys. Rev. Lett.*, 90:026805, 2003.

[Suz76] M. Suzuki. Relationship between d-dimensional quantal spin systems and (d+1)-dimensional Ising systems. *Prog. Theor. Phys.*, 56:1454, 1976.

[SvDIL03] M. Schechter, J. von Delft, Y. Imry, and Y. Levinson. Two pairing parameters in superconducting grains. *Phys. Rev. B*, 67:064506, 2003.

[Tay72] J. R. Taylor. *Scattering Theory.* Wiley, 1972.

[Tin96] M. Tinkham. *Introduction to Superconductivity*. McGraw-Hill, 1996.

[VC04] F. Verstraete and J. Cirac. Renormalization algorithms for quantum-many body systems in two and higher dimensions. *cond-mat/0407066*, 2004.

[vDR01] J. von Delft and D.C. Ralph. Spectroscopy of discrete energy levels in ultrasmall metallic grains. *Physics Reports*, 345:61, 2001.

[Ver] F. Verstraete. private communication.

[VGRC04] F. Verstraete, J.J. Garcia-Ripoll, and J.I. Cirac. Matrix product density operators: simulation of finite-T and dissipative systems. *cond-mat/0406426*, 2004.

[Vid04] G. Vidal. Efficient simulation of one-dimensional quantum many-body systems. *Phys. Rev. Lett.*, 93:040502, 2004.

[Wei95] S. Weinberg. *The Quantum Theory of Fields*. Cambridge University Press, 1995.

[WF] S. White and A. Feiguin. in preparation.

[WF04] S. White and A. Feiguin. Real time evolution using the density matrix renormalization group. *Phys. Rev. Lett.*, 93:076401, 2004.

[Whi96] S. White. Spin gaps in a frustrated Heisenberg model for CaV_4O_9. *Phys. Rev. Lett.*, 77:3633, 1996.

[Wil75] K. Wilson. The renormalization group: Critical phenomena and the Kondo problem. *Rev. Mod. Phys.*, 47:773, 1975.

[WN99] S.R. White and R.M. Noack. Density matrix renormalization group. In I. Peschel, X. Wang, M. Kaulke, and K. Hallberg, editors, *Density matrix renormalization: a new numerical method in physics*. Springer, 1999.

[WPE02] Saul A. Teukolsky W. Press (Editor). *Numerical Recipes in C++: The Art of Scientific Computing*. Cambridge University Press, 2002.

List of publications

Parts of this thesis have been published previously in somewhat modified form:

- Parts of chapter 3 in
  Dominique Gobert, Ulrich Schollwöck, and Jan von Delft,
  Josephson effect between superconducting nanograins with discrete energy levels,
  European Physical Journal B **38**, 501 (2004).

- Parts of chapter 4 in
  Dominique Gobert, Moshe Schechter, Ulrich Schollwock, and Jan von Delft,
  Well-defined quasiparticles in interacting metallic grains,
  cond-mat/0404614, accepted by Phys. Rev. Lett.

- Parts of chapter 5 in
  Dominique Gobert, Corinna Kollath, Ulrich Schollwöck, and Gunter Schütz,
  Real-time dynamics in spin-1/2 chains with adaptive time-dependent DMRG,
  cond-mat/0409692, submitted to Phys. Rev. E.

The following publication is not included in this thesis:
Dominique Gobert, Jan von Delft, and Vinay Ambegaokar,
Comment on "Quantum measurement and decoherence",
Phys. Rev. A **70**, 026101 (2004).

Acknowledgments:

It is a pleasure to thank Ulrich Schollwöck and Jan von Delft for advising me on the topics of this thesis. I was very lucky to have advisors that supported me so constantly and actively. Discussing with them was both fun and instructive. I also appreciate having been introduced to their collaborators, and having been sent around to various summer schools and projects around the world. I also thank Herbert Schoeller for refereeing this thesis.

I wish to tank Moshe Schechter for his patience in discussing physics with me, and for the warm reception he gave me in Israel. A special thanks goes to Dorit, Itai and everybody else at Kibbuz Naan for their hospitality. I also wish to thank the people at Weizmann Institute and Avi Schiller for very instructive discussions.

It has been a great pleasure working with Vinay Ambegaokar. I was deeply impressed by his profound physical insights, and enjoyed very much working on our little joint project, which taught me a lot about the sociology of science. Of the other people at Cornell, I thank in particular Piet Brouwer and his group.

I thank Peter Schmitteckert and his family for their kind hospitality.

It was fun collaborating with Gunther Schütz and meeting his group at Schloss Wolfsburg.

A big thanks goes to Ralf Simmler, Robert Dahlke and Jens Schmalzing for keeping the computers running, and for being extremely helpful with all kinds of computer stuff.

Thanks to Andreas, Thomas K. and B., Frank, Severin, Ian, Corinna and Robert for proofreading parts of this manuscript and for pointing out many inconsistencies to me. Of course, I am the sole responsible for the remaining errors.

I was lucky to have Silvia, Corinna and Robert as my office mates in Munich, and Thomas and Andreas in Aachen. I do not know how much of my Ph.D. thesis I will remember in 20 years from now, but I will certainly not forget the great fun we had, also outside our office. I also enjoyed having everybody else from Ulrich Schollwöck's and Jan von Delft's group – Frank, Henryk, Udo, Michael, Markus, Rolf, Laszlo and Ian –, and from Herbert Schöller's group – Maarten, Christian, Severin, Frank, Thomas, Olaf, Katja and Stefan – around in München and in Aachen. Finally, a special thanks goes to Anna, the members of the Physiker-Stammtisch, and to all my other friends.

Curriculum Vitae

Persönliche Daten

Name:	Dominique Gobert
Geburtsdatum:	10. September 1974
Geburtsort:	München
Familienstand:	ledig

Schulische und universitäre Ausbildung

1981 – 1985	Grundschule Canisiusschule München
1985 – 1994	Ludwigsgymnasium München
Juni 1994	Abitur
	Studium Diplom Physik
1998 – 2000	Universität Regensburg
April 1996	Vordiplom
1996/97	Université Montpellier II (Frankreich)
1997/98	University of Illinois (USA)
1994 – 1998	Ludwig-Maximilians-Universität München
Dezember 2000	Diplom Diplomarbeit am Lehrstuhl Prof. Dr. Julius Wess *Einschränkungen an Dilaton-Kopplungen*
	Promotion
Juli 2001	Beginn der Promotion bei Prof. Dr. Ulrich Schollwöck und Prof. Dr. Jan von Delft Ludwig-Maximilians-Universität München, Rheinisch-Westfälische Technische Hochschule Aachen *Applications of the density-matrix renormalization group to mesoscopic phenomena*

Stipendium

1994 – 2000	Bayerische Begabtenförderung

Erklärung

Hiermit erkläre ich, daß die vorliegende Arbeit von mir selbst angefertigt wurde, daß ich dies selbständig getan und dabei andere als die angegebenen Quellen nicht verwendet habe. Die den benutzten Werken wörtlich oder inhaltlich entnommenen Stellen sind als solche kenntlich gemacht.

München, den 28. September 2004